# CHIRALITY AND NANOPARTICLES ENFORCED STABILIZATION OF TOPOLOGICAL DEFECTS IN LIQUID CRYSTALS

Apparao Gudimalla

**Doctoral Dissertation**
**Jožef Stefan International Postgraduate School**
**Ljubljana, Slovenia**

**Supervisor:** Prof. Dr. Samo Kralj, IPS and University of Maribor, Maribor, Slovenia
**Co-Supervisor:** Prof. Dr. Sabu Thomas, Mahatma Gandhi University, Kerala, India
**Co-Supervisor:** Asst. Prof. Dr. Brigita Rožič, Jožef Stefan Institute, Ljubljana, Slovenia

**Evaluation Board:**
Prof. Dr. Uroš Cvelbar, Chair, IPS and Jožef Stefan Institute, Ljubljana, Slovenia
Dr. Aleksandra Drozd-Rzoska, Member, Polish Academy of Sciences, Warsaw, Poland
Prof. Dr. Robert Repnik, Member, University of Maribor, Maribor, Slovenia

MEDNARODNA PODIPLOMSKA ŠOLA JOŽEFA STEFANA
JOŽEF STEFAN INTERNATIONAL POSTGRADUATE SCHOOL


Apparao Gudimalla

# CHIRALITY AND NANOPARTICLES ENFORCED STABILIZATION OF TOPOLOGICAL DEFECTS IN LIQUID CRYSTALS

**Doctoral Dissertation**

# STABILIZACIJA TOPOLOŠKIH DEFEKTOV V TEKOČIH KRISTALIH S POMOČJO KIRALNOSTI IN NANODELCEV

**Doktorska disertacija**

**Supervisor:** Prof. Dr. Samo Kralj

**Co-Supervisor:** Prof. Dr. Sabu Thomas
**Co-Supervisor:** Asst. Prof. Dr. Brigita Rožič

Ljubljana, Slovenia, November 2021

*To ...*

# Acknowledgments

I am short of words to express my deep sense of gratitude to all the people I have come across. All of them have contributed to my success directly or indirectly. But, here I am trying to figure out some persons who have influenced me a lot and have left their footsteps for me to follow.

It is a great pleasure to express my deep sense of gratitude to my supervisors Prof. Dr. Samo Kralj, Prof. Dr. Sabu Thomas, and Asst. Prof. Dr. Brigita Rožič for their excellent guidance and deep foresight for completing my research work. I would like to thank Prof. Dr. Samo Kralj for guiding me through the years of researching, for all his advices, support, and patience at the time of writing and preparing this thesis.

I express my profuse gratitude to Prof. Dr. Zdravko Kutnjak, Dr. Marta Lavrič, and Dr. George Cordoyiannis for guiding, teaching, and supporting me throughout the experiments and also providing materials and characterization labs, suggesting a problem and their constant encouragement, inspiring guidance throughout the tenure of my work without which this work would not have come to light. Their help gave a better direction to my experiments, which is a part of my thesis. I wish to thank Prof. Dr. Milan Ambrožič for teaching me theory and writing the research article. Special thanks to Prof. Dr. Aleksander Zidanšek for helping and supporting me, writing research articles, and his valuable suggestions to complete my course successfully.

It gives me great pleasure the support and help of Prof. Dr. Uroš Cvelbar and his research group for allowing me to work in their labs. Thanks to my colleague Mr. Saša Harkai for teaching and supporting me. Also, thanks to Dr. VSR Jampani, Dr. Miha Škarabot, Dr. Nikola Novak and Mr. Dejvid Črešnar and all other co-workers from the institute.

Special thanks to my extended family Mr. Rajesh Kannan and his family, Mr. A S Kiran, Dr. Neelakandan M S, Mr. Raghunath V, Dr. Dona P, Ms. Katarina R M, and Mr. Stefan M for their support in all possible ways and successful completion of my thesis.

I express my sincere thanks to all IJS and MPŠ students and staff, and all other friends for their help, whose company provided me with joyful moments in my research life. This thesis would not have been possible without the scholarship by ADFUTURA (Public Scholarship, Development, Disability, and Maintenance Fund of Republic of Slovenia).

Last but not least, I extend my sincere thanks to my parents, my lovely sisters, and my friends for their care and moral support for the completion of my work.

# Abstract

Of our main interest in this work is the stabilization of assemblies of topological defects (TDs) in liquid crystals (LCs). Due to the topological origin of TDs, the physics of defects is of interest for all branches of physics, including condensed matter systems, particle physics, and cosmology. LCs represent an ideal testbed for the physics of TDs. In the thesis, we mainly focus on the impact of chirality and different nanoparticles (NPs) on the stability and positioning of assemblies of TDs. The thesis research activities include experimental measurements, theoretical modeling, and numerical simulations. In the experimental part, we focus on the preparation of mixtures of magnetic NPs and CE8 LC. Further, using polarized optical microscopy (POM) and high-resolution calorimetry, the stabilization of Blue Phase (BP) and Twist Grain Boundary A ($TGB_A$) phases have been studied. In theoretical modeling, we use Landau-de Gennes-Ginzburg's mesoscopic approach in terms of nematic tensor and smectic complex order parameters.

We first consider the impact of chirality and saddle-splay elasticity on the stabilization of multiple-twisted structures in nematic LCs. For this purpose, we used the Frank-Oseen approach, where the nematic order is described solely by the nematic director field. Cylindrical geometry was used in which we were able to determine critical conditions for the onset of multiple-twisted structures for different boundary constraints. Such structure leads inevitably contain lattices of TDs in three dimensions due to topological reasons. Next, we were interested in the mechanical forces on NPs immersed in nematic LC structures.

Finally, we considered LC structures exhibiting qualitatively different lattices of line defects. These are realized in blue phases and smectic A (SmA) twist grain boundary phases. BPs and $TGB_A$ exhibit disclinations (line TDs in nematic orientational order) and dislocations (line TDs in translational order), respectively. The core structure of disclinations is essentially biaxial and of screw dislocations essentially nematic uniaxial. The fundamental mechanism stabilizing these structures is in fact curvature. However, the efficiency of stabilizing specific TDs depends on NPs' geometrical details.

The above theoretical results were experimentally verified in mixtures of quasi-spherical magnetic NPs and CE8 liquid crystal. POM and high-resolution calorimetric results demonstrated stabilization of $TGB_A$ long-range order as well as modest stabilization of BPI phase, while suppression of the disordered BPIII phase. These results are similar to those found in mixtures of the same LC with gold nanorods, demonstrating that magnetic nanoparticles filling the topological defect cores form probably elongated clusters, which mimic highly anisotropic nanorods.

# Povzetek

Naš glavni interes je stabilizacija sklopov topoloških defektov (TD) v tekočih kristalih (TK). Zaradi topološkega ozadja TD, je fizika defektov zanimiva za vsa področja fizike, vključno s sistemi kondenzirane materije, fiziko delcev in kozmologijo. TK predstavljajo idealno preizkusno mesto za fiziko TD. V doktorskem delu se osredotočamo predvsem na vpliv kiralnosti in različnih nanodelcev (ND) na stabilnost in pozicioniranje sklopov TD. Disertacija vključuje eksperimentalne meritve, teoretično modeliranje in numerične simulacije. V eksperimentalnem delu smo se osredotočili na pripravo mešanic magnetnih ND in CE8. Nadalje so z uporabo polarizirane optične mikroskopije (POM) in kalorimetrije visoke ločljivostji proučevane stabilizacije TK faz, $TGB_A$ in modrih faz (BP). Pri teoretičnem modeliranju smo uporabili Landau-de Gennes-Ginzburgov mezoskopski pristop v smislu nematskega tenzorja in smektičnih kompleksnih ureditvenih parametrov.

Najprej smo upoštevali vpliv kiralnosti in elastičnost sedla na stabilizacijo večkrat zvitih struktur v nematskih TK. V ta namen smo uporabili Frank-Oseenov pristop, kjer je nematski red opisan izključno s poljem nematskega direktorja. Uporabljena je bila cilindrična geometrija, v kateri smo lahko določili kritične pogoje za nastanek večkrat zvitih struktur (MTS) za različne robne omejitve. Takšen strukturni svinec zaradi topoloških razlogov neizogibno vsebuje mreže TD v treh dimenzijah. Uporabili smo cilindrično geometrijo in različne robne pogoje, da smo približno posnemali vpliv domenskih mej, ki ločujejo regije z različno usmerjenimi več-zvitimi konfiguracijami. Nadalje so nas zanimale mehanske sile na ND, ki so dani v nematske TK strukture.

Nazadnje smo upoštevali TK strukture, ki kažejo kvalitativno različne mreže linijskih defektov. Ti se realizirajo v modrih fazah (BPs) in smektični A (SmA) fazi, twist grain boundary ($TGB_A$) fazah. BP in $TGB_A$ kažejo disklinacije (linija TD v nematskem orientacijskem redu) in dislokacije (linije TD v translacijskem redu). Struktura jedra disklinacij je nematska dvoosna in vijačnih dislokacij nematska enoosna. Eksperimentalno smo pokazali, da lahko iste vrste ND učinkovito stabilizirajo obe mreži TD. Temeljni mehanizem, ki stabilizira te strukture, je pravzaprav ukrivljenost. Učinkovitost stabilizacije specifičnih TD je odvisna od geometrijskih podrobnosti ND.

Zgornji teoretični rezultati so bili eksperimentalno preverjeni v mešanicah kvazisferičnih magnetnih ND in tekočega kristala CE8. POM in kalorimetrični rezultati z visoko ločljivostjo so pokazali stabilizacijo dolgega reda $TGB_A$, pa tudi skromno stabilizacijo faze BPI, hkrati pa zaviranje neurejene faze BPIII. Ti rezultati so podobni tistim, ki jih najdemo v mešanicah istega TK z zlatimi nanopalčkami slednje dokazuje, da magnetni nanodelci, ki zapolnijo jedra topološkega defekta, verjetno tvorijo podolgovate grozde, ki posnemajo nanopalčke z anizotropnim razmerjem stranic.

# Contents

# List of Figures

# List of Tables

# Abbreviations

| | | |
|---|---|---|
| TDs | ... | Topological defects |
| LCs | ... | Liquid crystals |
| CE8 | ... | S-(+)-[4-(2'-methylbutyl) phenyl 4'-n-octylbiphenyl-4-carboxylate] |
| NPs | ... | Nanoparticles |
| MTS | ... | Multiple-twisted structures |
| F | ... | Free energy |
| K | ... | Kelvin |
| T | ... | Temperature |
| I | ... | Isotropic |
| N | ... | Nematic |
| $N^*$ | ... | Chiral nematic |
| $\mathtt{N}^*_{\mathtt{L}}$ | ... | Chiral line nematic |
| BP | ... | Blue phase |
| TGB | ... | Twist grain boundary |
| SmA | ... | Smectic A |
| DCR | ... | Defect Core Replacement |
| ADCT | ... | Adaptive Defect Core Targeting |
| TEM | ... | Transmission electron microscopy |
| DLS | ... | Dynamic light scattering |
| RT | ... | Radially twisted |
| RZT | ... | Radially-z-twisted |
| NLC | ... | Nematic liquid crystal |
| POM | ... | polarized optical microscopy |
| RPM | ... | Rotation per minute |
| nm | ... | Nano meter |
| µm | ... | Micro meter |
| µL | ... | Micro liter |
| OA | ... | Olic acid |
| $L$ | ... | Latent heat |
| H | ... | Enthalpy |
| $G$ | ... | Gaussian curvature |
| $R$ | ... | Radius |
| ACC | ... | ac calorimetry |

# Symbols

| | | |
|---|---|---|
| $\vec{n}$ | ... | nematic director |
| $s$ | ... | uniaxial order parameter |
| $\chi$ | ... | NPs concentration |
| $\eta$ | ... | Translational order parameter |
| $\Psi$ | ... | smectic order parameter |
| $\phi$ | ... | phase factor |
| $\rho$ | ... | spatial variation |
| $T_*$ | ... | change in temperature |
| $\xi$ | ... | correlation length |
| $W$ | ... | surface potential constant |
| $\alpha$ | ... | critical exponent |
| $C_\perp$ | ... | elastic constant |
| $C_\parallel$ | ... | compressibility constant |
| $q$ | ... | wave vector |
| $\vec{e}$ | ... | unit vector |
| $R$ | ... | radius |
| $d_0$ | ... | layer thickness |
| $I_{(d)}$ | ... | Identity matrix |
| $\vec{v}$ | ... | Interface vector |
| $C_p$ | ... | heat capacity |
| $Q$ | ... | tensor order parameter |
| $Tr$ | ... | trace operation |

# Chapter 1

# Introduction

Soft nanocomposites consisting of liquid-crystalline (LC) [1] matrices hosting nanoparticles (NPs) comprise a research topic of high interest [2], [3]. In such systems, both the individual and combined properties of the constituents are exploited. These nanocomposites [4] often display either greatly enhanced or qualitatively new features with respect to pure LC matrices.

The key reasons for the intense interest in studying the properties of soft nanocomposites are as follows. The diverse LC configurations [5] display a plethora of physical phenomena that could be exploited in various applications [6]. Furthermore, LC matrices exhibit a unique combination of liquid character, optical anisotropy, and softness. The liquid LC character enables a relatively simple preparation of LC-NP mixtures and phase separation phenomena can be avoided with careful choice and/or surface treatment of the latter. Combining diverse of LC configurations and with different NP dopants (with diversity in their chemical structure, NP size and shape variations, surface treatments, etc.) increases the complexity of potential emerging phenomena [7]. Optical anisotropy of LCs allows one to experimentally probe the main structural and phase transition properties using simple (e.g., polarising optical microscopy) experimental setups. Finally, LC softness provides the capability of relatively strong responses to even weak perturbations [8].

The origin of softness is the continuous symmetry breaking [5], [ 8] via which most LC phases, the so-called mesophases, are reached. The transition between different mesophases could be described by an order parameter field, consisting of two qualitatively different contributions: the *amplitude* field and the *symmetry-breaking* (also referred to as the *phase*) field. The first component determines the strength of a newly established order, exhibiting a single equilibrium value for given conditions. On the contrary, the second component describes a symmetry-breaking choice among an infinite degenerate set of possible options. Firstly, this degeneracy is reflected in easily excitable Goldstone fluctuations that introduce softness to LC phases [8]. The symmetry-breaking field endows LCs with a sensitive structural "vision" of conditions in different parts of the LC body. They could even give rise to long-range forces between immersed objects, such as NPs. Secondly, owing to degeneracy, the symmetry-breaking fields could be in general frustrated, giving rise to topological defects (TDs) [9], [10].

In most cases, TDs appear in localized regions where the relevant symmetry-breaking field is not uniquely defined. This "singularity" typically gives rise to the local melting of the amplitude field. The local region, where the amplitude is substantially suppressed, defines the "core" of a defect. The correlation length of the amplitude field determines the characteristic linear size of a defect's core.

Note the symmetry-breaking phase transitions and consequently TDs are ubiquitous in nature [11]. The resulting phenomena are intertwined with universal behaviors. Namely, the topological origin of TDs, which is "blind" for microscopic details, makes this area of

research strongly interdisciplinary [11], of interest for particle physics to condensed matter, and even cosmology. To emphasize the potential importance of the physics of TDs we remind that "fields" could represent basic entities of nature [12]. In this case, topologically protected TDs might represent "fundamental particles", as first suggested by Skyrmy [13].

Furthermore, it is well known that appropriately surface-decorated nanoparticles (NPs) could be efficiently trapped within cores of defects [14]. The reason behind this is mainly the Defect Core Replacement (DCR) mechanism [14]. Namely, if NPs are trapped within the cores of defects, their non-singular volume reduces the free energy cost of the defect core. Consequently, one can manipulate the stability of defects via NPs, or vice versa, TDs could be exploited to control spatial assembling of NPs.

In general, the presence of TDs is energetically costly, and therefore, structures dominated by TDs are relatively rarely realized in bulk equilibrium. In bulk LCs, they could be stabilized by the inherent chirality of LC molecules [5]. For strong enough chiralities LC phases exhibiting lattices of line TDs in orientational or translational order could exist, referred to as disclinations and dislocations, respectively [5]. These are realized in Blue Phases (BPs) [15], [16] and smectic Twist-Grain Boundary phases (TGBs) [17], [18].

In many cases, chirality is very efficient in stabilizing TDs. Chirality is pervasive in nature and refers to cases where an object and its mirror image are different [19]–[22]. It signals the absence of the inversion symmetry, giving rise to right-handed and left-handed appearance. Chirality is present at all branches of physics and often impacts or even dominates numerous important natural phenomena. Chiral symmetries play an important role in weak interactions of the Standard Model of physics [23]. Functionalities of several essential components of biological cells rely on chirality [20]. For instance, we metabolize only right-handed glucose. Handedness enables various self-assembling mechanisms [24]–[28], and the sensitivity of molecular details on handedness is clearly manifested in DNA configurations [29]. Chirality could propel micro-swimming [30], [31] motions. Furthermore, it could be exploited in various technological and medical applications. In particular, in optically transparent media chirality could strongly affect (e.g., rotate) the polarisation of light. Chiral materials, in general, respond differently to right- and left-handed polarised electromagnetic waves. Using basic chiral constituents, one could design systems that sensitively control the response of different display devices and sensors [32]–[36]. One could engineer new materials with extraordinary properties (e.g., metamaterials exhibiting negative refractive index [37], [38]) or self-assembling structures for different photonic applications [39]. Therefore, a deep understanding of chirality and related emergent behaviors are of interest to all branches of physics.

However, several issues related to chirality remain unresolved [40]–[44] even at a fundamental level. For instance, the molecular origins of chirality and the relative role of chiral symmetry breaking remain an open problem [45]. In particular, mechanisms involved in chirality transfer from microscopic to macroscopic levels [46]–[48] are not sufficiently understood. A convenient system to gain a deeper understanding of the latter feature are chiral nematic liquid crystals (LCs), the simplest representatives of anisotropic soft materials [49], [50]. Namely, these systems are easily experimentally available, relatively weak external stimuli could trigger structural changes, and a few parameters determine chirality. However, macroscopic chirality-driven behavior could be extremely complex if appropriate confining geometries are used [51]. Finally, chirality often enables appropriate conditions for the spontaneous formation of complex structures of TDs.

The plan of the thesis is as follows. In Chapter 2, we presented the theoretical basics used in our research. LC structures are introduced, where particular attention is paid, to configurations hosting line defects in orientational and translational order. Phenomenological mesoscopic model, in terms of nematic tensor order parameter and

smectic A complex order parameter is presented. This section concludes with curvature and, nanoparticles-driven topological defects stabilising mechanisms. In Chapter 3, the experimental background is described. Liquid crystal compounds and magnetic NPs used in our experiments are presented. We describe experimental techniques used to monitor LC configurations and determine. In Chapter 4, the results of our research are presented and discussed.

We first consider on chirality-driven frustrations that enable TDs in LCs. In this case, we limit to nematic structures in cylindrical confinements. We study chirality driven multi-twisted structures, where we use a Laudau-type analytical approach supported by numerical simulations, conditions are determined under such structures could be stabilized. Three-dimensional packing of such structures, which we stabilize in cylindrical confinements, would lead to line topological defects in orientational order. Next, we investigated theoretically how topological defects could be exploited to assemble appropriate surface decorated NPs. For this purpose, we consider the nematic phase, where we allow nematic biaxial states. As a testbed, we use cylindrical confinement where boundary conditions enforce the surface TDs. We show that nanoparticles would be attracted to the core of the defect only if conditions at its surface are compatible with the local nematic structure. Afterwards, we focus on stabilising with an appropriate surface decorated NPs on LC phases hosting line defects in orientational and translational order. We first consider only the impact of NPs geometry on the stabilization. We show that spherical and anisotropic NPs stabilise different defect lattices. Next, we study spherical magnetic NPs. We have done extensive experimental investigations for this case because this kind of investigation has not yet been performed. In last Chapter 5 summarizes the main novelties of my work.

# Chapter 2

# Theoretical Background

This chapter presents the basics of liquid crystals and their structures and the theoretical framework on which my research work was based.

## 2.1 Liquid Crystal Structures

### 2.1.1 Defectless liquid crystal phases

The mechanical and symmetry properties of LC phases are intermediate between those of a conventional isotropic liquid and those of a solid crystal. The most common LC types are shown in Figure 2.1 and are referred to as *thermotropic, lyotropic,* and *polymeric* LCs [5], [52]–[56].

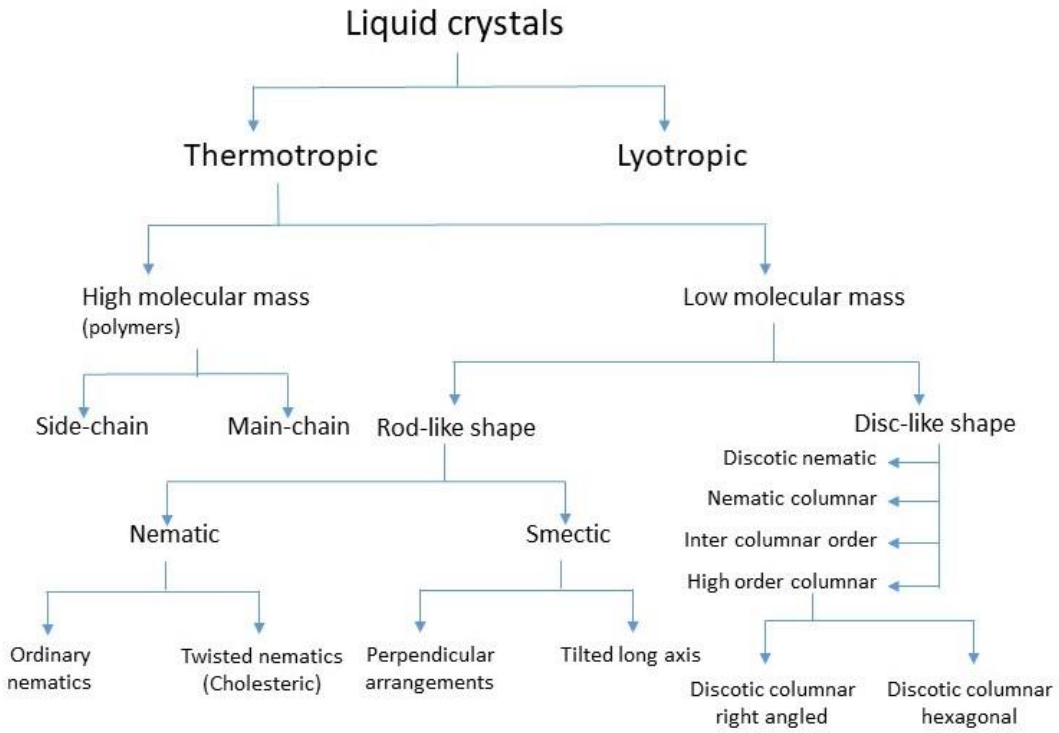


Figure 2.1: A general classification of liquid crystals is presented here [56], [57].

We restrict our focus on thermotropic LC phases that are reached on varying temperatures ($T$). Furthermore, we consider only LCs consisting of rod-like molecules. A

typical sequence of phases in non-chiral LCs on decreasing temperature from the isotropic phase is illustrated in Figure 2.2.

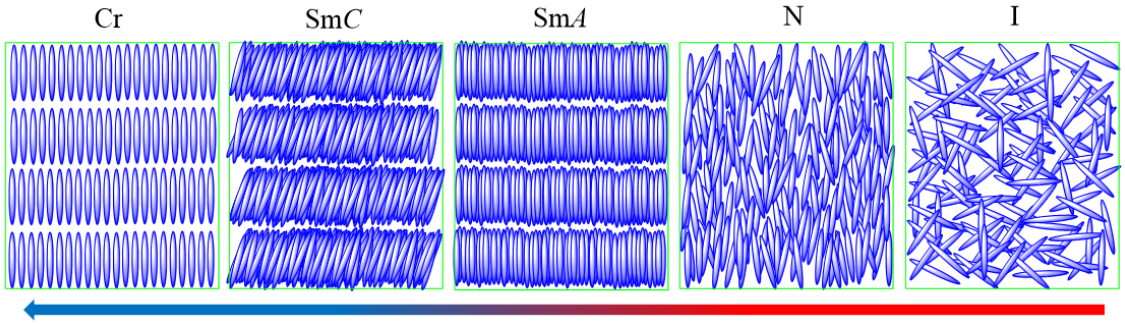


Figure 2.2: Typical phases of non-chiral LCs on decreasing temperature from the isotropic phase (I), Nematic (N), Smectic A (SmA), Smectic C (SmC), and Crystal (Cr) phase [57].

### 2.1.2 Liquid crystal phases hosting line defects

If LC order is frustrated TDs could be present [9], [58]. We henceforth restrict our focus on line defects referred to as i) disclinations and ii) dislocations. There are defects in i) orientational and ii) translational order.

Disclinations in nematic order correspond to points where $\vec{n}$ is not uniquely defined. Most common are $m = 1/2$ and $m = -1/2$ disclinations [59], [60], characterized by the winding number $m$. The latter determines the number of reorientations of $\vec{n}$ on encircling a line defect counter-clockwise. Half integers are possible due to the $\pm\vec{n}$ invariance. Their typical nematic director structure is as shown in Figure 2.3. Note that in nematic LCs the disclination core [61], [62] is in reality strongly biaxial in order to avoid the singularity at the center of the defect core.

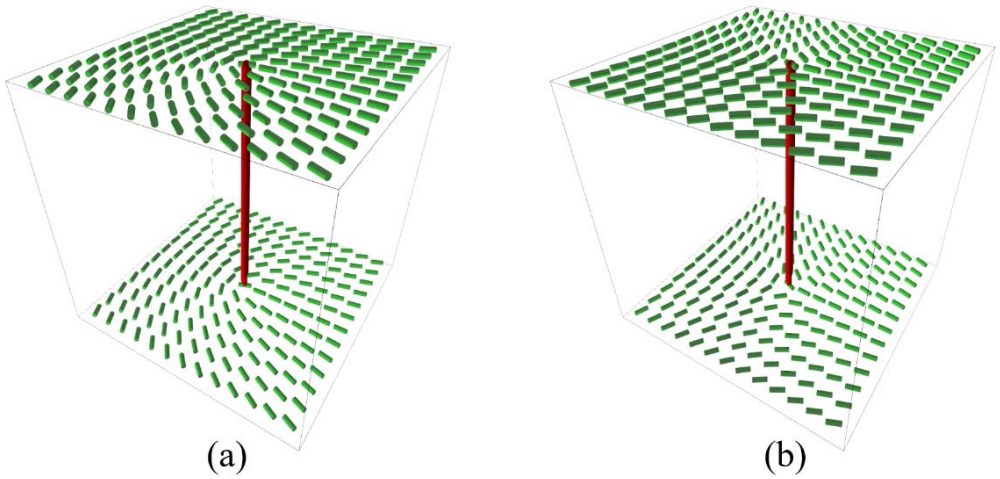


Figure 2.3: The nematic (a) $m = 1/2$ and (b) $m = -1/2$ disclination [57].

The simplest defects in translational order are screw and edge dislocations [5], [62]–[64] that are schematically depicted in Figure 2.4**.** They exhibit discontinuities in the layer order (i.e., in the symmetry breaking "phase" field). In the center of these defects, the amplitude of the smectic order parameter is melted [57].

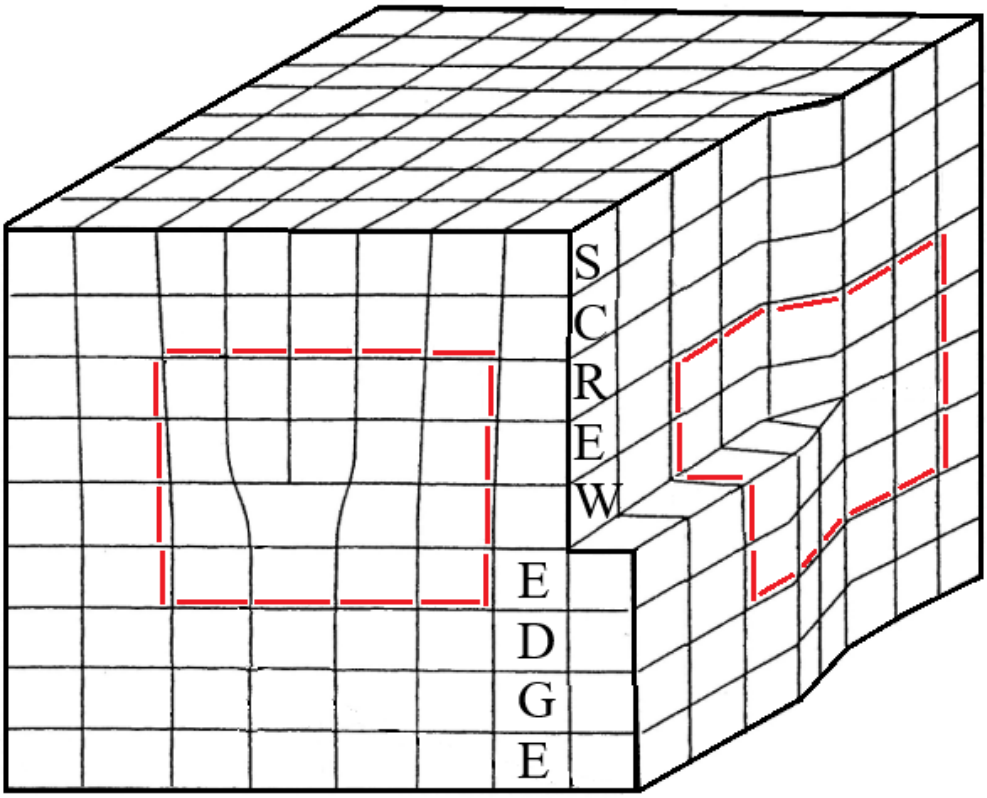


Figure 2.4: Schematic presentation of edge and screw dislocation in translational order [57].

In general, structures exhibiting lattices of line defects are not stable due to the energetically costly defect cores. A simple and efficient way to stabilize these lattices of defects is to introduce chirality into the system, which can stabilize the lattice of defects both in nematic and smectic order. We limit our review to BP [15], [16] and $TGB_A$ [17], [18] structures, in which lattices of $m = -1/2$ disclinations and screw dislocations are stable, respectively. Note that $TGB_A$ refers to a structure of grain-boundaries separating slabs of SmA order.

In chiral LCs, the nematic (N) phase is replaced by the chiral nematic ($N^*$), also referred to as the cholesteric phase [5]. This phase consists of cross-sections exhibiting nematic order, which are uniformly twisted along the perpendicular direction. Different BP configurations could be introduced between the isotropic (I) and N* phases for a strong enough chirality. Furthermore, the $TGB_A$ phase could intervene in a narrow temperature window separating the defect-less $N^*$ and SmA phases. In the following, we summarize the main features of BP and TGB configurations.

#### 2.1.2.1 Blue phases

*Reinitzer* discovered liquid crystals in 1888 [65], but the real research interest in BPs started much later in 1960s. BPs appear as a highly twisted nematic LC that cools down from the isotropic phase. In 1973 [66] *Coates* and *Gray* came up with the name "blue phases", to indicate this unusual state, and began to treat the phase as one of the LC phases. In Pioneering studies, blue phases exhibited blue colors; that is how BPs got their name. However, BPs are not always blue. They may reflect the light of other colors depending on the chirality of the LCs [67]. BPs are highly fluid self-assembled three-dimensional cubic structures [68]. Three distinct thermodynamic BP phases can exist (see

Figure 2.5 and Figure 2.6), which commonly appear in a narrow temperature interval 2-3 K between the I and the N* phase [69].

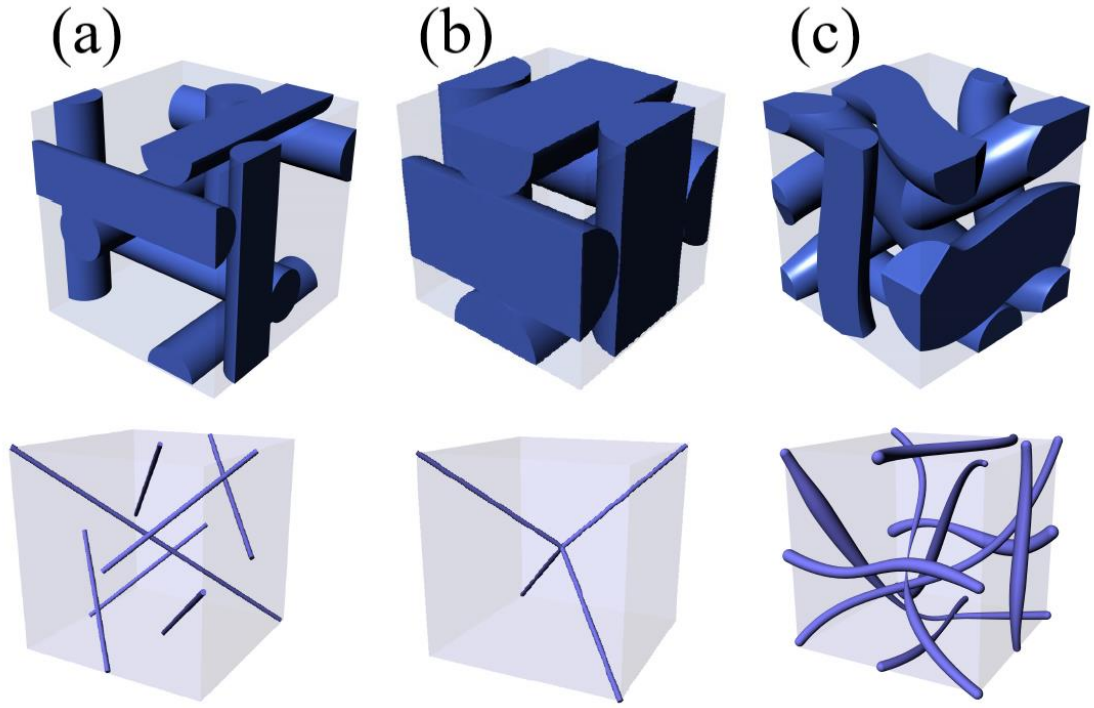


Figure 2.5: The packing of double-twist cylinders (top panel) and the structure of disclinations (bottom panel) are presented (a) BPI, (b) BPII, (c) BPIII [57].

BPs consist of double-twist cylinders that tend to be arranged mutually perpendicularly. Chiral molecules form locally the so-called "double-twist" structure, which is energetically more favorable than a single twist [70]–[72] realized in N*. However, to realize a double twist in 3D, a lattice of $m = -1/2$ disclinations needs to be introduced due to topological reasons, as illustrated in Figure 2.6. These defects form a cubic lattice, where the characteristic lattice linear scale is typically in the range of several hundred nm [70]. There are three different kinds of such phases: blue phase I (BPI), blue phase II (BPII), and blue phase III (BPIII) (Figure 2.5). BPI and BPII display a relatively high degree of translational order. BPI exhibits a cubic body-centered structure, while BPII has a simple cubic unit (i.e. the double-twist cylinders are packed in the cubic lattice) [73], [74]. On the contrary, a random network of disclination lines [75] characterizes BPIII. Consequently, BPIII possesses macroscopically the same symmetry as the I phase [74].

In the pioneering work by *Meiboom et al.* [15], the stability of BPs was explained using a simple Oseen-Frank elasticity, by using the so-called Meiboon's defect model [76].

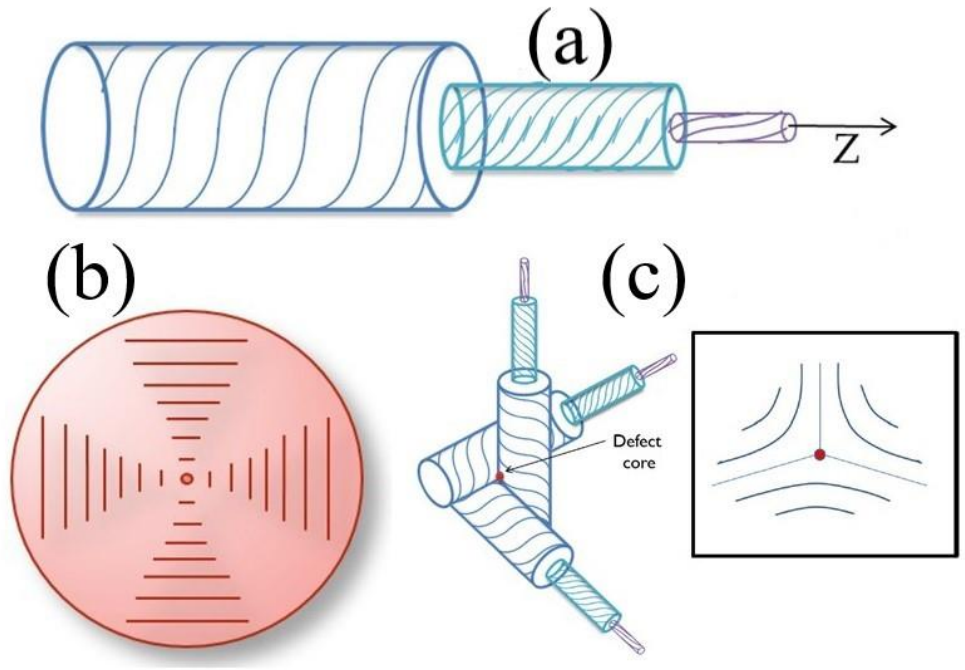


Figure 2.6: (a) A schematic presentation of a double-twist cylinder aligned along the z-coordinate is shown here. The lines indicate the nematic director field. (b) The double-twist director field in the (x, y) plane is drawn, where $\vec{n}$ points along the z-direction at the symmetry axis. (c) Double-twist cylinders topologically enforce $m = -1/2$ disclinations [57].

Due to the narrow stability range, BPs have been for a long time of interest only for fundamental studies [57], [77], [78]. However, with time the scientific community realized the BPs potential for various applications in emerging technologies [77], such as three-dimensional lasers, tunable photonic crystals, and fast optical displays [79]–[82]. In the last decades, this has initiated extensive research efforts to increase their temperature stability range. Several strategies, such as chiral doping, polymer, and nanoparticle stabilization, as well as long-time scale preservation in a supercooled state, were successfully exploited for the stabilization of BPs in wide temperature ranges [70], [78], [83]–[99].

#### 2.1.2.2 Twist-grain boundary phases

Chirality favors twist-like configurations, which are incompatible with the smectic layer-type configuration. Consequently, for large enough chirality, lattices of screw disclinations could appear in order to energetically compromise the conflicting twist elastic deformations and smectic layer order. A typical $TGB_A$ structure is shown in Figure 2.7. It consists of bulk-like smectic order blocks, where the neighboring blocks are twisted for a finite angle. This twist is enabled by a lattice of screw dislocations that reside in the so-called *grain boundaries*.

$TGB_A$ was predicted based on the mathematical analogy between smectic LCs and superconductors by *de Gennes* [100]. He claimed that both phases could be described with a complex order parameter. He demonstrated a complete analogy between the N–SmA and the normal metal-superconducting phase transition. By extending this analogy to structures possessing topological defects, *Renn* and *Lubensky* [17] proposed the $TGB_A$ configuration [101] as the LC analog to the Abrikosov flux phase appearing in type–II superconductor in the presence of an external magnetic field. Twist penetrates the $TGB_A$ structure via a lattice of screw dislocations that are roughly analogs of magnetic vortices

[102] in the type–II superconducting phase. In the latter case, an external magnetic field enforces the Abrikosov flux lattice [103].

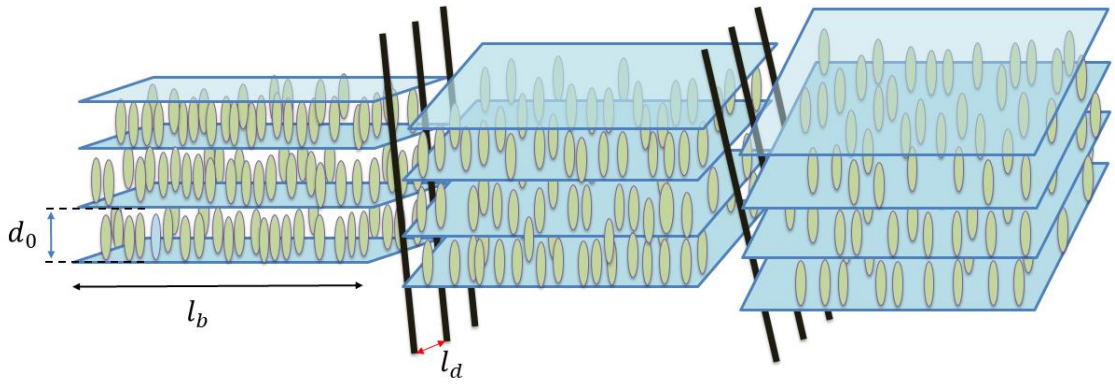


Figure 2.7: A schematic presentation of the $TGB_A$ structure. The width of smectic blocks is denoted by $l_b$, and the distance between neighboring screw dislocations by $l_d$ [57].

Different types of TGB phases are distinguished based on the type of smectic ordering within the blocks. Therefore [104]–[106], $TGB_A$, $TGB_C$, or $TGB_C^*$ configurations, exhibit within blocks SmA, SmC, or $SmC^*$ order, respectively [18], [107], [108].

Furthermore, the TGB phase could melt to a chiral line liquid just as the Abrikosov phase melts to a directed line liquid, as predicted by *Kamien* and *Lubensky* [109]. They predicted the existence of a short-range TGB structure, corresponding to a liquid of screw dislocations. This phase is referred to as the chiral line liquid ($N_L^*$). Note that TGB and $N_L^*$ are not thermodynamically distinct phases, because they share the same phase symmetry. However, they differ in the range of translational order [102].

Experimentally, *Goodby et al.* discovered the TGB phase in 1989 [18], [107]. The optical properties of this phase are similar to the $N^*$ phase. *Srajer et al.* [110] showed that this phase's small-angle x-ray structure factor displays a continuous ring, which is consistent with the model of *Renn* and *Lubensky* [108]. The existence of the lattice of screw dislocations was confirmed by the freeze-fracture measurements of *Ihn et al.* [111]. The phase sequence $N^*$–$TGB_A$–SmA was first detected by *Lavrentovich et al.* [112]. Different TGB and $N_L^*$ structures have been reported in Ref. [104], [105].

## 2.2 Phenomenological Model

In the following, a simple phenomenological description of the LC ordering is presented. For this purpose, the Landau-de Gennes-Ginzburg [113] type phenomenological description of LC ordering is used.

### 2.2.1 Order parameter

The nematic uniaxial phase is the simplest LC structure and exhibits long-range orientational order. The latter is at the mesoscopic level commonly described by the traceless and symmetric nematic tensor order parameter [5]

$$Q = \sum_{i=1}^{3} s_i \vec{e}_i \otimes \vec{e}_i. \tag{2.1}$$

Here $s_i$ are eigenvalues (the amplitude fields) and $\vec{e}_i$ are eigenvectors (the symmetry-breaking fields) of $Q$. In the case of biaxial states, all the eigenvalues are different. We

consider LCs, which is bulk equilibrium display uniaxial order. In this case, $Q$ is commonly expressed as [5]

$$Q = s\left(\vec{n} \otimes \vec{n} - I_{(d)}/3\right). \tag{2.2}$$

Here $\vec{n}$ is the nematic director (symmetry breaking) field, $s$ is the nematic order parameter (amplitude) field and $I_{(d)}$ is the identity matrix. $\vec{n}$ points along with the average local orientation of rod-like LC molecules, where the states $\pm\vec{n}$ are physically equivalent, and $|\vec{n}| = 1$. The degree of ordering is described by the uniaxial order parameter (amplitude) field $s$, where $s \in [-\frac{1}{2}, 1]$. In the bulk equilibrium, the nematic order is spatially homogeneous, positive and $\vec{n}$ points along a symmetry-breaking direction.

On further decreasing $T$, smectic phases typically occur that additionally possess positional quasi-long-range order. In equilibrium, they form a stack of parallel and equidistant smectic layers. Depending on the molecular order in layers one distinguishes among different smectic phases. The simplest is the SmA phase, where LC molecules tend to be aligned parallel to the smectic layer normal. In the bulk SmA equilibrium, the layers are stacked along the spatially homogeneous $\vec{n}$. In the simplest approach, the layer ordering is described by the mesoscopic order parameter field $\Psi$ [5], [100]

$$\Psi = \eta e^{i\phi}, \tag{2.3}$$

where $\eta$ and $\phi$ represent the translational amplitude and symmetry-breaking field, respectively. It approximately describes the mass density spatial variation $\rho = \rho_0(1 + \Psi + \Psi^*)$, where $\rho_0$ is a constant. In bulk equilibrium $\eta$ is spatially homogeneous, $\phi = q_0\vec{n}.\vec{r}$ and the periodicity $q_0 = 2\pi/d_0$ determines the smectic layer spacing $d_0$. The orientational ordering is described in terms of the nematic tensor order parameter $Q$. In the uniaxial approximation, where biaxial effects are neglected, the order parameter is conventionally expressed [113] by Eq. (2.1). This description considers both uniaxial and biaxial states. In the latter case, the nematic LC order is elastically distorted. Most of the thesis will consider only uniaxial nematic order, which is Eq. (2.2) in terms of amplitude $s$ and the nematic director field $\vec{n}$.

The SmA layering is described in terms of the complex order parameter given by Eq. (2.3) in terms of the smectic layer amplitude $\eta$ and the smectic phase $\phi$.

For the layers staked along the wave vector $\vec{q}_0$, the phase is given by $\phi(\vec{r}) = \vec{q}_0 \cdot \vec{r}$. The translational order-parameter field $\eta$ reveals the degree of translational ordering. The relation $\eta(\vec{r}) = 0$ signals absence of local translational ordering.

### 2.2.2 Free energy

A thermotropic LC exhibiting either the I–N–SmA or the I–SmA phase transitions is considered below. The free energy $F$ of the confined LC is expressed as

$$F = \int \left(f_h^{(n)} + f_h^{(s)} + f_e^{(n)} + f_e^{(s)} + f_c\right) d^3r + \int \left(f_i^{(n)} + f_i^{(s)}\right) d^2r, \tag{2.4}$$

where the volume integral runs over the LC body and the surface integral over the LC confining substrate. In the simplest case of the isotropic elasticity and in the lower-order approximation (with respect to the order-parameters expansions), the free energy densities are expressed as

$$f_h^{(n)} = \frac{3}{2}a_0^{(n)}(T - T_*)TrQ^2 - \frac{9}{2}b^{(n)}TrQ^3 + \frac{9}{2}c^{(n)}(TrQ^2)^2, \tag{2.5}$$

$$f_h^{(s)} = a_0^{(s)}(T - T_{NA})|\Psi|^2 + b^{(s)}|\Psi|^4, \tag{2.6}$$

$$f_e^{(n)} = L_1 Q_{ij,j} Q_{ie,e} + L_2 Q_{ij,k} Q_{ij,k} + L_3 Q_{ie,j} Q_{ji,e} + q L_c \epsilon_{ijk} Q_{in} Q_{jn,k}, \tag{2.7}$$

$$f_e^{(s)} = C_{\parallel}|(\vec{n} \cdot \nabla - iq_0)\Psi|^2 + C_{\perp}|(\vec{n} \times \nabla)\Psi|^2, \tag{2.8}$$

$$f_c = -D\nabla\Psi \cdot Q\nabla\Psi^*, \tag{2.9}$$

$$f_i^{(n)} = W_n^{(1)}\vec{v} \cdot Q\vec{v} + W_n^{(2)} Tr(Q - Q_i)^2, \tag{2.10}$$

$$f_i^{(s)} = -\frac{W_s^*\Psi + W_s\Psi^*}{2}. \tag{2.11}$$

The homogeneous nematic $f_h^{(n)}$, smectic $f_h^{(s)}$, and the coupling $f_c$ term determine the equilibrium value of the nematic $\left(s(\vec{r}) = S_{eq}\right)$ and smectic $\left(\eta(\vec{r}) = \eta_{eq}\right)$ order parameters in a bulk homogeneous sample. The quantities $a_0^{(n)}, b^{(n)}, c^{(n)}, T_*, a_0^{(s)}, b^{(s)}, D,$ and $T_{NA}$ are positive material constants.

If the smectic and nematic orders are decoupled $(D = 0)$ the phase behavior of the system is as follows. The quantity $T_*$ determines the supercooling temperature of the isotropic phase. The I-N transition takes place at $T_{IN} = T_* + \frac{b^{(n)2}}{24a_0^{(n)}c^{(n)}}$, $S_{eq}(T < T_{IN}) = S_0\frac{3+\sqrt{9-\frac{8(T-T_*)}{T_{IN}-T_*}}}{4}$, where $S_0 = S_{eq}(T = T_{IN}) = \frac{b^{(n)}}{4c^{(n)}}$. The SmA phase is reached at $T = T_{NA}$, $\eta_{eq}(T < T_{NA}) = \eta_0\sqrt{\frac{T_{NA}-T}{T_{NA}}}$, where $\eta_0 = \sqrt{\frac{T_{NA}a_0^{(s)}}{2b^{(s)}}}$.

The elastic term $f_e$ penalizes the departures from the bulk equilibrium ordering. The quantities $L_1, L_2, L_3, L_c$ and $C_{\parallel}$ and $C_{\perp}$ stand for the bare nematic and smectic elastic constants, respectively. The elastic term $L_c$ enforces chirality to the system, favoring the periodicity $q$. The quantity $\epsilon_{ijk}$ is the Levi-Civita symbol. It equals one for even permutations of indices –1 for odd combinations and equals zero in other order. The smectic elastic terms $f_e^{(s)}$ favor (i) homogeneous orientational ordering, (ii) parallel alignment of $\vec{n}$ and the normal $\vec{v}_s$ of a smectic layer, and (iii) the bulk layer distance $d_b = 2\pi/q_o$. Therefore, in the equilibrium one obtains $\phi = \phi_{eq} = q_0\vec{r} \cdot \vec{n}$.

The coupling of LC ordering with the confining surface is described by the nematic $(f_i^{(n)})$ and smectic $(f_i^{(s)})$ interface terms, where $W_n^{(1)}$, $W_n^{(2)}$and $W_s$ stands for the nematic and smectic anchoring terms and $\vec{v}$ is the normal vector of the interface. Note that for different surface treatments we have different surface interaction terms. In Eq. (2.10) and Eq. (2.11), we write the most common interactions used in the literature. $W_n^{(1)} > 0$ favors perpendicular orientation of LC molecules with respect to $\vec{v}$ (the isotropic tangential anchoring condition). Relation $W_n^{(1)} < 0$ favours the orientation of the molecules along $\vec{v}$ (the homeotropic anchoring condition). If $W_n^{(2)} > 0$ is a dominant term, then it enforces surface-imposed order equal to $\mathrm{Q_i}$. The confining surface tends to increase the degree of smectic ordering is $W_s$ and $W_s^*$ are positive.

## 2.3 Topological Defects Stabilization Mechanism

Here, we present the key mechanisms that generate lattices of line defects. For simplicity, we restrict to the nematic uniaxial order.

The resulting free energy density is expressed as

$$f_h^{(n)} \sim a^{(n)}(T - T_n^*)s^2 - b^{(n)}s^3 + c^{(n)}s^4, \tag{2.12}$$

$$f_e^{(n)} \sim L|\nabla s|^2 + \frac{K_1}{2}(\nabla.\vec{n})^2 + \frac{K_2}{2}(\vec{n}.\nabla\times\vec{n} - q)^2 + \frac{K_3}{2}|\vec{n}\times\nabla\times\vec{n}|^2 - \frac{K_{24}}{2}\nabla.(\vec{n}\nabla.\vec{n} + \vec{n}\times\nabla\times\vec{n}), \tag{2.13}$$

$$f_h^{(s)} \sim a^{(s)}(T - T_s^*)\eta^2 + b^{(s)}\eta^4 + c^{(s)}\eta^6, \tag{2.14}$$

$$f_e^{(s)} \sim C_\parallel|(iq_0\vec{n} - \nabla)\Psi|^2 + C_\perp|(\vec{n}\times\nabla)\Psi|^2, \tag{2.15}$$

where the orientational and translational order are described in terms of order parameters given by Eqs. (2.2) and (2.3). In expressing $f_e^{(n)}$ we use the conventional Frank description in terms of the Frank splay $K_1$, twist $K_2$, bend $K_3$ and saddle-splay $K_{24}$ elastic constant. It roughly holds that these constants are proportional with $LS^2$, where $L \sim L_1 = L_2 = L_3$ [114].

### 2.3.1 Curvature

We first discuss the conditions favoring BPs that are characterized by lattices of disclinations. The main ordered phase that appears as a competitor of BPs is the $N^*$ phase. The latter is characterized by the twist nematic configuration, for which $f_e^{(n)} \sim 0$. On the contrary, in BPs, the first four elastic contributions in Eq. (2.13) are on average finite and positive. In addition, disclinations require melting (more exactly, the appearance of biaxial states) of the uniaxial nematic order in the cores of defects, introducing additional condensation penalty costs in BPs. The key BP stabilizing term is thus the saddle-splay term for the positive value of $K_{24}$. Note that the elastic term weighted by $K_{24}$ equals the Gaussian curvature $G$ of a hypothetical local surface [5], whose surface normal is determined by $\vec{n}$. Therefore, $K_{24} > 0$ favors "double-cylinders" which are characterised by $G > 0$, decreasing the overall free energy. However, in between "double-twist cylinders" the LC structure exhibits regions where $G < 0$. Nevertheless, the free penalty in these regions is relatively small due to the presence of disclinations that, on average, decrease the amplitude of nematic local order. The overall energy penalty balance favors the presence of disclinations.

In the case of smectic order, the smectic compressibility term represents the generator of dislocations. In order to show that, we assume a spatially constant value of the smectic amplitude field $\eta$. Consequently, the minimization of the compressibility terms yields the condition

$$q_0\vec{n} = \nabla\phi. \tag{2.16}$$

Applying the operation $\nabla\times$ on Eq. (2.16), one obtains $q_0\nabla\times\vec{n} = \nabla\times\nabla\phi \equiv 0$, which leads in strongly chiral LCs to inequality, because of $\nabla\times\vec{n} \neq 0$. One could resolve this frustration either by melting the smectic order or by introducing dislocations. Note that in

superconductors [115] one obtains a similar inequality, where $\vec{A}$ (which is related to the magnetic field $\vec{B} = \nabla \times \vec{A}$) plays the role of $\vec{n}$, and $\phi$ is the phase of the complex order parameter quantifying the condensation of the superconducting Cooper-pairs.

### 2.3.2 Nanoparticles

Introducing NPs or other agents such as polymeric molecules to LC structures hosting lattices of defects could efficiently enhance the stability of such structures. The key mechanisms enabling the stabilization are referred to as the Defect Core Replacement (DCR) [92], [99], [116] and the Adaptive Defect Core Targeting (ADCT) [14] mechanisms.

The DCR mechanism refers to the partial replacement of the relatively expensive TD cores volume with the volume of (partially) trapped NPs. Within the cores of disclinations and dislocations, the uniaxial nematic order and smectic order, respectively, are essentially melted [61], [64], [117]. This generally introduces relatively high energy costs in the respective condensation-free energy contributions. However, if NPs are trapped within the cores, the free energy condensation penalty is reduced. In order to illustrate this, the condensation penalty $\Delta F_c^{(phase)}$ for introducing defects into BP or TGB phase is estimated by

$$\Delta F_c^{(BP)} \sim \left| f_h^{(n)} \right| V_{def}, \tag{2.17}$$

$$\Delta F_c^{(TGB)} \sim \left| f_h^{(s)} \right| V_{def}, \tag{2.18}$$

where $V_{def}$ estimates the total volume of defect cores within a system, and the condensation free energy contributions are given in Eq. (2.12) & (2.14). If NPs are trapped within the cores, they reduce the value of $V_{def}$.

Note that the above-described mechanism is effective only when the NPs do not significantly distort the surrounding symmetry-broken order parameter field component (i.e. the nematic director field $\vec{n}$ or the smectic phase-field $\phi$), which is embodied in the universal ADCT mechanism. This mechanism refers to cases, where the same NPs stabilize both lattices of disclinations and dislocations [14]. It incorporates the following characteristics: i) NPs should slightly distort the symmetry-broken field of the LC structure to be attracted to a defect's core. ii) If NPs are trapped within the cores they should not significantly distort the surrounding LC order. iii) In order to have a universal impact on both disclinations and dislocations, NPs should have the potential to adapt to the structure of different environments. This last condition is met when NPs have an appropriate surface treatment [14], [99], [116].

The ADCT mechanism is effective only when the NP-LC interaction is moderate, i.e., neither weak nor strong. To estimate this condition in the nematic phase, the coupling at NP-LC interfaces is modeled by the free energy density term [5] (see Eq. (2.10))

$$f_i = w\, Tr(Q - Q_i)^2. \tag{2.19}$$

Here $Tr$ stands for the trace operation, $w > 0$ stands for the positive surface anchoring-wetting constant, and $Q_i$ is the nematic order favored by the interface. The appropriate regime enabling adaptivity is where the global interface and elastic penalty contributions are comparable. To obtain an estimate for such a condition [118], one compares the average free energy $\Delta F$ penalties in extreme cases, where either i) elastic or ii) surface interaction penalties are minimised. In the first case, the surface interaction contribution is maximal and is estimated by $\frac{\Delta F^{(i)}}{V} \sim \frac{N}{V} a_{NP} w \sim p \frac{a_{NP}}{v_{NP}} w$. Here N stands for the number of NPs in the

sample, $a_{NP}$ and $v_{NP}$ determine the average surface area and volume of a NP, and $p = \frac{Nv_{NP}}{V}$ is the volume concentration of NPs. In the second regime, the interface penalties are negligible and the free energy penalties are dominated by the elastic deformations, which arise in order to accommodate NP-LC interfaces-imposed order. It follows [118] that $\frac{\Delta F^{(ii)}}{V} \sim \frac{K}{l_{NP}^2}$, where $K$ is the representative Frank elastic constant and $l_{NP} \sim (v_{NP}/p)^{1/3}$ is the average separation between essentially homogeneously dispersed NPs. The adaptive regime is estimated by imposing $\Delta F^{(i)} \sim \Delta F^{(ii)}$, yielding the condition

$$p \frac{a_{NP}}{v_{NP}} \frac{l_{NP}^2}{d_e} \sim 1, \tag{2.20}$$

where $d_e \sim K/w$ defines the surface extrapolation length. For spherical NPs of radius $r$ it follows

$$\frac{p^{2/3} r}{d_e} \sim 1. \tag{2.21}$$

For example, this condition is fulfilled for $w \sim 10^{-6}$ J/m$^2$ in case of conventional LCs [5] (i.e. $K \sim 10^{-12}$ J/m), spherical NPs of radius $r \sim 10$ nm and concentration $p \sim 0.001$.

It is noteworthy that lattices of defects could also be stabilized by other mechanisms, e.g., by effectively enhancing the chirality strength of the system [68]. This could be achieved by using appropriate chiral dopants.

# Chapter 3

# Experimental Background

We have used synthesized magnetic NPs and various experimental methods to characterize them in the present work. Transmission electron microscopy (TEM) has been used for the particle's shape, size distribution, and surface morphology. Dynamic light scattering (DLS) is used to determine the size distribution profile of tiny particles in colloidal suspension. Furthermore, the phase behavior of LC+NP mixtures has been probed utilizing ACC, POM. To distinguish between various phases in the LCs and successive mixtures with magnetic NPs, polarized optical microscopy (POM) and high-resolution calorimetry (ACC) were used.

## 3.1 Materials Used

Chiral CE8 liquid crystal compound was used in this thesis. More specifically, the impact of NPs on the stabilization of phase behaviors was studied in a mixture of chiral CE8 and magnetic NPs with three different concentrations.

### 3.1.1 Liquid crystal compound

A strongly chiral LC compound S-(+)-[4-(2'-methyl butyl) phenyl 4'-n-octylbiphenyl-4-carboxylate] known as CE8 has been used.

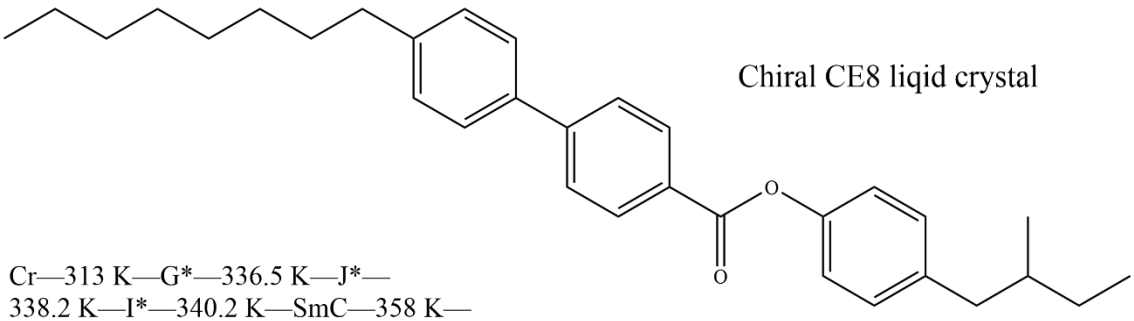


Cr—313 K—G*—336.5 K—J*—
338.2 K—I*—340.2 K—SmC—358 K—
SmA—401.1 K—N*—412.1 K—BPI—415.6—BPII—416.1 K—BPIII—417.7 K—I.

Figure 3.1: The chemical structure of chiral liquid crystal CE8 and its phase sequence [99].

It was purchased from Merck and used without further treatment. CE8 compound was used for the stabilization of blue phases by using NPs [85], [86], [99], [116]. The present ferroelectric chiral LC exhibits the following phase sequence as obtained from the bulk CE8 calorimetric run [119], as you can see below.

### 3.1.2 Magnetic nanoparticles

Mixtures of LCs and NPs have been extensively studied, both experimentally and theoretically [120]–[124]. Recently, different types of LC and NP mixtures were exploited for the tuning of the electro-optical response [120] and phase stabilization [85], [95], [98], [116], [125]–[127]. Nowadays, magnetic NPs are of great interest for researchers and they have tried to produce new NPs exhibiting extraordinary properties [128]. Knowing that NPs mixtures and other conventional materials could exhibit special behaviors not found in any individual components [4]. It has been shown experimentally [129], [130] that the spontaneous onset of LC ordering could be a way to obtain well-aligned NPs [53]. It is well known that LC exhibits a long-range orientational order, and it responds extremely to various perturbations as an external field (e.g. electric or magnetic) [128].

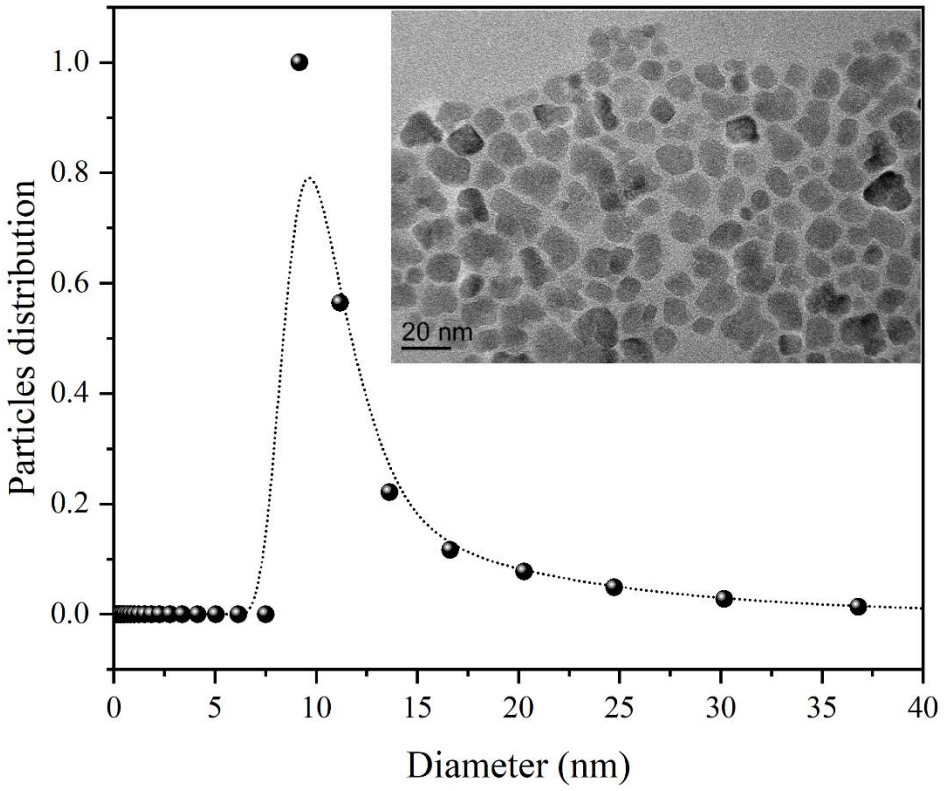


Figure 3.2: DLS image of maghemite ($\gamma - Fe_2O_3$) magnetic nanoparticles (the insert: TEM image of magnetic NPs).

The chosen magnetic NPs were maghemite ($\gamma$-$Fe_2O_3$) nanoparticles with an average diameter around 10 nm. The NPs have been synthesized by Dr. Sašo Gyergyek, Department for Synthesis of Materials, IJS. Briefly, the NPs were synthesized by co-precipitation of Fe(II) and Fe(III) cations with ammonia, followed by adsorption of oleic acid (OA) [131]. The addition of HNO3 flocculated the hydrophobized NPs. The particles were soaked in OA for coating, and the excess acid was removed by washing NPs with acetone. Finally, the NPs were dispersed in an equal amount of toluene and chloroform to form a colloidal suspension. The average size $d_{TEM}$ of the NPs was estimated from TEM images of at least 500 NPs (Figure 3.2) and was found to be $d_{TEM} = 10\,nm \pm 2\,nm$. The hydrodynamic diameter $d_{DLS}$ = 10.5 nm of the NPs was estimated by DLS (Figure 3.2) and was very close to $d_{TEM}$ indicating good agreement by dispersion of the NPs in toluene.

## 3.2 Liquid Crystals and Nanoparticles Mixing

A well-known mixing protocol prepared the CE8 and magnetic NPs mixture described elsewhere [99], [132]. The NPs concentrations such as $\chi = 0.01, 0.001, 0.0001$, where $\chi$ is defined as the mass of magnetic NPs over the total mass

$$\chi = \frac{m_{NP}}{m_{NP} + m_{LC}} \tag{3.1}$$

Here $m_{NP}$ and $m_{LC}$ stand for the total masses of NPs and LC molecules in the samples. 100 mg of CE8 LC was used in each mixture and the NPs concentration was determined by the above formula (Eq. (3.1)). NPs were dispersed and stored in high-purity toluene and chloroform. The desired amount of LC and NPs solution took in a vial; additionally, 200 µL of high-purity toluene was added into a vial. Then the vial was placed on the non-magnetic heater. Since we are using magnetic NPs, we have used glass rod stirring to mix the solution. The temperature was set to 350 K and the rotation speed to 250-300 rpm while toluene was presented in the vial. The temperature was gradually increased; in the meantime, toluene was periodically added to the mixture to enable enough time for mixing to get a good mixture. The sample was set to the isotropic phase before the toluene was evaporated completely from the vial, i.e. at 430 K, and glass rod rotation speed was reduced to 100-150 rpm. Once the toluene evaporated, the mixture was mixed with a glass rod by hand for a couple of minutes. After all, the mixture was quenched immediately with cold water to keep the mixture into the crystalline phase, and then the crystalline mixture was used in further experimental techniques.

## 3.3 Experimental Techniques

In this work, we have used two different experimental techniques, namely optical microscopy and ac calorimetry, to identify the phases and check the stability of the respective phases.

### 3.3.1 Polarized optical microscopy

Optical microscopy was used to initially characterize LC+NP mixture samples. Later on, the time-consuming high-resolution calorimetric method was used. Both measurements have been used to check the presence of the desired phases in the system. The homemade extremely subtle temperature (± 0.01K) controller attached to the optical microscopy was used to identify various LC phases. Nikon ECLIPSE E600 polarized microscope has been used for the sample observations under polarizers in transmission mode, and the images were taken with the 20X imaging Canon EOS 550D camera. The temperature (i.e. heating and cooling cycles) rates under the microscope with an approximate heat rate of 0.02 K per 1 min using a heated stage with $\pm 0.1^0$ K temperature stability driven by the Lakeshore 304 K temperature controller. Non-treated glass cells were used for microscopy observations.

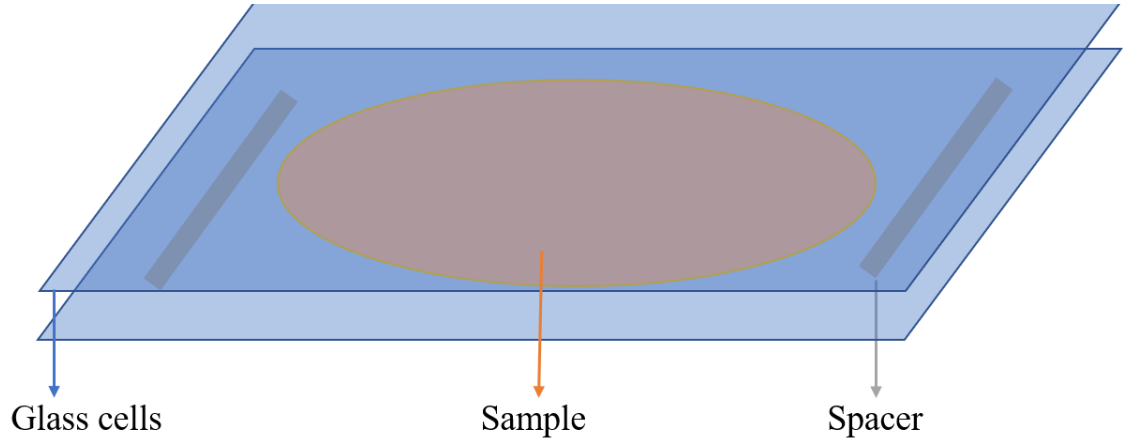


Figure 3.3: Schematic representation of LC mixture in between the glass cells and spacers for POM observations.

Afterwards, two non-treated glass plates were separated by a 12 µm thick spacer stuck together enveloping an LC and NPs mixture in between (Figure 3.3). The mixture was first re-melted into the isotopic phase and then the cell was pressed together. After this, we proceeded with the POM measurements.

### 3.3.2 High-resolution calorimetry

The temperature dependence of the heat capacity was performed by the high-resolution ac calorimetry (ACC). This is a useful technique for studying the critical behavior in the vicinity of various phase transitions. The temperature dependence of the heat capacity $C_p$ and enthalpy $H$ functions plays an important role in characterizing the phase transitions in condensed matter [133]. In the past, several known calorimetric techniques have been developed, i.e., differential scanning calorimetry (DSC) [133], traditional adiabatic calorimetry [134]–[136], adiabatic scanning calorimetry [128], isothermal titration calorimetry, and photothermal calorimetry. Besides, a variety of high-resolution scanning techniques were invented. Among them, the special technique is ac calorimetry [133], well suited for LCs and other soft and solid materials to obtain the phase transition behavior and reveal the universality class, etc. [14], [133], [135], [137]–[139].

In the present work, we have used high-resolution ac calorimetry. The ac calorimetry is sensitive mostly to the continuous enthalpy changes, while the relaxation mode is to both continuous and discontinuous enthalpy changes. Both the ac and relaxation modes can be obtained the heat capacity $C_p(T)$ in the vicinity of the selected phase transition, as well as to determine the type of critical behavior [133], [140]. The comparison of data obtained by the modes can be used to detect the latent heat when present. The latent heat at a first-order transition is derived from the difference in the total enthalpy obtained by the two modes of operation [140]. In this thesis, we performed ac runs to derive the phase diagrams and critical behavior of given mixtures.

All calorimetry measurements were performed at the setup at the Jožef Stefan Institute, Ljubljana. A homemade, dual-mode computerized calorimetry operating in both ac and relaxation modes over a broad temperature range between 80 to 470 K has been used [119], [138]. A detailed description is given below, followed by calorimeter setup, sample preparation, and mounting.

The calorimeter setup consists of a thermal bath, which includes two hermetically sealed Cu blocks, the electronic devices: Keithley 2002 digital multimeter for the data acquisition, Krohn-Hite 5920 power source and resistor for guiding heating power along with Lake

Shore temperature controller for setting and stabilizing the bath temperature within 0.1 mK and a computer control the setup as given in Figure 3.4.

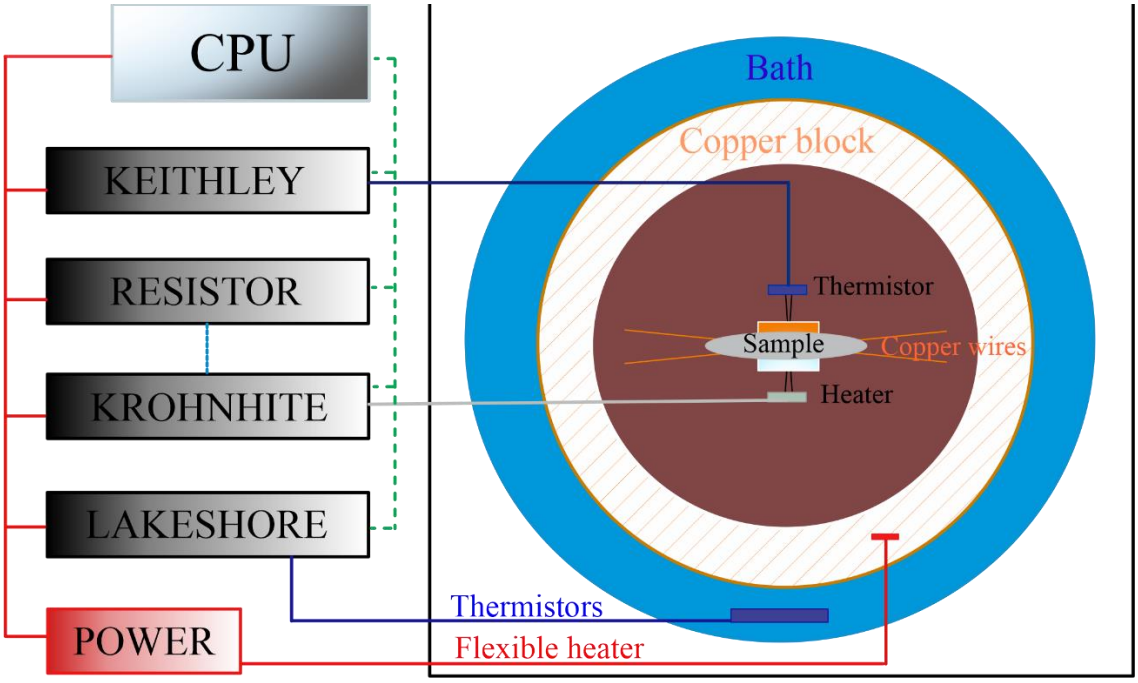


Figure 3.4: Schematic representation of home-made high-resolution calorimetry setup at IJS. The setup comprises several parts, such as electronic devices (left) connected with a computer and a thermal bath unit (right) where the sample goes. Figure 3.5 presented a real view of the thermal bath, inside view, and their connections with a sample.

For the calorimetric cell preparation, a high-purity hand-shaped silver cup and a lid need to be cleaned with acetone and ethanol by using a sonicator. Afterwards, the glue and indium paste are spread on both cup lid edges. Indium paste ensures that the cup and lid adhere well to each other when pressed together, preventing any possible sample leakage. It is important since all samples are liquid-like at higher temperatures. Then the cup is filled with the prepared LC mixture. After pressing together, the cup and the lid, additional components such as heater (down), thermistor and copper leads (top) are attached to the sample cell. One side, a 120 Ω strain-gauge, serving as a heater, and 40 µm thick supporting copper wires are attached by a special glue GE varnish.

The heater is connected to the Krohn-hite function generator and supplies the ac or linear power to the sample/cell. On the other side of the cell, a 500 kΩ small-glass-bead thermistor is attached by the Torr seal for precisely probing the temperature of the sample as in Figure 3.6. The thermistor is connected to the Keithley digital multimeter, which measures its resistivity. Another heater attached to the bath shield is connected to the Lakeshore temperature controller and serves to stabilize the bath temperature. Two additional thermometers are connected to the Lakeshore temperature controller. The computer controls the whole measurement procedure, triggers the measurement, and stores all the data collected during the experiment. The sample cell is coupled to the surrounding bath mainly through the air and connecting wires. The whole chamber is insulated from the outside environment by three thermal shields. The temperature of the internal chamber is stabilized to within ±0.1 mK by the Lakeshore 304 temperature stabilizer. The thermal resistance of the connection between the sample and the bath yields typically between 200-250 Ω.

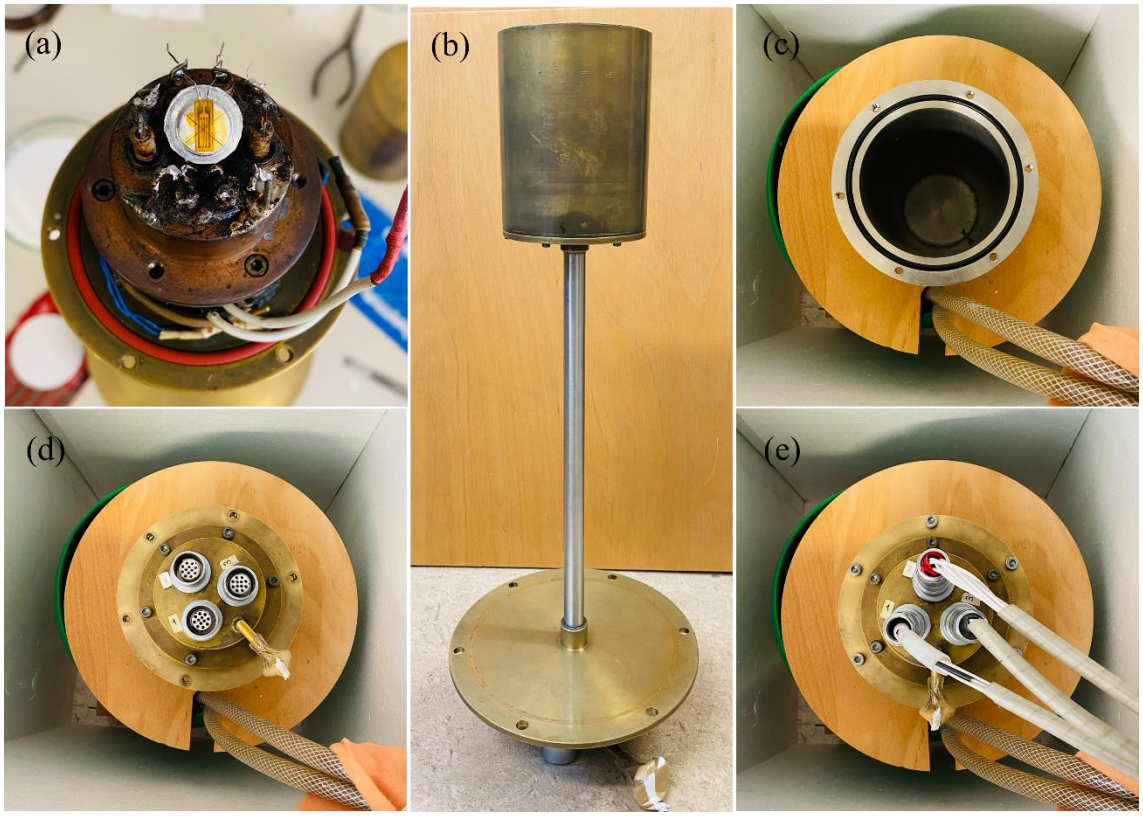


Figure 3.5: High-resolution calorimetry thermal bath setup. a) A sample cell with the attached thermistor, heater, and copper wires are mounted in the sample holder and b) then closed with a copper cover (sample holder stand). c) Thermal bath chamber, d) sample holder (b) fixed in bath chamber, and e) chamber connected with electronic devices as shown in Figure 3.4.

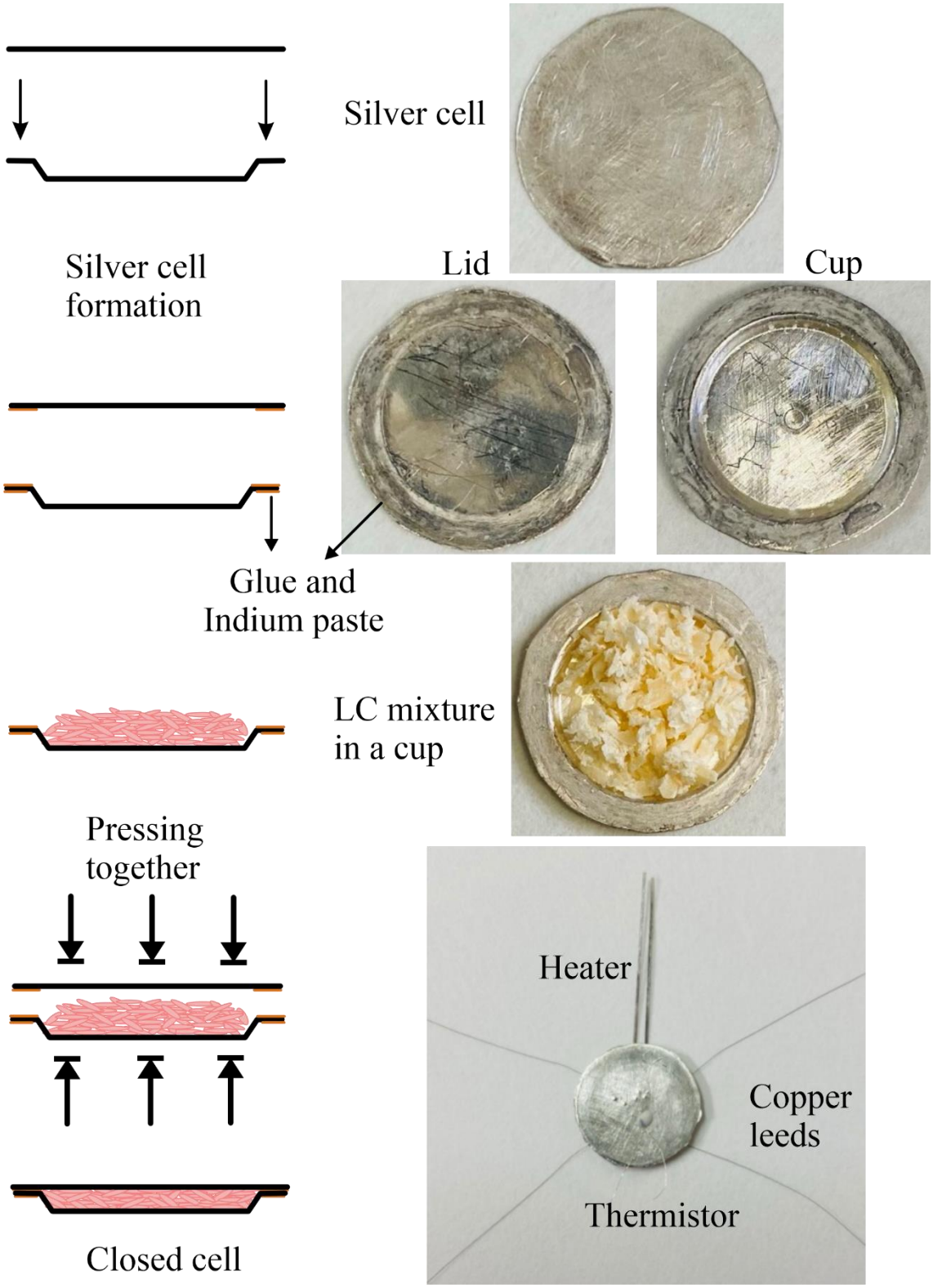


Figure 3.6: Presentation of the LC mixture cell preparation for the heat capacity measurements. The handmade silver cells (cup and lid) are prepared to place the LC mixture sample in and closed, as shown in the figure. Then the heater, copper wires, and thermistor are attached to the sample cell. At the bottom right, the final sample cell with attachments is shown.

# Chapter 4

# Results and Discussion

In this chapter, we present the obtained theoretical and experimental results. We first study the theoretically chirality-driven multiple twisted nematic structures in a cylindrical environment, such structures would in 3D lead to lattices of disclinations. We determine conditions where such nematic structures could be stable. Then we analyses theoretically how stabilized topological defects could be exploited to trap appropriately surface decorated NPs. Afterwards, we summarize and reinterpret the existing NP-driven stabilization of lattices defects in BPs and $TGB_A$. In this case, we focus on the impact of geometry of NPs. Finally, we present our detailed experimental study of the impact of spherical magnetic NPs on BPs and $TGB_A$, where we emphasize the role of the NPs magnetic field.

## 4.1 Chirality Induced Frustration

Of our interest are spontaneously twisted NLC structures in cylindrical confinement. In a 3D system, such structures of staked cylinders inevitably lead to the formation off line defects. However, within individual cylinders defects are not formed. For this purpose, it is sufficient to describe patterns using the Frank-Oseen continuum approach [141] in terms of the nematic director field $\vec{n}$ in the presence of chirality. We use the expression (see Eq. (2.7))

$$f_e = \frac{K_1}{2}(\nabla.\vec{n})^2 + \frac{K_2}{2}(\vec{n}.\nabla\times\vec{n}+q)^2 + \frac{K_3}{2}|\vec{n}\times\nabla\times\vec{n}|^2 - \frac{K_{24}}{2}\nabla.(\vec{n}\nabla.\vec{n}+\vec{n}\times\nabla\times\vec{n}). \tag{4.1}$$

We model the surface interaction term using a simple Rapini-Papoular [141] description (see Eq. (2.10)):

$$f_s = \frac{W}{2}(1-(\vec{n}.\vec{e})^2). \tag{4.2}$$

Here, $W$ stands for the surface anchoring strength and the unit vector $\vec{e}$ determines the local easy axis. Namely, $f_s$ is minimized if $\vec{n}$ is locally aligned along $\vec{e}$ for $W>0$ and perpendicular to $\vec{e}$ for $W<0$, respectively.

### 4.1.1 Representative classes of multiple-twisted structures

In the study, we focus on spontaneously twisted nematic structures realized within an infinite cylinder of radius $R$. For this reason; we use cylindrical coordinates $\{r,\varphi,z\}$,

determined by the unit vector triad $\{\vec{e}_r, \vec{e}_\varphi, \vec{e}_z\}$. We consider two different ansatzes which approximate two qualitatively different families of solutions that are expected to be stable for geometries and boundary conditions of our interest [142], [143].
The first class is parametrized as [143]

$$\vec{n}^{(RZT)} = cos\varphi\ sin\Omega\ \vec{e}_r + sin\varphi\ sin\Omega\ \vec{e}_\varphi + cos\Omega\ \vec{e}_z, \tag{4.3}$$

$$\varphi = q_1^{(RZT)} z - \varphi, \Omega = \frac{\pi}{2} - q_2^{(RZT)} r\ sin\varphi, \tag{4.4}$$

where the wave vectors $q_1^{(RZT)}$ and $q_2^{(RZT)}$ are variational parameters. A typical representative structure is shown in Figure 4.1a.

In the Cartesian coordinates $\{x, y, z\}$ the ansatz reads

$$\vec{n}^{(RZT)} = \cos\left(q_1^{(RZT)} z\right) sin\Omega\ \vec{e}_x + \sin(q_1^{(RZT)} z)\ sin\Omega\ \vec{e}_y + cos\Omega\ \vec{e}_z. \tag{4.5}$$

Cases $q_1^{(RZT)} \neq 0$ and $q_2^{(RZT)} \neq 0$ determine double-twisted solutions. In these patterns, referred to as *radially–z–twisted* (RZT) structures [143], twist deformation is realized both along the $\vec{e}_r$ and $\vec{e}_z$ directions. Furthermore, this ansatz encompasses also single-twisted structures. For example, for $q_2^{(RZT)} = 0$ a structure twisting around the y axis is expressed as

$$\vec{n}^{(RZT)} = \cos(q_1^{(RZT)} z - \varphi)\ \ \vec{e}_r + \sin\left(q_1^{(RZT)} z - \varphi\right)\ \vec{e}_\varphi, \tag{4.6}$$

which corresponds to a classical cholesteric solution with periodicity $q_1^{(RZT)}$.

This solution corresponds to a classical cholesteric solution, where the twist is realized along the z-axis.

The second family of solution of our interest corresponds to the *radially-twisted* (RT) structures [143], where the twist is realized only along $\vec{e}_r$, see Figure 4.1b. For this purpose, we use the ansatz

$$\vec{n}^{(RT)} = sin\Omega\ \vec{e}_\varphi + cos\Omega\ \vec{e}_z. \tag{4.7}$$

Here, $\Omega = \Omega(r)$ and to avoid a singularity at the cylinder axis, we impose the condition $\Omega(0) = 0$. Previous numerical studies [143] have revealed that the dependence of $\Omega(r)$ is roughly linear in $r$, even for large twists of $\vec{n}$. Consequently, we use the approximation

$$\Omega = q^{(RT)} r. \tag{4.8}$$

A typical spatial profile of these functions is presented in Figure 4.1.

We now impose the approximation of equal elastic constants $K \equiv K_1 = K_2 = K_3$, but allow $K_{24} \neq K$. At the cylinder's lateral wall, $r = R$, we impose for the positive anchoring strength $W>0$ either a) homeotropic anchoring $(\vec{e} = \vec{e}_r)$, b) planar tangential anchoring along $\vec{e}_z$ (i.e., $(\vec{e} = \vec{e}_z)$, or c) planar tangential anchoring along $\vec{e}_\varphi (\vec{e} = \vec{e}_\varphi)$. We henceforth refer to these cases as a) *homeotropic*, b) *zenithal polar planar)*, and c) *azimuthal planar* anchoring, respectively. For $W < 0$, these cases correspond to isotropic tangential anchoring in planes characterized by surface normal along $\vec{e}$. Note that in our study, the latter case is sensible only for the condition (a).

For later convenience, we introduce the following dimensionless quantities: $Q = qR, Q_1 = q_1^{(RZT)}R, Q_2 = q_2^{(RZT)}R, Q_{RT} = q^{(RT)}R, K_{24} = \frac{k_{24}}{K}, w = \frac{RW}{K}$ and the dimensionless free energy is scaled in units of $F_0 = \pi KH$. We note that $W$, and thus $w$, can differ for each of the three types of anchoring. Therefore $F \to F/F_0$, where $H$ is the height of the cylinder. For numerical convenience, we suppose that $H$ is either large in comparison with the period $p = 2\pi/q_1^{(RZT)}$, or an integer number of $p$.

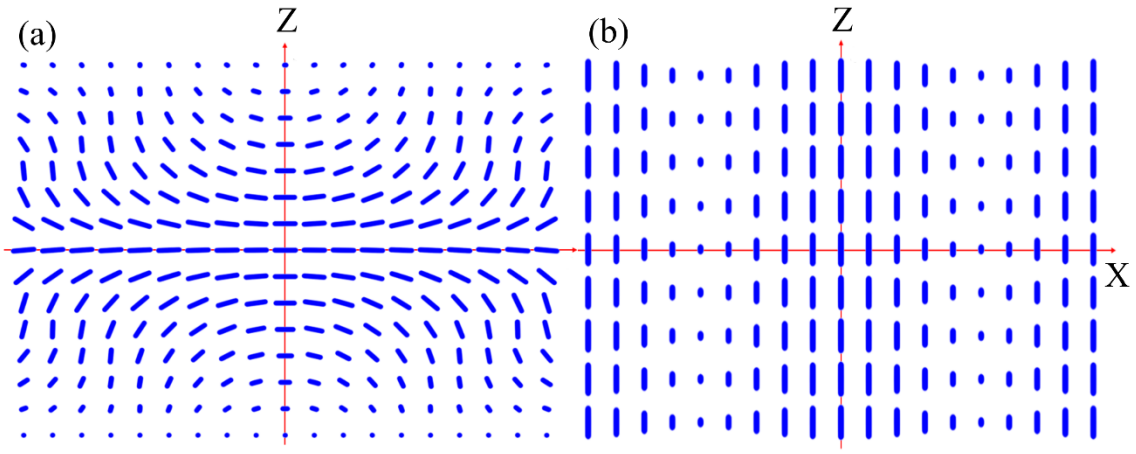


Figure 4.1: Double-twisted nematic structures. (a) The radially-z-twist deformation. $Q_1 = 1.0$, $Q_2 = 1.0$ twist is realised both along the $\vec{e}_\varphi$ and $\vec{e}_z$ directions. (b) The radially twisted structure. Here, the twist is realized along $\vec{e}_r$. $Q_{RT} = 1.1$. We present the figures in (x, z) plane [144].

#### 4.1.1.1 Free energies of structures

Using the ansatzes Eqs. (4.3) & (4.4) and Eqs. (4.7) & (4.8) and the scaling described above, we calculate free energies $F$ of the structures (see Eqs. (4.3) & (4.4)). For later convenience, the energies are decomposed as $F^{(RZT)} = F_e^{(RZT)} + F_s^{(RZT)}$ and $F^{(RT)} = F_e^{(RT)} + F_s^{(RT)}$ for the first (RZT) and second class (RT) of solutions, respectively.

We consider first the family of solutions labeled by $\vec{n}^{(RZT)}$ (see Eqs. (4.3) & (4.4)). The elastic contribution reads

$$F_e^{(RZT)} = \frac{(Q-Q_2)^2}{2} + \frac{Q_1^2 Q_2^2}{8} + \frac{Q_1}{2}\left(\frac{Q_1}{2} + (1-k_{24})Q_2 - Q\right)\left(1 + \frac{J_1(2Q_2)}{Q_2}\right). \tag{4.9}$$

Now let $F_s^{(RZT)}$ stand for the interface contribution, which is different for a) homeotropic ($F_s^{(RZT)} = F_{s,h}^{(RZT)}$), b) zenithal ($F_s^{(RZT)} = F_{s,z}^{(RZT)}$), and c) azimuthal $F_s^{(RZT)} = F_{s,\varphi}^{(RZT)}$ anchoring:

$$F_{s,h}^{(RZT)} = \frac{3w}{4} - \frac{w}{4}\frac{J_1(2Q_2)}{Q_2}, \tag{4.10}$$

$$F_{s,z}^{(RZT)} = \frac{w}{2} - \frac{w}{2}J_0(2Q_2), \tag{4.11}$$

$$F_{s,\varphi}^{(RT)} = \frac{3w}{4} + w\left(\frac{J_1(2Q_2)}{4Q_2} - \frac{J_0(2Q_2)}{2}\right). \tag{4.12}$$

Here $J_0$ and $J_1$ stand for the Bessel functions of order 0 and 1, respectively.

The second class of solutions is determined by the elastic term

$$F_e^{(RT)} = \frac{1}{2}(Q + Q_{RT})^2 + \left(1 - k_{24} + \frac{Q}{Q_{RT}}\right) sin^2 Q_{RT} + \int_0^1 \frac{sin^2(Q_{RT}x)}{x} dx, \quad (4.13)$$

and surface contributions

$$F_{s,H}^{(RT)} = w, \quad (4.14)$$

$$F_{s,z}^{(RT)} = w\, sin^2 Q_{RT}, \quad (4.15)$$

$$F_{s,\varphi}^{(RT)} = w\, cos^2 Q_{RT}. \quad (4.16)$$

We obtain solutions by varying the variational parameters $Q_1, Q_2$ and $Q_{RT}$ for given material properties (determined by $Q, k_{24}, w$) and boundary conditions.

Of interest is the determination of regimes where radially– $z$–twisted (RZT) or radially-twisted (RT) structures are stable. We first perform an analytic analysis of structures where we expand the free energies in the limit of relatively small dimensionless wave numbers $Q_1, Q_2$ and $Q_{RT}$ . Then we shall perform a more detailed stability analysis numerically.

#### 4.1.1.2 Landau-type analysis

We first consider RZT (class 1) structures using the ansatz Eqs. (4.3) & (4.4). By minimizing the total free energy $F^{(RZT)}$ with respect to $Q_1$ it follows that

$$Q_1 = \frac{Q + (k_{24} - 1)Q_2}{1 + \frac{Q_2^2}{2\left(1 + \frac{J_1(2Q_2)}{Q_2}\right)}}. \quad (4.17)$$

This relation is independent of the boundary condition because $F_s^{(RZT)}$ (see Eqs. (4.10), (4.11) & (4.12)) is independent of $Q_1$.

Hereinafter, we limit to regimes of relatively low periodicities $Q_2$ (i.e. $Q_2 \ll 1$), for which Eq. (4.17) yields

$$Q_1 \sim Q + (k_{24} - 1)Q_2 - \frac{Q_2^2 Q}{4}. \quad (4.18)$$

Taking this into account, we expand $F^{(RZT)}$ up to the fourth power in $Q_2$. It follows that

$$F_h^{(RZT)} = \frac{w}{2} + \frac{(Q - Q_2)^2}{2} - k_{24} Q Q_2 + \frac{8k_{24} - 4k_{24}^2 + 2Q^2 + w}{8} Q_2^2 + \frac{Q(k_{24} - 1)}{2} Q_2^3 + \frac{24 - 48k_{24} + 24k_{24}^2 - 5Q^2 - 2w}{96} Q_2^4, \quad (4.19)$$

$$F_z^{(RZT)} = \frac{(Q - Q_2)^2}{2} - k_{24} Q Q_2 + \frac{4k_{24} - 2k_{24}^2 + Q^2 + 2w}{4} Q_2^2 + \frac{Q(k_{24} - 1)}{2} Q_2^3 + \frac{24 - 48k_{24} + 24k_{24}^2 - 5Q^2 - 12w}{96} Q_2^4, \quad (4.20)$$

$$F_{\varphi}^{(RZT)} = \frac{w}{2} + \frac{(Q-Q_2)^2}{2} - k_{24}QQ_2 + \frac{8k_{24} - 4k_{24}^2 + 3w}{8}Q_2^2 + \frac{Q(k_{24}-1)}{2}Q_2^3 + \frac{24 - 48k_{24} + 24k_{24}^2 - 10w}{96}Q_2^4. \tag{4.21}$$

Here $F_h^{(RZT)}$, $F_z^{(RZT)}$, and $F_{\varphi}^{(RZT)}$ denote $F^{(RZT)}$ for homeotropic, zenithal, and azimuthal anchoring, respectively. We obtained a Landau-type form of $F^{(RZT)} = F_0^{(RZT)} + \alpha_1 Q_2 + \alpha_2 Q_2^2 + \alpha_3 Q_2^3 + \alpha_4 Q_2^4$ where $Q_2$ and $\{\alpha_1, \alpha_2, \alpha_3, \alpha_4\}$ play the role of order parameter and Landau expansion coefficients, respectively.
For nonchiral LCs ($Q$=0), one obtains

$$F_h^{(RZT)} = \frac{w}{2} + \frac{8k_{24} - 4k_{24}^2 + w + 4}{8}Q_2^2 + \frac{24 - 48k_{24} + 24k_{24}^2 - 2w}{96}Q_2^4, \tag{4.22}$$

$$F_z^{(RZT)} = \frac{4k_{24} - 2k_{24}^2 + 2w + 4}{4}Q_2^2 + \frac{24 - 48k_{24} + 24k_{24}^2 - 12w}{96}Q_2^4, \tag{4.23}$$

$$F_{\varphi}^{(RZT)} = \frac{w}{2} + \frac{8k_{24} - 4k_{24}^2 + 3w + 4}{8}Q_2^2 + \frac{24 - 48k_{24} + 24k_{24}^2 - 10w}{96}Q_2^4. \tag{4.24}$$

The spatially homogeneous order becomes unstable with respect to the RZT class of solutions where the coefficients $\alpha_2$ that weight the $Q_2^2$ contribution in Eqs. (4.22), (4.23) & (4.24) change sign. From the condition $\alpha_2 = 0$ one could deduce a critical value $k_{24}$ above which the RZT structures become stable:

$$k_{24}^{(h)} = 1 + \sqrt{1 + \frac{w}{4}}, \tag{4.25}$$

$$k_{24}^{(z)} = 1 + \sqrt{1 + w}, \tag{4.26}$$

$$k_{24}^{(\varphi)} = 1 + \sqrt{1 + \frac{3w}{4}}. \tag{4.27}$$

Here $k_{24}^{(h)}, k_{24}^{(z)}$, and $k_{24}^{(\varphi)}$ determine the critical values of $k_{24}$ for homeotropic, zenithal, and azimuthal anchoring, respectively. Note that in the approximation of equal elastic constants the Ericksen's critical value of $K_{24}$ is given by $k_{24}^{(e)} = 2$. Therefore, in the absence of chirality $K_{24}$ could trigger double-twisted structures only for $w < 0$, which in our modeling is physically meaningful for the case given by Eq. (4.25).

Next, we focus on the RT structures using the ansatz of Eq.(4.7) & (4.8). In the limit $Q_{RT} \ll 1$ it follows

$$F_e^{(RT)} \sim \frac{Q^2}{2} + 2QQ_{RT} + (2 - k_{24})Q_{RT}^2 - \frac{QQ_{RT}^3}{3} + \frac{\left(k_{24} - \frac{5}{4}\right)}{3}Q_{RT}^4. \tag{4.28}$$

It is easy to estimate the equilibrium value of the chirality wave number $Q_{RT}$ of the RT structure if both $Q$ and $Q_{RT}$ are small. We expand Eq. (4.13) and Eqs. (4.14), (4.15) & (4.16) and free energy minimization yields

$$Q_{RT} = -Q/(2 + \gamma - k_{24}), \tag{4.29}$$

with $\gamma = 0$ for homeotropic anchoring, and $\gamma \pm w$ for tangential anchorings (positive sign for zenithal anchoring and negative sign for azimuthal anchoring). Note the Eq. (4.29) is valid only in the limit $|Q_{RT}| < 1$.
Thus, for nonchiral LCs it follows

$$F_h^{(RT)} \sim w + (2 - k_{24})Q_{RT}^2 + \frac{(k_{24} - \frac{5}{4})}{3} Q_{RT}^4, \tag{4.30}$$

$$F_z^{(RT)} \sim (2 - k_{24} + w)Q_{RT}^2 + \frac{(k_{24} - \frac{5}{4} - w)}{3} Q_{RT}^4, \tag{4.31}$$

$$F_\varphi^{(RT)} \sim w + (2 - k_{24} - W)Q_{RT}^2 + \frac{(k_{24} - \frac{5}{4} + w)}{3} Q_{RT}^4. \tag{4.32}$$

In this case, the critical conditions read

$$k_{24}^{(h)} = 2, \tag{4.33}$$

$$k_{24}^{(z)} = 2 + w, \tag{4.34}$$

$$k_{24}^{(\varphi)} = 2 - w. \tag{4.35}$$

Therefore, in achiral LCs, the saddle-splay elasticity may trigger the RT structure below $k_{24}^{(e)} = 2$ only for the case of azimuthal anchoring.

#### 4.1.1.3 Numerical analysis

We next explore the (meta) stability of double-twist structures in chiral LCs. Of particular interest is the determination of regimes in which the reversal of macroscopic chirality could be realized by varying a relevant parameter.

##### 4.1.1.3.1 RZT structure: Homeotropic anchoring

We focus first on RZT (class 1) structures and homeotropic anchoring. Of interest is the exploration of the impact of the saddle–splay constant $k_{24}$ and intrinsic chirality $Q$ for relatively weak anchoring, for which we set to $w = 1$. In Figure 4.2 we plot $Q_1$ and $Q_2$ equilibrium values on varying $Q$ between 0 and 1. For the case $Q = 0$ (achiral nematic) the RZT structures could be triggered only in the regime $k_{24} > k_{24}^{(e)} \equiv 2$. However, for chiral LCs, $k_{24}$ efficiently promotes the stability of RZT structures well below $k_{24}^{(e)}$. Furthermore, for $k_{24} = 0$, it holds that $Q_2 = 0$ and $Q_1 = Q$. This solution corresponds to the classic cholesteric structure. Graphs in Figure 4.2 also reveal that a value of $k_{24}$ can be extracted experimentally.

We investigate how the saddle–splay constant $k_{24}$ and intrinsic chirality $Q$ influence the double chirality of the system. We first consider a weak homeotropic anchoring and we fix the anchoring strength to $w = 1$. In Figure 4.2, we compare the graphs $Q_1(k_{24})$ (left figure) and $Q_2(k_{24})$ (right figure) in equilibrium for five different values of $Q$ from 0 to 1. Although the value $k_{24}$ has an upper limit 2 according to the present theory, we have extended its interval to the value 3 for more general consideration. The case $Q = 0$ (nonchiral nematic) is exceptional: the unphysical value $k_{24} > 2$ would be needed for the RZT structure to be stable, while even very small values of $k_{24}$ are sufficient to support RZT double twist for nonzero $Q$. On the other hand, when $k_{24} = 0$, it holds $Q_2 = 0$ and $Q_1 = Q$, i.e., there is a

single twist around the $z$-axis. Graphs in Figure 4.2 also indicate the possibility to estimate the value of $k_{24}$, although it is also masked with the value of the anchoring strength.

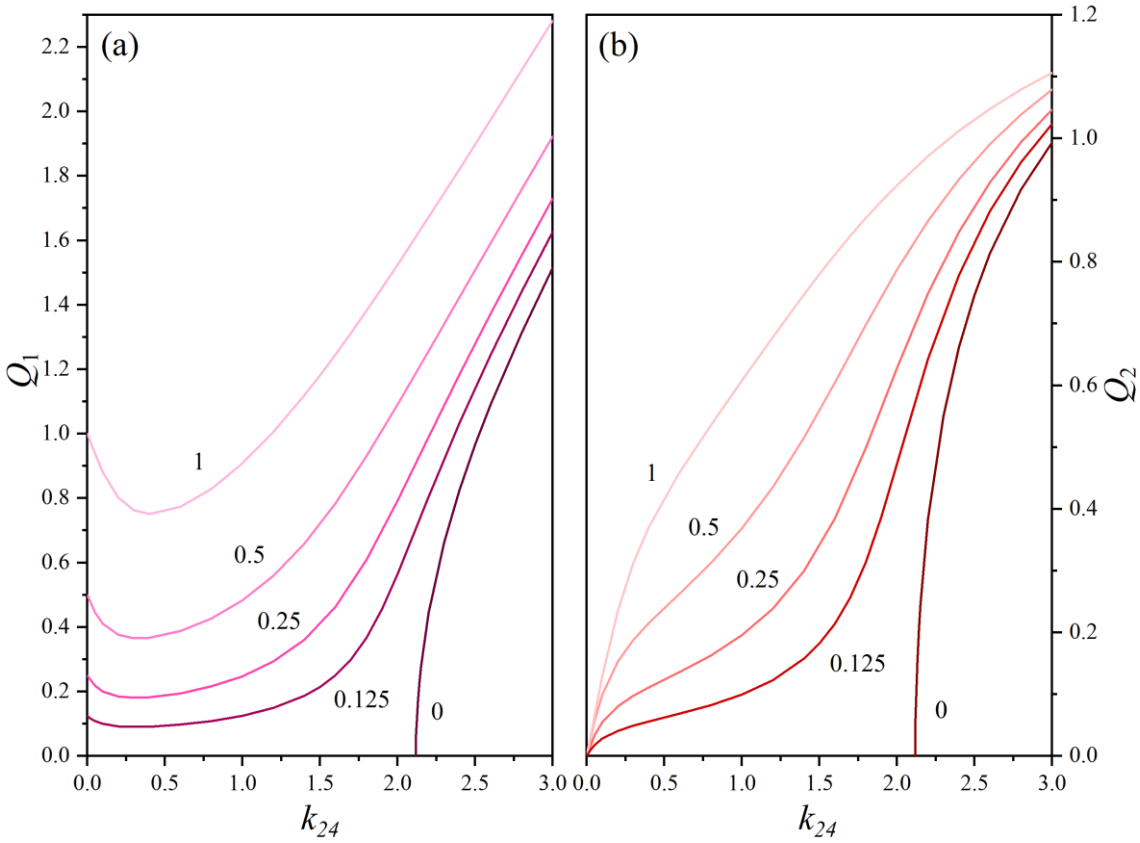


Figure 4.2: Dependence of equilibrium values of $Q_1$ (left) and $Q_2$ (right) on $k_{24}$ for five different values of the intrinsic chirality $Q$ (denoted by numbers in graphs). Homeotropic anchoring, $w = 1$ [144].

#### 4.1.1.3.2 RZT structure: Tangential anchoring

For tangential anchorings, the configurational variability of RZT structures is much more complex. This is illustrated in Figure 4.3, where we plot the dependencies of $Q_1(k_{24})$ and $Q_2(k_{24})$ on all studied anchoring, conditions for two significantly different values of $Q$, *viz.*, $Q = 0.125$ and $Q = 1$. The behavior is roughly similar for homeotropic and azimuthal anchoring, whereas for zenithal anchoring qualitatively different features emerge. In particular, $Q_1$ could even change sign at a critical value of $k_{24}$, which we denote by $k_{24}^{(c)}$. Similarly, for a given value of $k_{24}$, this crossover could be achieved by varying $Q$, and we label the corresponding critical value by $Q_c$.

The behavior of the system in the case of planar anchoring ($w = 1$) on varying $k_{24}$ and $Q$ is even more spectacular than for homeotropic anchoring. The graphs $Q_1(k_{24})$ and $Q_2(k_{24})$ for all types of anchoring and two significantly different values of $Q$ are compared: $Q = 0.125$ and 1. We notice that while the graphs for homeotropic and azimuthal anchoring are similar, the situation is significantly different for zenithal anchoring. The parameter $Q_1$ even changes sign at the definite value of $k_{24}$ in the latter case.

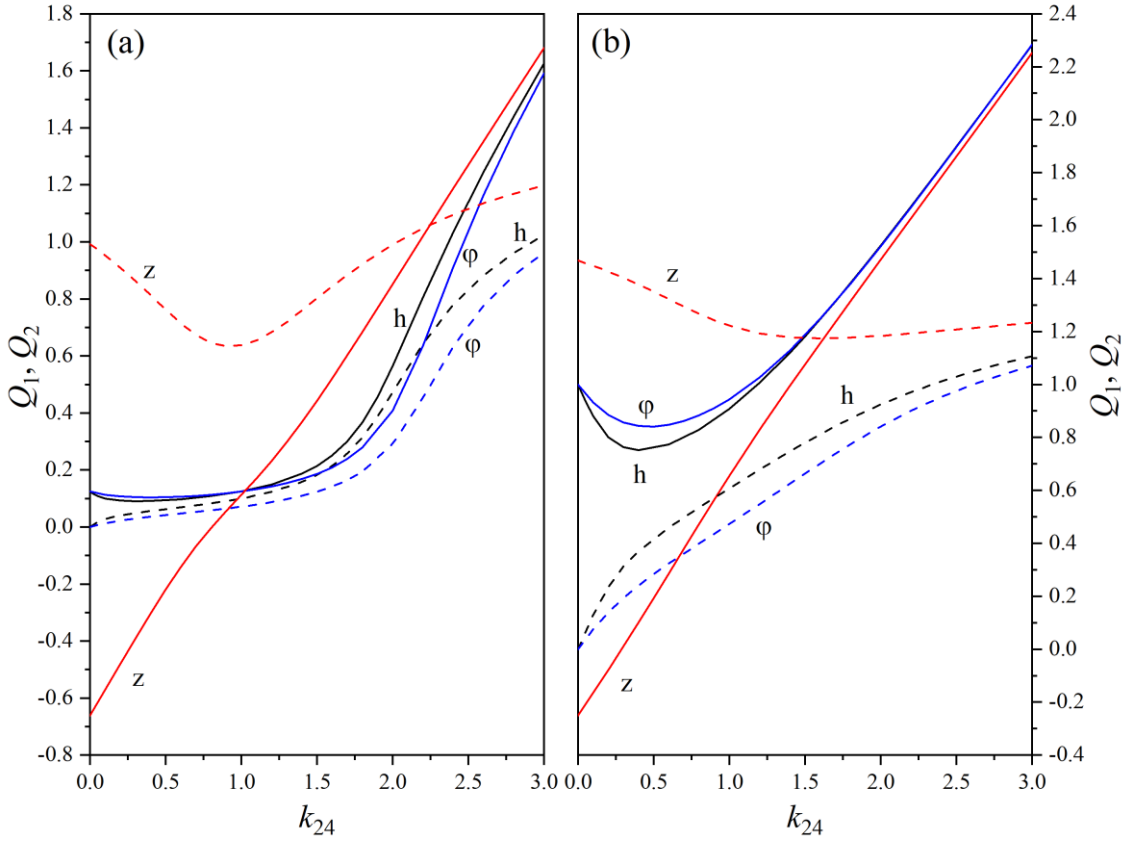


Figure 4.3: Dependence of $Q_1$ (solid lines) and $Q_2$ (dashed lines) on $k_{24}$ for $Q = 0.125$ (left figure) and $Q = 1$ (right figure) and different types of anchoring, labeled by "h" (homeotropic), "$\varphi$" (azimuthal) and "z" (zenithal). $w = 1$ [144].

Note that a value of $k_{24}^{(c)}$ depends relatively strongly on $Q$. Because the uniaxial twist with $Q_1 = 0$ can be observed easily by polarized optical microscopy, this phenomenon may be exploited to measure the splay–bend elastic constant. This is illustrated in Figure 4.4, where we plot the $Q_c(k_{24})$ dependence for different anchoring strengths. Experimentally, one could vary $Q$ by adding a chiral dopant to LC. The reversal of the sign of $Q_1$ exists in the interval $0 < k_{24} < 1$ well below $k_{24}^{(e)}$. In the strong anchoring limit $W \infty$ the graph $Q_c(k_{24})$ approaches the straight line.

We also note that in the case of zenithal anchoring, the value of $k_{24}$, where $Q_1$ changes sign, is very different for the two cases of $Q$. Since the uniaxial twist with $Q_1 = 0$ can be easily noticed with the optical polarizing microscopy, and this may serve as a way of measurement of splay–band elastic constant. Regarding the possible measurement of $k_{24}$, Figure 4.4 shows the dependence of the "critical" value of intrinsic chirality $Q_c$ on $k_{24}$, where $Q_1 = 0$. The suggested experiment is the following: chiral molecules are added to NLC to increase intrinsic chirality until $Q_1 = 0$. Then, according to Figure 4.3, the corresponding $k_{24}$ can be obtained. The reversal of the sign of $Q_1$ exists only in the interval of the saddle-splay constant $0 < k_{24} < 1$. We have considered five different of $w$: from $w = 0.2$ to 5. In the case $w > 1$, the graphs are similar. In the strong anchoring limit $w \rightarrow \infty$, the graph $Q_c(k_{24})$ approaches the straight line. For $w < 1$, the graphs are qualitatively different, and the interval of $k_{24}$ is smaller. Another significant difference is about the corresponding value of $Q_2$: while $Q_2$ remains finite at the right limit of interval of $k_{24}$ in the case $w > 1$ (i.e., $Q_2 > 0$ at $k_{24} = 1$), $Q_2$ goes to zero at the right limit ($k_{24} < 1$) in the case $w < 1$).

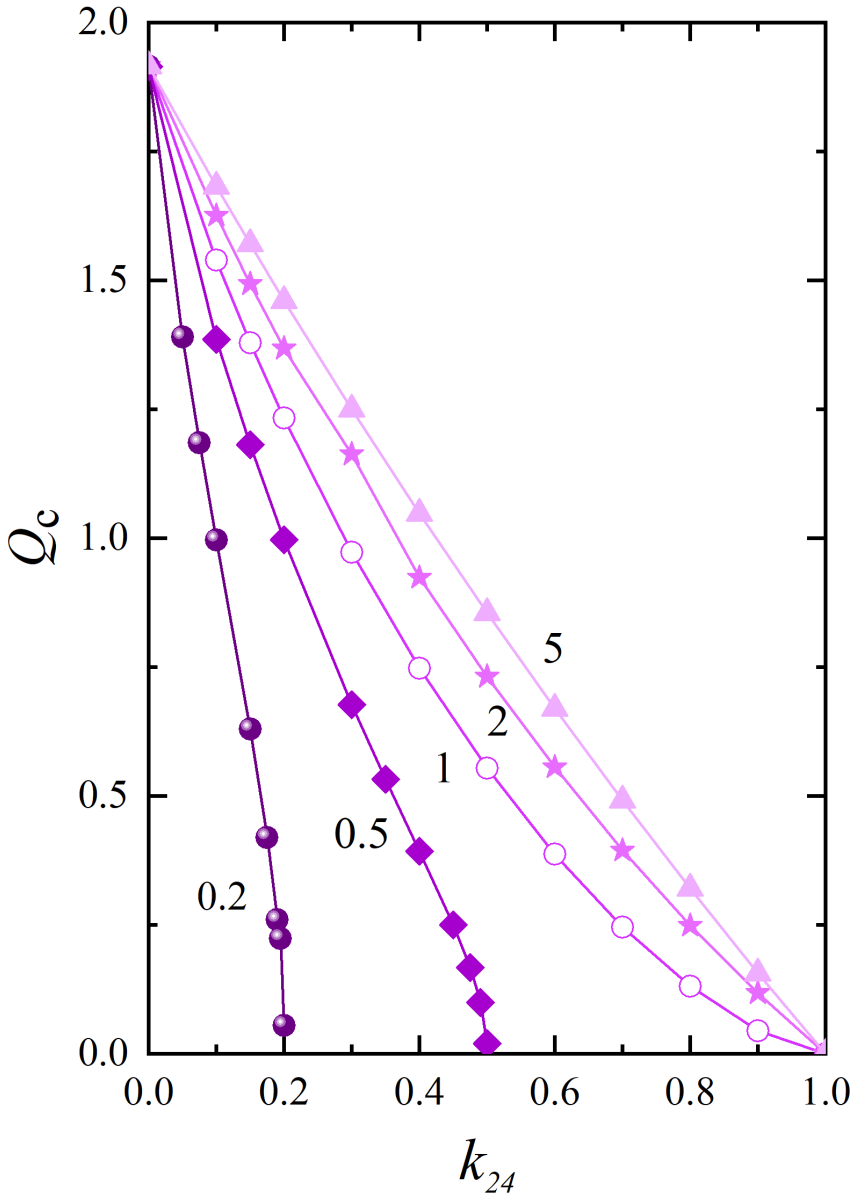


Figure 4.4: The dependence of the critical intrinsic chirality $Q_c$ (where $Q_1 = 0$) on $k_{24}$ in the case of zenithal anchoring for different values of anchoring strength. Results were calculated in points labeled with symbols and lines that serve as guides for the eye. From left to right: $w = 0.2$ (circles), 0.5 (diamonds), 1 (open circles), 2 (stars) and 5 (triangles) [144].

#### 4.1.1.3.3 Energy comparison of RZT and RT structures

The equilibrium energies of both types of structures (RZT and RT) were compared for different sets of parameters. In general, homeotropic anchoring favors RZT configurations. This is obvious since the nematic director of the RT structure is always parallel to the boundary plane at the cylinder boundary. On the other hand, for both types of tangential anchoring stability regimes of different structures depending on a specific set of parameters $k_{24}$, $Q$ and $w$. Due to broad parameter space, we limit our analysis to a few cases relevant

to our study. For example, Figure 4.4 reveals the parameters for which $Q_1 = 0$ (chirality reversal) is realised for the RZT configuration for zenithal anchoring. It is essential to compare its free energy with the competitive RT structure. Some representative examples are depicted in Figure 4.5 and Figure 4.6. In Figure 4.5, we plot the equilibrium energies of the competing structures on varying $Q$ for $k_{24} = 0.5$ and weak ($w = 1$) zenithal anchoring for the case exhibiting chirality reversal. In this case, the RZT structure with $Q_1 < 0$ is metastable with respect to RT. However, Figure 4.5 illustrates the existence of a regime for which the configuration with $Q_1 < 0$ is stable for $k_{24} = 0.25$. Thus, chirality reversal may be found experimentally in this case. The arrows in Figure 4.5 indicate approximately the energy of the RZT structure at the reversal of the sign of $Q_1$, together with the calculated chirality parameters. For lower values of $Q$, it holds that $Q_1 < 0$, and vice versa. Although the energies for the cases $k_{24} = 0.25$ and 0.5 are not very different, the critical value of $Q$ ($Q_c = Q$, where $Q_1$ changes sign) differs significantly: $Q_c = 0.554$ for the case $k_{24} = 0.5$, whereas $Q_c = 1.097$ for the case $k_{24} = 0.25$.

It is easy to estimate the equilibrium value of the chirality $Q_{RT}$ of the RT structure if both $Q$ and $Q_{RT}$ are supposed to be small. In this case $\sin(Q_{RT}) \approx Q_{RT}$ in Eqs. (4.22), (4.23), (4.24), (4.25), (4.26) & (4.27), and upon consequent minimization of the energy, we obtain: $Q_{RT} = -Q/(2 + \Delta - k_{24})$, with $\Delta = 0$ for homeotropic anchoring, and $\Delta = \pm\, w$ for planar anchoring (positive sign for zenithal anchoring and negative sign for azimuthal anchoring). Of course, the denominator $(2 + \Delta - k_{24})$ must not be near zero value for this estimation to hold. The easiest case for physical interpretation of this estimation is, when $k_{24} = 0$ and $w = 0$: it then holds $Q_{RT} = -\frac{Q}{2}$. The negative sign is correct and it indicates an appropriate twist of nematic direction around the radial axis in dependence of the sign of $Q$. The absolute value of $Q_{RT}$ is half the value of $Q$ because of the double twist.

The equilibrium energies of both types of structures (RZT and RT) were compared for different sets of parameters. Still, we have not made a systematic comparison to obtain a corresponding stability phase diagram since there are too many free parameters to vary. We have noticed, for instance, that the homeotropic anchoring tends to favor the RZT structure. This is obvious since the nematic director of the RT structure is always parallel to the boundary plane at the cylinder boundary. On the other hand, for both types of planar anchoring, there is a competition of the energy of both structures, and one or the other structure is stable depending on a specific set of parameters $k_{24}$, $Q$ and $w$.

Since Figure 4.4 indicates sets of parameters where $Q_1 = 0$ (chirality reversal), it is essential to compare the corresponding energies with the RT structure. We have only picked up some typical sets of parameters without systematic variation. We have found that in some relatively narrow intervals of parameters, there indeed exists the energetically favorable structure (also with respect to RT), where we can observe the change of the sign of $Q_1$. For other values of the parameters, the lower energy of the RT structure obscures this chirality reversal. This is depicted in Figure 4.4 and Figure 4.5.

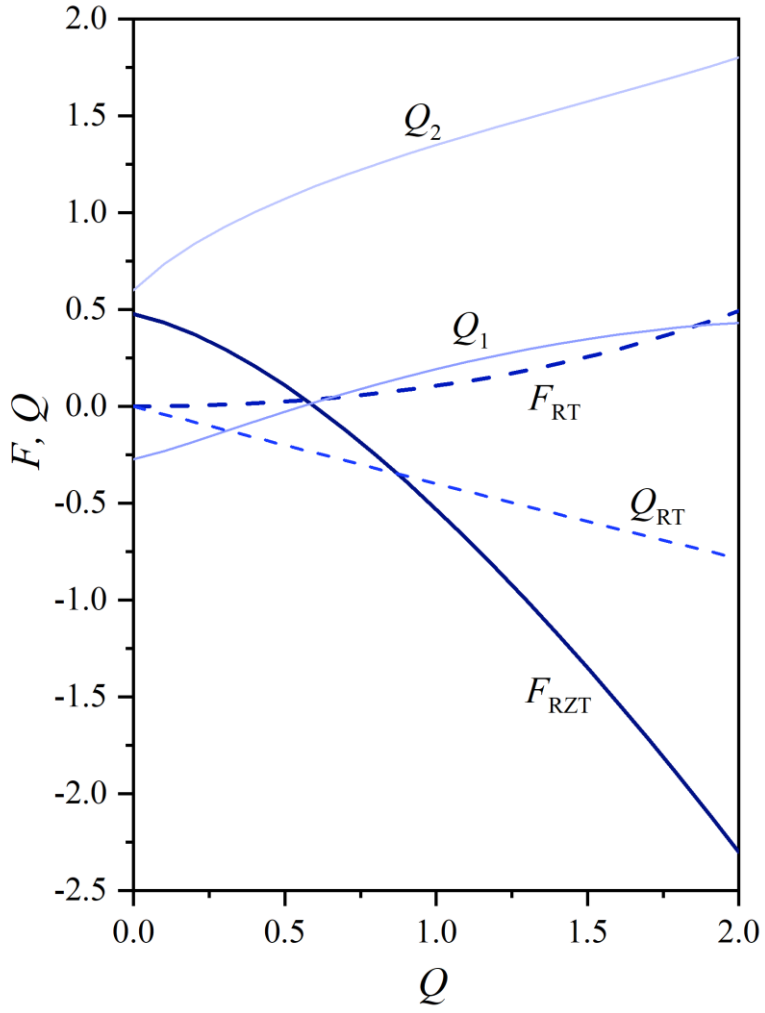


Figure 4.5: Dependence of the equilibrium energies (thick lines) and chirality parameters (thin lines) of the RZT structure (solid lines) and RT structure (dashed lines) on the intrinsic chirality $Q$. $k_{24} = 0.5$, zenithal anchoring with $w = 1$ [144].

In Figure 4.4 we present equilibrium energies and chirality parameters for both structures when intrinsic chirality $Q$ varies from 0 to 2, with $k_{24} = 0.5$ and $w = 1$ for zenithal anchoring. The chirality $Q_1$ reverses sign. But the comparison of energies shows that the RZT structure with $Q_1 < 0$ is not stable with respect to RT. However, as it is seen in Figure 4.5, where only the energies are compared, a range of the values of the parameter $Q$ exists where $Q_1 < 0$ is stable, if we change the value of $k_{24}$ to 0.25. Thus, the chirality reversal could be found experimentally in this case. The arrows in Figure 4.5 indicate approximately the energy of the RZT structure at the reversal of the sign of $Q_1$, together with the calculated chirality parameters. For lower values of $Q$ it holds $Q_1 < 0$, and vice versa. Although the energies in the cases $k_{24} = 0.25$ and 0.5 are not very different, the critical value of $Q$ ($Q_c = Q$, where $Q_1$ changes sign) differs significantly: $Q_c = 0.554$ in the case $k_{24} = 0.5$, while $Q_c = 1.097$ in the case $k_{24} = 0.25$.

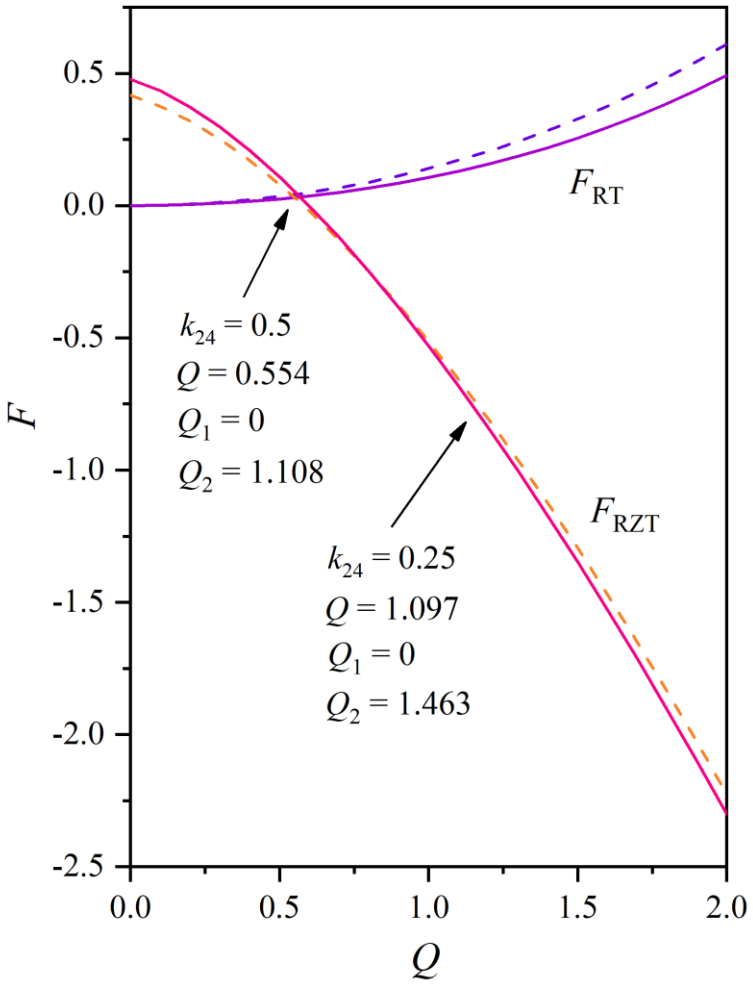


Figure 4.6: Dependence of the equilibrium energies of the RZT and RT structures on the intrinsic chirality $Q$. Solid lines: $k_{24} = 0.5$. Dashed lines: $k_{24} = 0.25$. Zenithal anchoring with $w = 1$. Arrows indicate the sign reversal of $Q_1$ for both values of $k_{24}$. For the case $k_{24} = 0.25$, the chirality $Q_1$ reverses sign in the regime where $F_{RZT} < F_{RT}$ [144].

Finally, in Figure 4.7 and Figure 4.8 we show calculated optical polarizing microscopy patterns for the competing RZT and RT structures for two different polarization directions of polarizer and analyzer, where we set $Q_1 = Q_2 = Q_{RT} = 1$. Simulations details are described in [143], [145]. The polarizations of polarizer and analyzer are mutually perpendicular. The angle between the polarizer and $x$–axis (horizontal axis) is 0 or 45°. One sees that the textures are significantly different and that one could easily distinguish these structures by using polarizing optical microscopy.

We may conclude for the case of zenithal anchoring that we can have a rich variability of qualitatively different structures, depending on a specific set of material parameters (and geometry, i.e., the radius of the cylinder): RZT with negative $Q_1$, RZT with positive $Q_1$, YZ ($Q_1 = 0$; twist only in the $y$-direction), and RT structure. Here, we consider only the case of RTZ with positive $Q_2$. On the other hand, in the case of homeotropic or azimuthal anchoring, we can have RZT states with finite values of chirality $Q_1$ and very small values of chirality $Q_2$, i.e., practically ZT structure (twist only in $z$-direction, i.e., the usual helical structure along the cylindrical axis). Figure 4.6 also indicates the importance of the $k_{24}$

parameter: a relatively small change from 0.25 to 0.5 significantly alters the stability of compared structures. We may note that the actual multi-parametric phase diagram of the stability of different structures, including the variation of parameters $w, k_{24}, Q$ and the anchoring easy axis, is expected to show a complicated pattern.

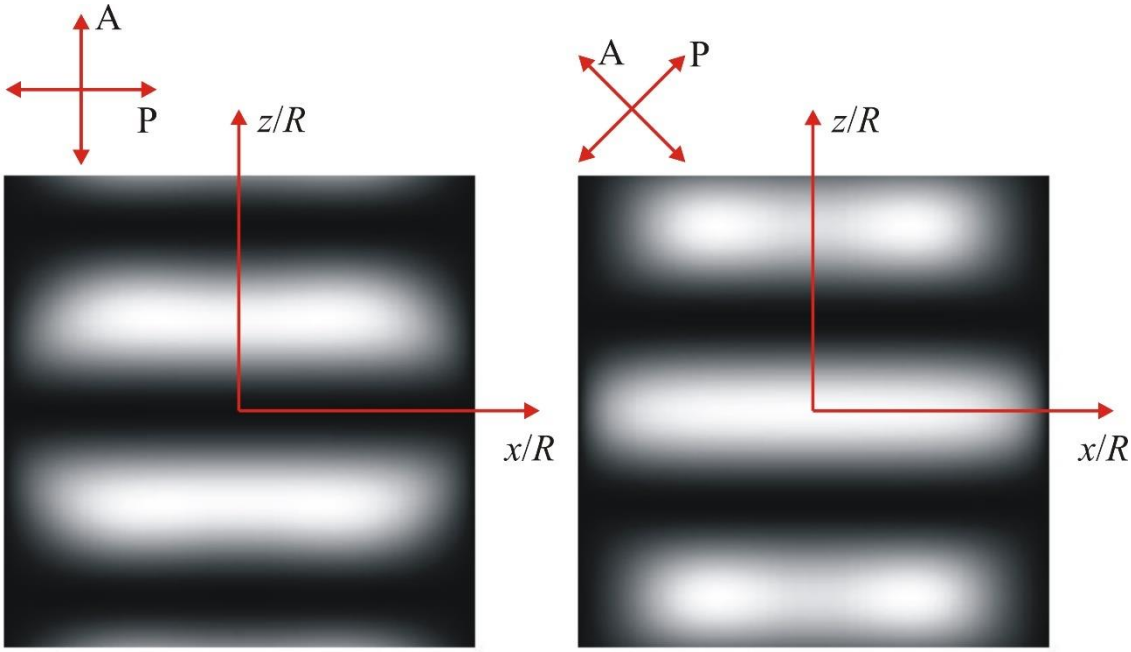


Figure 4.7: Calculated optical patterns for the RZT structure with $Q_1 = Q_2 = 1$. The transmitted polarization of polarizer is in the $x$–direction (left figure) and at the angle 45° with respect to $x$–direction (right figure). Optical data: $R = 1$ μm, laser light wavelength $\lambda = 445$ nm, refraction indices: $n_0 = 1.544$, $n_e = 1.821$, corresponding to NLC E7 [144].

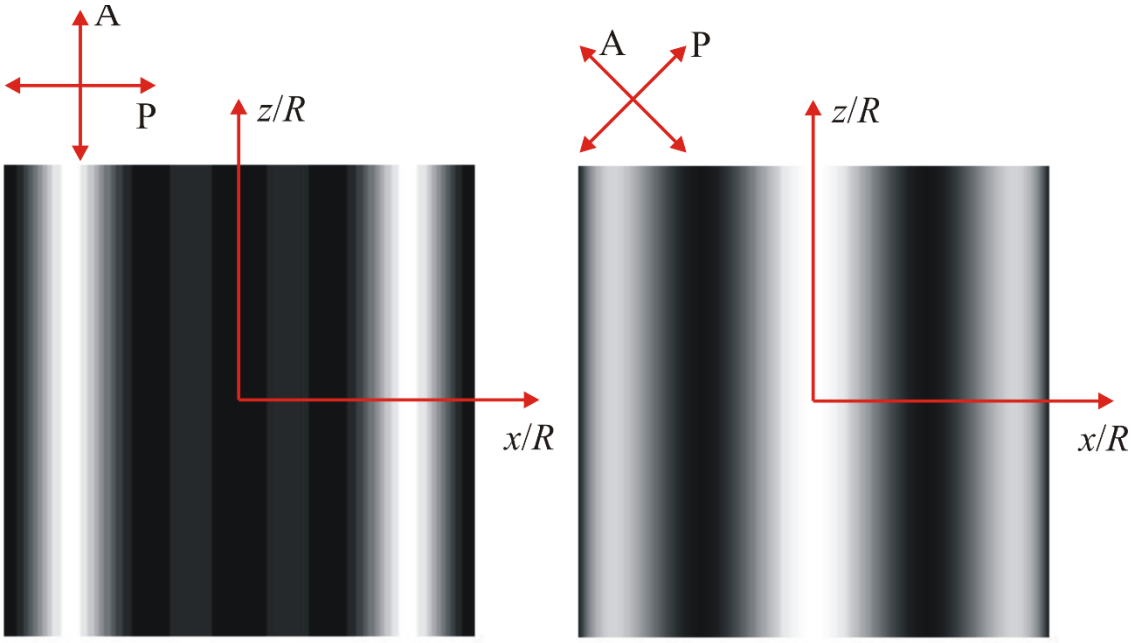


Figure 4.8: The same as for Figure 4.7, but for the RT structure with $Q_{RT} = 1$ [144].

Finally, in Figure 4.6 and Figure 4.7 we compare optical polarizing microscopy patterns for both structures and two different polarization directions of polarizer and analyzer. We

choose the representative values of chirality parameters: $Q_1 = Q_2 = Q_{RT} = 1$. The polarizations of polarizer and analyzer are at the angle of 90°, as usual. The angle between the polarizer and $x$–axis (horizontal axis) is 0 or 45°. The details of numerical simulation of optical patterns are given in Refs. [146], [147]. An optical polarizing microscopy is an appropriate tool for distinguishing between the considered structures.

It is also instructive to use the Kilian twist tensor $K_{KIL}$ according to Ref. [148] in order to obtain additional insight into the local character of twist elastic deformation:

$$K_{KIL} = \begin{bmatrix} n_y \frac{\partial n_z}{\partial x} - n_z \frac{\partial n_y}{\partial x} & n_y \frac{\partial n_z}{\partial y} - n_z \frac{\partial n_y}{\partial y} & n_y \frac{\partial n_z}{\partial z} - n_z \frac{\partial n_y}{\partial z} \\ n_z \frac{\partial n_x}{\partial x} - n_x \frac{\partial n_z}{\partial x} & n_z \frac{\partial n_x}{\partial y} - n_x \frac{\partial n_z}{\partial y} & n_z \frac{\partial n_x}{\partial z} - n_x \frac{\partial n_z}{\partial z} \\ n_x \frac{\partial n_y}{\partial x} - n_y \frac{\partial n_x}{\partial x} & n_x \frac{\partial n_y}{\partial y} - n_y \frac{\partial n_x}{\partial y} & n_x \frac{\partial n_y}{\partial z} - n_y \frac{\partial n_x}{\partial z} \end{bmatrix}.$$

This tensor is expressed with Cartesian components of nematic director and with their spatial derivatives. In general, the tensor has no specific symmetry. It has at most two nonzero eigenvalues representing the local "effective chiralities" in two different directions. These two directions (if they exist) are given by the corresponding eigenvectors which are always perpendicular to the local nematic director. Conversion of the nematic director into the Cartesian form and the calculation of the tensor $K$ results of the following two eigenvalues: $\lambda_1 = q_1^{(RZT)} \cos^2(q_2^{(RZT)}\, r \sin\varphi)$ and $\lambda_2 = q_2^{(RZT)}$. The corresponding eigenvectors are perpendicular to the nematic director, but they are generally not perpendicular. While the second effective chirality is $q_1^{(RZT)}$ everywhere, $\lambda_1$is inhomogeneous. Since the absolute value of sin $\varphi$ varies from 0 to 1 within the cylinder, the maximum value of $\lambda_1$is simply $q_1^{(RZT)}$ for positive $q_1^{(RZT)}$. However, the minimum value of $\lambda_1$ depends on the dimensionless chirality parameter $Q_2$. If $Q_2$ is smaller than $\pi/2$, so it is the product $q_2^{(RZT)}\, r$ within the cylinder since $r < R$. In this case, the minimum value of $\lambda_1$ is larger than zero, and this value is $\cos^2 Q_2$. However, if $Q_2 > \frac{\pi}{2}$ holds, the minimum value of $\lambda_1$ is zero.

The expression for the eigenvector corresponding to $\lambda_1$ is complicated, but in the case $r = 0$ it simplifies to the vector in the direction of $z$–axis, as expected. The expression for the second normalized eigenvector is simple: $\vec{e}_2 = (-\sin\left(q_1^{(RZT)} z\right), \cos\left(q_1^{(RZT)} z\right), 0)$. It is easily seen that it is perpendicular to the nematic director.

We may relate the chiralities $q_1^{(RZT)}$ and $q_1^{(RZT)}$ (or their dimensionless forms $Q_1$ and $Q_2$) and correspondingly the Kilian tensor to the saddle–splay elastic energy term in the dimensionless form:

$$F_{24}^{(RZT)} = -\frac{k_{24}}{2} Q_1 Q_2 \left(1 + \frac{J_1(2Q_2)}{Q_2}\right). \tag{4.36}$$

In the limit of small $Q_2$ this expression is simplified to $F_{24} \approx -k_{24} Q_1 Q_2$, while for very large $Q_2$, we have $F_{24} \approx -k_{24} Q_1 Q_2/2$. Therefore, the saddle–splay elastic term would tend to increase the positive values of both $Q_1$ and $Q_2$ without limits (despite local maxima and minima of the Bessel function) if no other energy terms were present. Consequently, the saddle–splay elastic term tends to increase the averaged eigenvalue $\lambda_1$ over the cylinder and the homogeneous eigenvalue $\lambda_2$ of the Killian tensor.

In the case of RT structure, the two eigenvalues of $K$ are $\lambda_1 = -q_{RT}$ and $\lambda_2 = -\sin(2q_{RT}\, r)/(2r)$. Thus, for small radius $r$, $\lambda_2 \approx \lambda_1$ holds, as expected. The corresponding eigenvectors are $\vec{e}_1 = \vec{e}_r$ and $\vec{e}_2 = (\sin\varphi \cos(q_{RT} r), -\cos\varphi \cos(q_{RT}\, r), \sin(q_{RT}\, r))$. Both

vectors are perpendicular to the nematic director and each other. It is interesting to note, that in contrast to the ZRT structure, the saddle–splay elastic term in the RT structure tends to favor the finite value of chirality parameter, $Q_{RT} = \pi/2$, since this term equals to

$$F_{24}^{(RT)} = -k_{24} \sin^2 Q_{RT}. \tag{4.37}$$

## 4.2 Elastic Force on Immersed Nanoparticle

Results above indicate under what conditions multiple-twisted structures are formed in cylindrical geometry. However, if one relaxes the cylindrical confinement, such structures inevitably lead to lattices of disclinations due to topological reasons [15], [74]. Recent studies also demonstrate [14], [149]–[153] that topological defects represent efficient traps for appropriate NPs.

Hereinafter, we make a simple analysis that illustrates how NP surface decoration impacts the positioning of the NP in an inhomogeneous nematic structure.

As cylindrical NPs, we consider a system of cylindrical polar coordinates $\{\vec{e}_r, \vec{e}_\varphi, \vec{e}_z\}$ where $e_r$ is a radial unit vector, orthogonal to $\vec{e}_z$ emanating from the symmetry axis, while $\vec{e}_\varphi = \vec{e}_z \times \vec{e}_r$ completes the positive orthogonal tried. Symmetry suggests to take order tensor $Q$ in this class can be expressed as

$$\begin{aligned} Q(r,z) = -2q_0\vec{e}_\varphi \otimes \vec{e}_\varphi + (q_0+\delta)\vec{e}_r \otimes \vec{e}_r + (q_0-\delta)\vec{e}_z \otimes \vec{e}_z \\ +q_m(\vec{e}_r \otimes \vec{e}_z + \vec{e}_z \otimes \vec{e}_r), \end{aligned} \tag{4.38}$$

where $q_0, q_m$, and $\delta$ depends only on $r$ and $z$. In this representation, $q_m$ measures departure of the eigenframe of $Q$ from the local coordinate basis $\{\vec{e}_r, \vec{e}_\varphi, \vec{e}_z\}$ while $\delta$ measures phase biaxiality when $q_m = 0$. The eigenvalues of $Q$ are easily computed from Eq. (4.38) and are given by

$$\lambda_0 = -2q_0, \lambda_\pm = q_0 \pm \sqrt{q_m^2 + \delta^2}. \tag{4.39}$$

Three basic loci formed by uniaxial states are then singled out in the $(q_0, \delta, q_m)$ space from Eq. (4.39): the $q_0$ axis configuration characterized by

$$\delta = q_m = 0, \tag{4.40}$$

describes uniaxial states along $\vec{e}_\varphi$, with positive scalar order parameter if and only if $q_0 < 0$; The condition

$$9q_0^2 = q_m^2 + \delta^2 \tag{4.41}$$

describes uniaxial states with $\lambda_0 = \lambda_+$, when $q_0$ negative, and with $\lambda_0 = \lambda_-$, when $q_0$ is positive. In the former case, the scalar order parameter is negative, while it is positive in the latter. At the cone's vertex, three eigenvalues coalesce, and an isotropic state occurs. We finally note that since the eigenvalues of the order tensor $Q$ are bounded in the range $\left[-\frac{1}{3}, \frac{2}{3}\right]$, just a bounded portion of the $(q_0, \delta, q_m)$-space is admissible.

For simplicity, we confine ourselves to the one-constant approximation, and so we consider an elastic free-energy density $f_e = \frac{L}{2}|\nabla Q|^2$ where $L > 0$ is the elastic constant (see Eq. (4.39)). To account for the existence of stable ordered states, the internal potential (see Eq. (4.25))

$$f_h(Q) = \frac{a(T-T^*)}{2} trQ^2 - \frac{B}{3} trQ^3 + \frac{C}{4}(trQ^2)^2 \tag{4.42}$$

should be added. Besides these bulk terms, we suppose that the NPs surface $(\partial\mathcal{B})$ favors, rather than imposes, a surface alignment described by the order tensor $Q_s$. We then introduce the following surface free-energy density (see Eq. (2.10))

$$f_s(Q, Q_s) = \frac{w}{2}|Q - Q_s|^2, \tag{4.43}$$

where $w > 0$. Three different cases are considered, we suppose that the preferential alignment $Q_s$ is radial and uniaxial and so we assume

$$Q_s = s_b\left(\vec{e}_r \otimes \vec{e}_r - \frac{1}{3} I_{(d)}\right), \tag{4.44}$$

where $s_b$ is the equilibrium bulk value of the scalar order parameter $s$.

Strong tangential anchoring in the second case we impose

$$Q_s = s_b\left(\vec{e}_z \otimes \vec{e}_z - \frac{1}{3} I_{(d)}\right). \tag{4.45}$$

The nematic blob also possesses a free surface $\partial\mathcal{B}_\infty$ that, for the sake of consistency, we take as a surface of revolution about the symmetry axis $\vec{e}_z$. We will not determine its shape, but we shall replace it with a circular cylinder of radius $R_\infty$, so large that the order tensor has already relaxed to its asymptotic profile on it. Since no confinement is placed on $\partial\mathcal{B}_\infty, w|_{\partial\mathcal{B}_\infty} = 0$. Thus, we need to minimize the free energy functional

$$F[Q] = \int_{\mathcal{B}} [f_e(Q) + f_h(Q)]dV + \int_{\partial\mathcal{B}} f_s(Q, Q_s)dA. \tag{4.46}$$

on the set of symmetric, traceless tensors $Q$ represented by Eq. (4.38).

### 4.2.1 Equilibrium equations

Follow a standard procedure, we find the equilibrium configurations by setting the first variation $\delta F$ of $F$ equal to zero. For a given position of the NP, we need to minimize the total free energy $F$ of the system. To this aim, we introduce polar cylindric coordinates into Eq. (4.46) and we map $Q$ into a perturbed tensor $Q_\varepsilon$ by mapping $q_0, \delta$ and $q_m$ in Eq. (4.38) into

$$q_0^\varepsilon = q_0 + \varepsilon u, \tag{4.47}$$

$$\delta_0^\varepsilon = \delta_0 + \varepsilon h, \tag{4.48}$$

$$q_m^\varepsilon = q_m + \varepsilon v, \tag{4.49}$$

where $u, h$ and $v$ are three regular, arbitrary functions of $r$ and $z$. We then expand $F[Q_\varepsilon]$ as a power series of $\varepsilon$ and focus on the first-order terms which only contribute to the first variation of $F$ defined as

$$\delta F(Q)[u,h,v] = \left.\frac{dF[Q_\varepsilon]}{d\varepsilon}\right|_{\varepsilon=0}. \tag{4.50}$$

In terms of our parametrization, we obtain the following relations:

$$trQ^2 = 2(q_m^2 + \delta^2 + 3q_0^2), \tag{4.51}$$

$$trQ^3 = 6q_0(\delta^2 + q_m^2 - q_0^2). \tag{4.52}$$

and

$$|\nabla Q|^2 = 2\left\{[3|\nabla q_0|^2 + |\nabla\delta|^2 + |\nabla q_m|^2] + \frac{1}{r^2}[q_m^2 + (3q_0+\delta)^2]\right\}. \tag{4.53}$$

The first variation $\delta F$ of $F$ yields

$$\begin{aligned}
\frac{1}{2\pi}\delta F[u,h,v] = &\int_{\mathcal{B}} r\left\{2L\begin{bmatrix}\frac{1}{r^2}(3(3q_0+\delta)u + (3q_0+\delta)h + q_m v)\\ -(3u\Delta q_0 + h\Delta\delta + v\Delta q_m)\end{bmatrix}\right\}drdz\\
&+\int_{\mathcal{B}} r\begin{Bmatrix}2A[3q_0u + \delta h + q_m v] -\\ 2B[2(\delta h + q_m v - q_0 u) + u(q_m^2 + \delta^2 - q_0^2)]\\ +4C(q_m^2 + \delta^2 + 3q_0^2)[3q_0u + \delta h + q_m v\,]\end{Bmatrix}drdz\\
&+\int_{\partial\mathcal{B}} 2Lr\left[3uq_{0,z} + h\delta_{,z} + v\nabla q_{m,z}\right]dr\\
+w&\int_{\partial\mathcal{B}} r\left\{\begin{matrix}[4q_0u + (q_0+\delta)(u+h) + (q_0-\delta)(u-h) + 2q_m v]\\ -s_b(u+h)\end{matrix}\right\}dr\\
&+2\pi\int_{\partial\mathcal{B}\infty} 2L[3u\nabla q_0 + h\nabla\delta + v\nabla q_m]\cdot v dA,
\end{aligned} \tag{4.54}$$

where $v$ is the outer normal of the free surface $\partial\mathcal{B}_\infty$ and where we noted that prescribing the tensor on $\partial\mathcal{B}$ makes the functions $u, h$, and $v$ vanish there. The factor $1/2\pi$ in front of $\delta F$ is due to the integration in the polar angle $\varphi$. Finally, $\Delta$ is the Laplace operator that acts on a scalar function $f = f(r,z)$ as

$$\Delta f = \frac{\partial^2 f}{\partial r^2} + \frac{1}{r}\frac{\partial f}{\partial r} + \frac{\partial^2 f}{\partial z^2}. \tag{4.55}$$

The integral on $\partial\mathcal{B}_\infty$ in Eq. (4.54) prescribes that the free surface of the nematic blob squeezed between the plates satisfies $\nabla Q \cdot v = 0$. However, we replace $\partial\mathcal{B}_\infty$ with a circular cylinder of radius $R_\infty \gg d$, and we impose the free-boundary condition from it, that is:

$$q_{0,r}(R_\infty, z) = \delta_{,r}(R_\infty, z) = q_{m,r}(R_\infty, z) = 0, \tag{4.56}$$

where we noted that $v = \vec{e}_r$ on $r = R_\infty$ and that the regular fields $u, h$ and $v$ can be chosen arbitrarily. Since these latter requirements also hold in bulk, we arrive at the following equilibrium equations valid in $\mathcal{B}$

$$L\left[\Delta q_0 - \frac{1}{r^2}(3q_0+\delta)\right] - Aq_0 + \frac{B}{3}(\delta^2 + q_m^2 - 3q_0^2) \\ -2Cq_0(3q_0^2 + \delta^2 + q_m^2) = 0, \tag{4.57}$$

$$L\left[\Delta\delta - \frac{1}{r^2}(3q_0+\delta)\right] - A\delta + 2B\delta q_0 - 2\delta C(\delta^2 + q_m^2 + 3q_0^2) = 0, \tag{4.58}$$

$$L\left[\Delta q_m - \frac{q_m}{r^2}\right] - 2Aq_m + 2Bq_0q_m - 2C(\delta^2 + q_m^2 + 3q_0^2)q_m = 0. \tag{4.59}$$

The following boundary conditions are imposed on boundaries $\partial\mathcal{B}$:

$$Lq_{0,z} + wq_0 = \frac{s_b}{6}w, \tag{4.60}$$

$$L\delta_{,z} + w\delta_0 = \frac{s_b}{2}w, \tag{4.61}$$

$$Lq_{m,z} + wq_m = 0. \tag{4.62}$$

Before solving numerically, the set of Eqs. (4.57),(4.58), (4.59) and (4.60), (4.61), (4.62), we recast them into a non-dimensional form, using the same units as in Ref. [154].

For later convenience, we also introduce the quantities

$$t(\tau) = \sqrt{1-\tau} + 1. \tag{4.63}$$

and the biaxial coherence length

$$\xi_b = \left[\frac{4LC}{B^2 t(\tau)}\right]^{1/2}, \tag{4.64}$$

with $t(\tau)$ given by Eq. (4.63). We note explicitly that $\xi_b$ depends on temperature through $\tau$. If we introduce

$$\bar{Q} = \frac{1}{s^*}Q, \qquad \bar{r} = \frac{r}{b}, \qquad \bar{z} = \frac{z}{d}$$

and replace $L$ with $\xi_b$, by direct manipulations, we can give Eq. (4.57), (4.58), (4.59) the following form

$$\left(\frac{\xi_b}{d}\right)^2 t(\tau)\left[\Delta q_0 - \frac{1}{r^2}(3q_0+\delta)\right] - \frac{\tau}{6}q_0 + \frac{1}{3}(\delta^2 + q_m^2 - 3q_0^2) \\ -\frac{q_0}{2}(3q_0^2 + \delta^2 + q_m^2) = 0, \tag{4.65}$$

$$\left(\frac{\xi_b}{d}\right)^2 t(\tau)\left[\Delta\delta - \frac{1}{r^2}(3q_0+\delta)\right] - \frac{\tau}{6}\delta + 2\delta q_0 - \frac{\delta}{2}(\delta^2 + q_m^2 + 3q_0^2) = 0, \tag{4.66}$$

$$\left(\frac{\xi_b}{d}\right)^2 t(\tau)\left[\Delta q_m - \frac{q_m}{r^2}\right] - \frac{\tau}{6}q_m + 2q_0 q_m - \frac{1}{2}(\delta^2 + q_m^2 + 3q_0^2)q_m = 0, \tag{4.67}$$

where we omitted bars to simplify notation. Similarly, the boundary conditions (Eq. (4.60), (4.61), (4.62)) are expressed as

$$\left(\frac{\xi_w}{d}\right) q_{0,z} + q_0 = \frac{1}{6}t(\tau), \tag{4.68}$$

$$\left(\frac{\xi_w}{d}\right) q_{\delta,z} + \delta = \frac{1}{2}t(\tau), \tag{4.69}$$

$$\left(\frac{\xi_w}{d}\right) q_{m,z} + q_m = 0, \tag{4.70}$$

where the surface *extrapolation length*

$$\xi_w = \frac{L}{w}$$

has been introduced.

We close this section by discussing the requirements to be imposed on the symmetry axis. Inspection of the equilibrium (Eq. (4.65), (4.66), (4.67)) reveals that

$$q_m(0,z) = 0 \; and \; 3q_0(0,z) = -\delta(0,z) \tag{4.71}$$

should be imposed on the symmetry axis $r = 0$ where the factor $1/r^2$ is not defined. It is easy to check that the conditions (Eq. (4.71)) require a uniaxial alignment at $r = 0$, namely

$$Q(0,z) = 6q_0(0,z)(\vec{e}_z \otimes \vec{e}_z - \frac{1}{3}I_{(d)}). \tag{4.72}$$

Using dimensionless variables, imposing uniaxial state along $\vec{e}_z$ amounts at taking

$$q_m = 0, q_0 = \frac{1}{6}t(\tau), and \; \delta = \frac{1}{2}t(\tau). \tag{4.73}$$

If the order is free to vary, then we have to impose

$$q_{0,r}(0,z) = \delta_{,r}(0,z) = q_{m,r}(0,z) = 0 \tag{4.74}$$

to guarantee that $Q$ remains smooth along the symmetry axis. If one is also willing to prescribe the degree of order on $r = 0$, then

$$q_{0,z}(0,z) = \delta_{,z}(0,z) = q_{m,z}(0,z) = 0 \tag{4.75}$$

should be imposed.

### 4.2.2 Structure of solutions

Here we study the structure of the equilibrium texture emerging from the solutions of Eq. (4.65), (4.66), (4.67) subject to the boundary conditions (Eq. (4.68), (4.69), (4.70)) and (Eq. (4.56)). We found it expedient to plot the *degree of biaxiality* $\beta^2$ defined by [155]

$$\beta^2 = 1 - 6\frac{(trQ^3)^2}{(trQ^2)^3}. \tag{4.76}$$

In the cell, $\beta^2$ ranges in the interval [0, 1], it vanishes in all uniaxial states while states with $\beta^2 = 1$ are said to exhibit maximal biaxiality. Since $trQ^3 = 3\det Q$ for all symmetric, traceless tensors, the states with maximal biaxiality are precisely those where one eigenvalue of the order tensor $Q$ vanishes. However, $\beta^2$ fails to be defined in the isotropic state where both $trQ^2$ and $trQ^3$ vanish. In the $(q_0, \delta, q_m)$-space, the loci of maximal biaxiality are the plane $q_0 = 0$ and the conical surface

$$q_0^2 = \delta^2 + q_m^2. \tag{4.77}$$

which is coaxial with the uniaxial cone (Eq. (4.41)).

A second feature of the equilibrium solution we chose to study is the angle $\varphi$ that $\vec{e}_z$ forms with the direction $\vec{n}$ associated with the largest eigenvalues of $Q$. We note that from our computations it follows that $\vec{n}$ always lies in the $\{\vec{e}_r, \vec{e}_z\}$ plane.

### 4.2.3 Mechanical actions

In this section, we compute the mechanical actions that the liquid crystals transmit to the plate $\partial\mathcal{B}$. The transmitted force has a non-vanishing component $\mathcal{F}$ along $\vec{e}_z$ only, while the transmitted torque vanishes identically.

By definition,

$$\mathcal{F} = \int_{\partial\mathcal{B}} \vec{e}_z \cdot T^{(E)}\vec{\nu}\, dA \tag{4.78}$$

where $\vec{\nu}$ is the outer unit normal of $\partial\mathcal{B}$. The tensor $T^{(E)}$ is the Ericksen stress tensor that can be expressed in terms of the bulk free energy density $w(Q) = f_{el}(Q) + f_b(Q)$ as

$$T^{(E)} = WI_{(d)} - \nabla Q \odot \frac{\partial W}{\partial \nabla Q}, \tag{4.79}$$

where

$$(\mathbb{A} \odot \mathbb{B})_{ij} = \sum_{h,k} A_{hki} B_{hkj} \tag{4.80}$$

for any pair of third-rank tensor $\mathbb{A}$ and $\mathbb{B}$. It follows

$$\vec{e}_z \cdot T^{(E)}\vec{e}_z = L\left\{\begin{matrix} 3\left(q_{0,r}^2 - q_{0,z}^2\right) + \left(\delta_{,r}^2 - \delta_{,z}^2\right) + \left(q_{m,r}^2 - q_{m,z}^2\right) + \\ \frac{1}{r^2}[q_m^2 + (3q_0 + \delta)^2] \end{matrix}\right\} \tag{4.81}$$
$$+A(3q_0 + \delta^2 + q_m^2) + 2Bq_0(q_0^2 - \delta^2 - q_m^2) + C(3q_0^2 + \delta^2 + q_m^2)^2.$$

We note that the singular factor $1/r^2$ is harmless since once integrated it is tamed by both the Jacobian $r$ and the fact that $q_m = 0$ and $3q_0 + \delta = 0$ at $r = 0$. By using the same non-dimensional form employed in Section 4.2, we can also write a non-dimensional traction

$$\vec{e}_z \cdot T^{(E)} \vec{e}_z = \frac{B^4}{(4C)^3} -$$

$$\left\{ \begin{array}{c} \left(\frac{\xi_b}{d}\right)^2 \alpha(\theta) \left[ \begin{array}{c} 3\left(q_{0,r}^2 - q_{0,z}^2\right) + \left(\delta_{,r}^2 - \delta_{,z}^2\right) + \\ \left(q_{m,r}^2 - q_{m,z}^2\right) + \frac{1}{r^2}\left(q_m^2 + (3q_0 + \delta)^2\right) \end{array} \right] \\ + \frac{\theta}{6}(3q_0^2 + \delta^2 + q_m^2) + 2q_0(q_0^2 - \delta^2 - q_m^2) + \frac{1}{4}(3q_0^2 + \delta^2 + q_m^2)^2 \end{array} \right\} \tag{4.82}$$

$$= \frac{B^4}{(4C)^3} \tau^{(E)}$$

where we dropped bars to avoid clutter. When the expression (Eq. (4.82)) for the force is inserted into (Eq. (4.78)), we finally obtain

$$\mathcal{F} = \frac{2\pi d^2 B^4}{(4C)^3} \int_0^{R_\infty} r\tau^{(E)} dr, \tag{4.83}$$

where lengths have been rescaled to $d$.

### 4.2.4 Results

Using the derivation described above, we studied the force experienced by a nanoparticle immersed within a nematic LC phase. For this purpose, we consider the LC confined within a cylindrical cell, where the bounding plates impose hybrid boundary conditions. We set that the system exhibits cylindrical symmetry (about the cylindrical axis set at $r = 0$), which is assumed in our derivation. The bottom plate, set at $z = 0$, imposes the homeotropic anchoring (i.e., alignment along the $z$-axis). The top plate (at $z = h$) enforces radial planar anchoring (i.e., alignment along the $r$-direction). At the lateral walls, we impose periodic boundary conditions. Such boundary conditions impose a boojum topological defect at the top plate. Its core structure is described by a *finger*-like structure, which is depicted in Figure 4.9. The *finger* is characterized by a sheet exhibiting maximal biaxiality. It encloses essentially (i.e., weakly biaxial) negatively uniaxial nematic phase, where the center of the *finger* is strictly negatively uniaxial). The outer region of the *finger* is essentially positively uniaxial. Due to topological reasons, the nematic order is melted at the tip of the finger. The resulting nematic structure exhibits three qualitatively different regions: i) the *radial region* closes to the upper plate, which favors a radially streaming nematic structure; ii) the *melted region* surrounding the *fingertip*, where the LC order is essentially isotropic within the separation distance given by the nematic correlation length; iii) the *homogeneous region*, which is pronounced close to the bottom plate, where nematic director field is on average aligned along the $z$-axis.

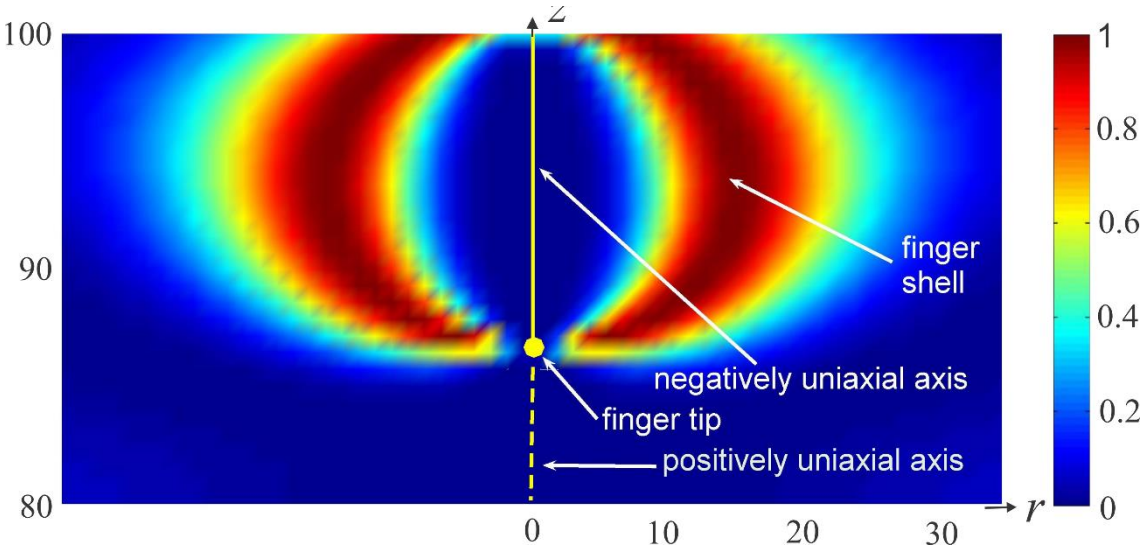


Figure 4.9: Biaxial structure of a nematic structure hosting a boojum.

Hereinafter, we demonstrate that if a nanoparticle is immersed within the LC medium, it is attracted to a region that can best accommodate its locally enforced nematic order. For this purpose, we consider three qualitatively different NP surface treatments imposing to neighboring LC molecules i) radial, ii) isotropic, iii) homogeneous order. We henceforth refer to these nanoparticles as *radial* NP, *isotropic* NP, and *homogeneous* NP.

In all cases, we chose a cylindrical shape of the NP, where its radius and height are equal to the nematic biaxial correlation length. In i), we set it locally strongly enforces radially streaming nematic structure (i.e., uniaxial nematic order along the $r$-coordinate). In ii), we assume that it locally melts the LC order. In iii), we set that it tends to align LC along its symmetry axis. Such "idealized" boundary conditions could be in practice roughly realized by appropriate surface treatment on NPs.

In simulations, we place the NP at the cylinder axis. We place it at different values of $z$ and calculate the resulting nematic structure in the simulation cell. From it, we can calculate the force that the LC environment imposes on the fixed immersed NPs as a function of its position.

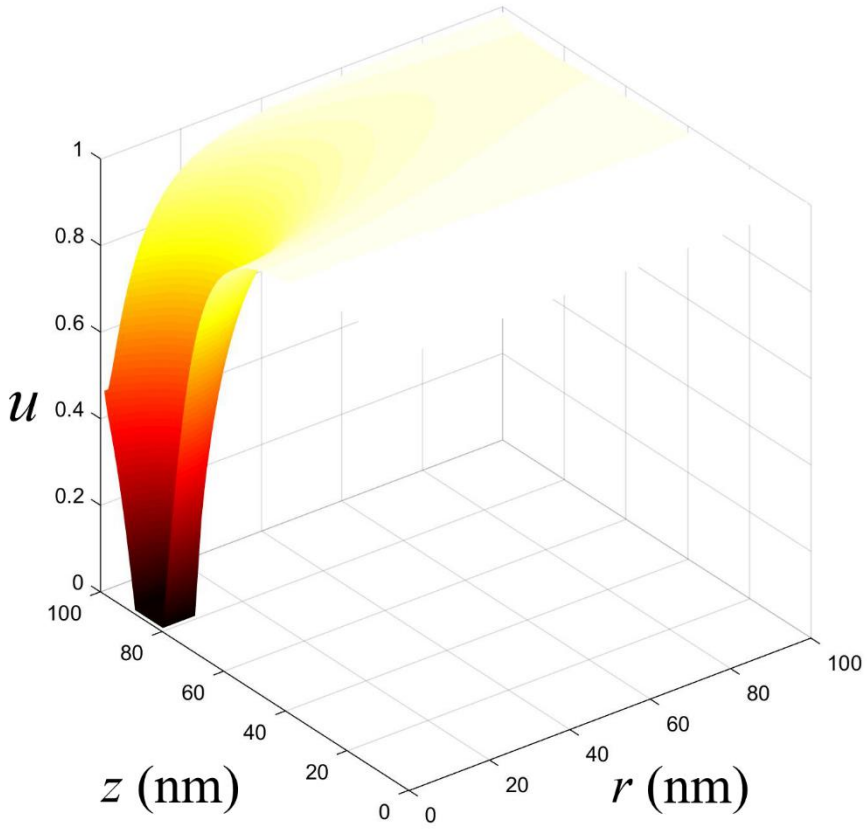


Figure 4.10: Nematic structure in a hybrid nematic cell. The *isotropic* NP is placed close to the top confining plate, which is set at $z = 100$ nm.

In Figure 4.10, we plot the scaled degree of scaled nematic order $u$ for a case where the *isotropic* NP is placed just below the top plate. Here we define $u$ as

$$u = \frac{TrQ^2}{TrQ_b^2},$$

where $Q_b$ determines bulk nematic equilibrium order. The cell width equals $h = 100$ nm. In the volume occupied by the NP, we set $u = 0$ and calculate the resulting nematic structure. In i) Figure 4.11, ii) Figure 4.12, and iii) Figure 4.13 we plot $u = (r, z)$ color textures on varying the position of NPs for the i) *radial* NP, ii) *isotropic* NP, and iii) *homogeneous* NP. For these cases, we calculated the force on NPs which is shown in Figure 4.14. One sees that i) the *radial* NP is attracted to the *radial region*, ii) *isotropic* NP to the *melted region*, and iii) *homogeneous* NP to the *homogeneous region* as predicted. Therefore, NPs tend to assemble in regions that best accommodate the nematic structure that the NPs locally impose.

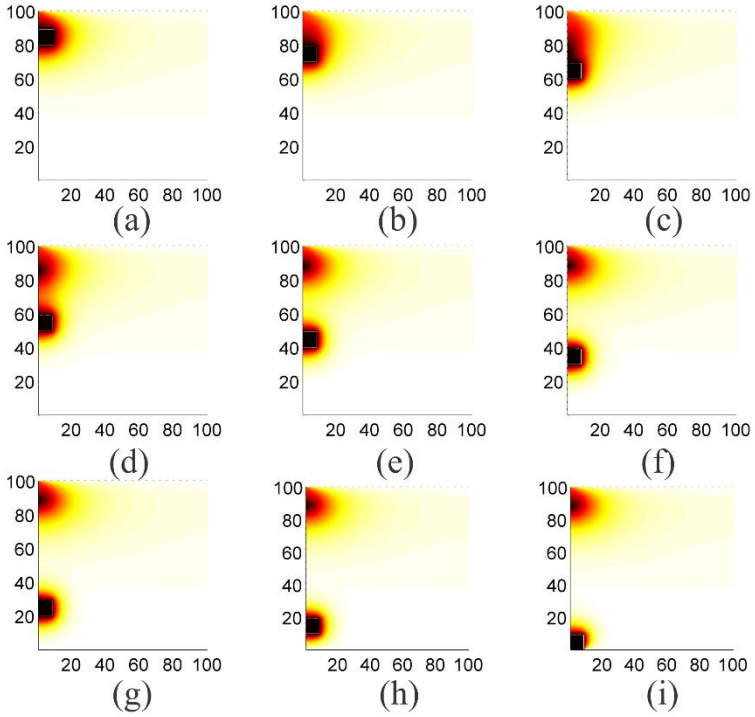


Figure 4.11: The $u = u(r, z)$ color textures on varying the position of NPs for the *radial* NP.

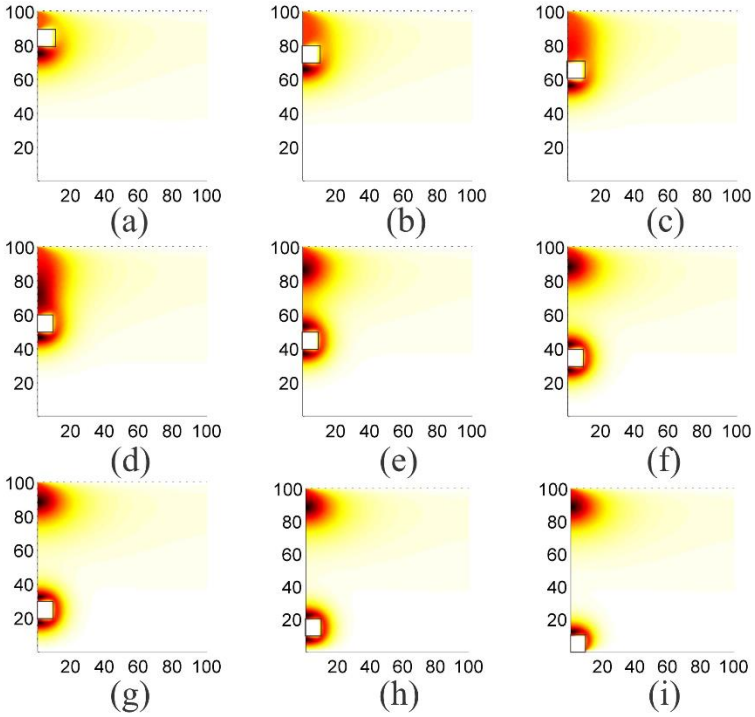


Figure 4.12: The $u = u(r, z)$ color textures on varying the position of NPs for the *isotropic* NP.

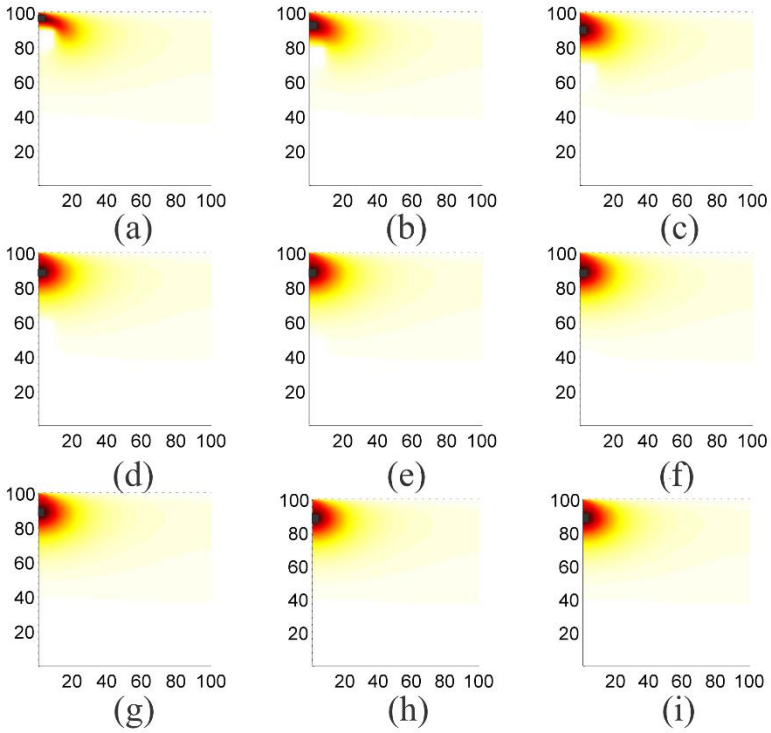


Figure 4.13: The $u = u(r, z)$ color textures on varying the position of NPs for the *homogeneous* NP.

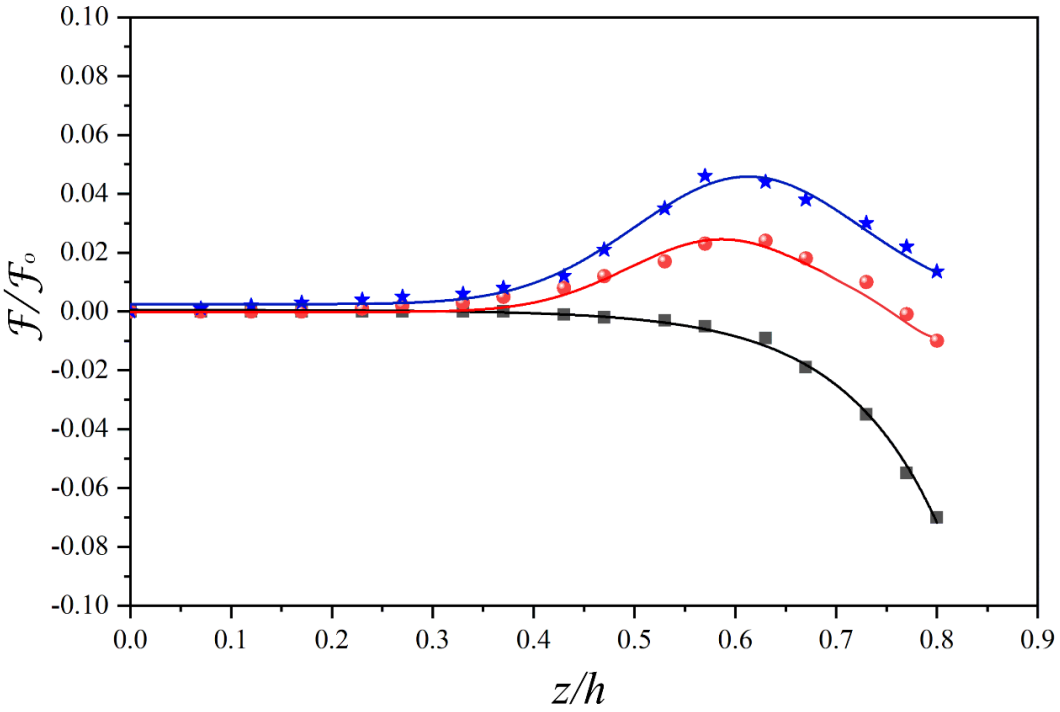


Figure 4.14: The force in units of $\mathcal{F}_0$ exhibited on immersed NPs by the LC order. +: *homogeneous* NP, squares: *radial* NP, circles, *isotropic* NP.

## 4.3 Nanoparticle-Driven Stabilization of Lattices of Line Defects

Hereinafter, we present experimental evidence [14], [85], [86], [92], [98], [99], [116], [118], [126], [156] demonstrating the efficiency of the DCR and ADCT mechanisms in stabilizing lattices of line defects in different NP-LC mixtures of chiral LCs. These studies used NPs of different mass concentrations (NPs mass can be calculated by Eq. (3.1)) having a different characteristic linear size, shape, and surface functionalization. The mass concentration is related to the volume concentration in the diluted regime ($p << 1$) by $\chi \approx p\frac{\rho_{NP}}{\rho_{LC}}$ (see Eq. (3.1)). Here $\rho_{NP}$ and $\rho_{LC}$ stand for mass densities of NPs and LCs, respectively. In these studies, the surface-treated particles were either spherical (CdSe, CdSSe and Au NPs [14], [99], [116], [118], [126] or strongly anisotropic (graphene oxide, laponite and $MoS_2$ nanosheets) [57], [58], [80], [85], [86], [157]. Their main geometrical characteristics are schematically depicted in Figure 4.15 and summarized in Table 4.1. In these studies, a different surface functionalization was used to prevent aggregation of NPs and to improve their adaptivity to defect cores, which is illustrated in Figure 4.16.

Table 4.1: Typical NPs used in experimental studies [85], [86], [126], [156], [157] are listed in this table. $d$ denotes the sphere diameter, $L$ denotes the approximate large nanosheet dimension and $D$ is the thickness of the sheet (all quantities are shown in Figure 4.15)[57]. OA; oleyil amine, TOP; trioctyl-phosphine, PVP; polyvinylpyrrolidone, CTAB; cetyltrimethylammonium.

| Shape | Coating | Core | Dimension (nm) |
|---|---|---|---|
| Spherical | OA, TOP | CdSSe | 3.5 ($d$) |
| Spherical | OA, TOP, PVP | CdSe | 3.5 ($d$) |
| Spherical | OA | Au | 10 ($d$) |
| Nanosheet | OA | Graphene-oxide | 50 ($L$), 3-5 ($D$) |
| Nanosheet | CTAB | Laponite | 25 ($L$), 2 ($D$) |
| Nanosheet | OA | $MoS_2$ | 10 ($L$), 1 ($D$) |

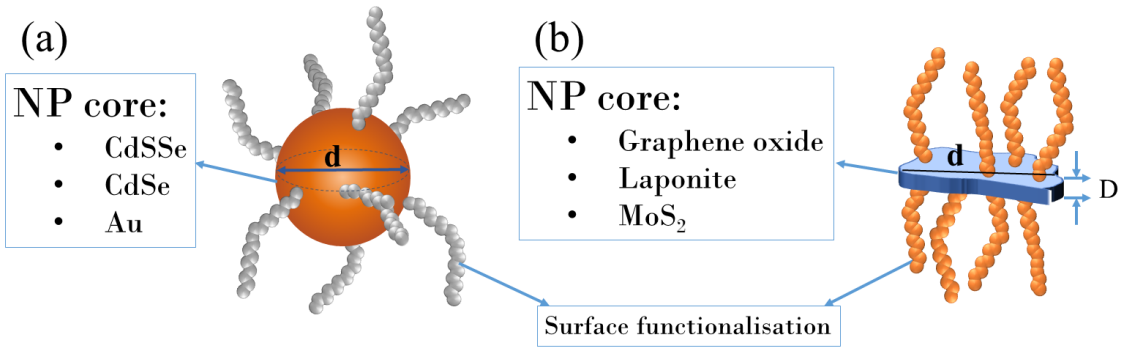


Figure 4.15: A schematic representation of spherical (a) and anisotropic (b) nanoparticle geometries typically used in experiments is shown here [14], [85], [98], [116], [125]–[127], [157]. The used surface coatings are presented in Table 4.1.

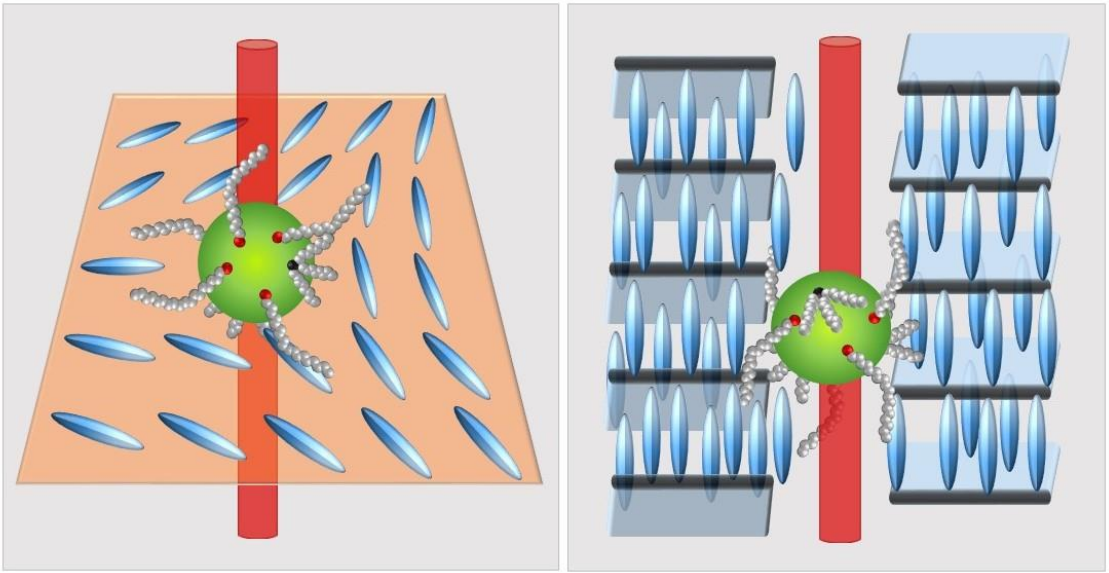


Figure 4.16 Illustrates trapped adaptive spherical NPs within (a) disclination and (b) screw dislocation. The adaptive character is enabled by the flexible molecules covering the NPs surface [57].

In Figure 4.17, the specific heat $c_p$ temperature response of chiral CE8 LC is plotted in a common scale with one concentration $\chi$ of spherical Au NPs [106], [108]. The bulk LC exhibits the phase sequence I–BPIII–BPII–BPI–N*-Sm$A$ on decreasing. Note, that CE8 does not possess a stable $TGB_A$ phase and recent studies indicate that it could be close to the N*–$TGB_A$–SmA triple point [127]. One sees that when dispersing Au NPs in CE8, the temperature range of the BPIII phase increases with respect to the competing phases. Next, finite concentrations $\chi$ nucleate and stabilize $TGB_A$ and $N_L^*$ phase.

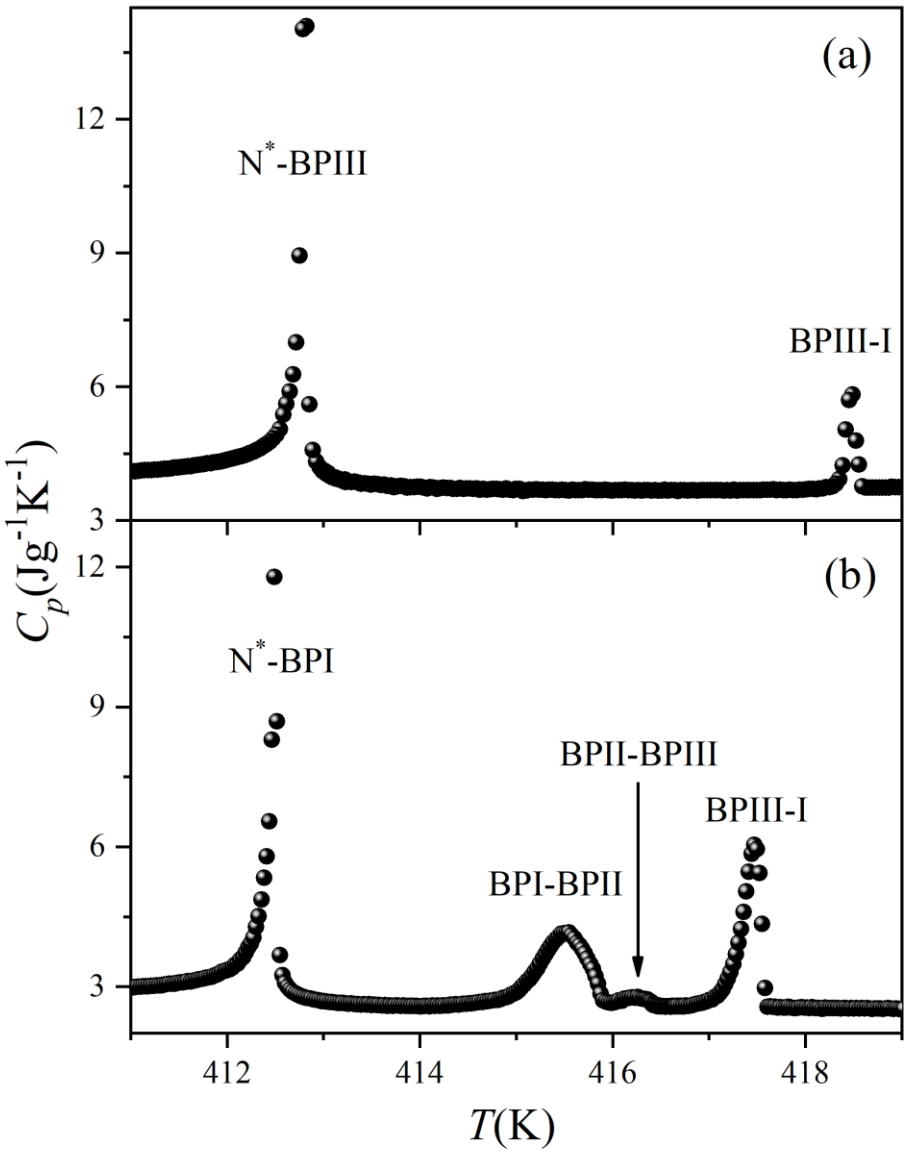


Figure 4.17: The ac calorimetry measurements of a mixture of CE8 and Au NPs. The heat capacity profiles for (a) mixture of CE8 with spherical Au NPs ($\chi = 0.0005$) [158] and (b) pure CE8 [99].

In Figure 4.18, the impact of various types of anisotropic nanoparticles (nanosheets) such as graphene oxide, $MoS_2$, and laponite on the blue phase range of CE8 is shown upon cooling [85], [86], [157]. While for spherical NPs, mostly the macroscopically amorphous BPIII is stabilized [52, 54], for nanosheets with large surfaces, the more ordered BPI structure prevails [78], [85], [86], [91], [157].

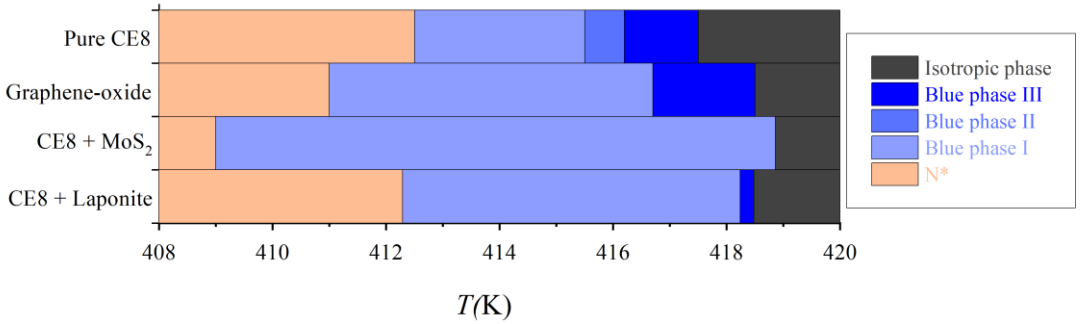


Figure 4.18: The influence of surface-functionalized anisotropic NPs (graphene oxide, $MoS_2$, laponite) on the BPs of CE8 is schematically depicted here. In all cases, the BPI structure is mainly stabilized over the other competing phases [57].

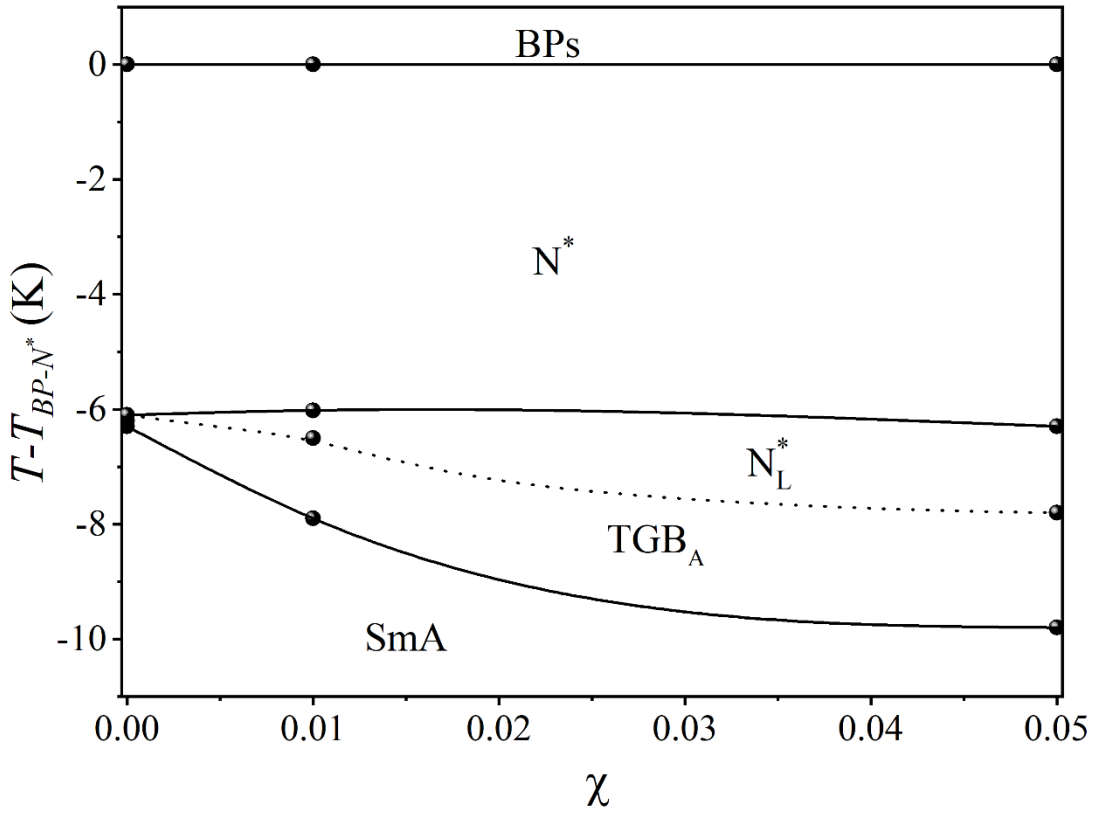


Figure 4.19: Concentration-temperature phase diagrams in mixtures of CE8 and CdSSe (spherical) NPs [57].

We next focus on the impact NPs on $TGB_A$ stability [126], [156]. In Figure 4.19, we plot the temperature window $\Delta T_{TGB}^{NP}$ of the $TGB_A$ and $N_L^*$ stability on increasing $\chi$ for CdSSe NPs. One sees that $\Delta T_{TGB}^{NP}$ monotonously increases. Previous results by *Trček* [159] and *Lavrič* [158] on larger spherical Au NPs show that the latter stabilize both lattices of disclinations (BPs) and dislocations ($TGB_A$ and$N_L^*$), similar to what was observed in the case of smaller CdSe quantum dots [14]. Note that the cores of disclinations and dislocations are significantly different, as shown in Figure 4.16.

## 4.4 Stabilization of Phases with Magnetic NPs

In this section, we present the experimental results and the discussion related to the existence and stabilization of $TGB_A$ and blue phase in chiral compound CE8 by adding magnetic NPs.

### 4.4.1 Stabilization of blue phase by magnetic NPs

Recent studies by *Karatairi et al.* [116], *Rožič et al.* [99], *Lavrič et al.* [85], [86], [157] and *Cordoyiannis et al.* [160] reported that different types of NPs in were used mixtures with CE8. To study the impact of NPs core composition, magnetic NPs mixtures were prepared at different concentrations.

#### 4.4.1.1 Existence of blue phase in pure CE8

It is well known, that pure CE8 exhibits all three blue phases in a total range of 2-3K [116] upon reducing temperature (Figure 4.20). The cholesteric BPs appear in a narrow temperature range between the isotropic and the cholesteric phase of highly chiral thermotropic LCs [66], [161]–[163] and, barely, in a lyotropic system [164], [165]. Upon cooling, BPIII, BPII, BPI appear, BPIII is macroscopically amorphous with a local cubic lattice in the director field, a 3D cubic periodicity characterizes BPII in the director field and BPI exhibits a body-centered cubic symmetry of the director field [71], [72], [132], [166], [167]. The existence of the BP range as a function of increased chirality was demonstrated in phase diagrams of racemic-chiral mixture [168]. Their thermodynamic stability was confirmed by identifying the distinct thermal signatures of I–BPIII, BPIII–BPII, BPII–BPI, and BPI–$N^*$ transitions for cholesteryl non-anoate [169]. Their critical behavior as a function of chirality was also explored [71], [170] and finally an elaborate temperature-chirality phase diagram was experimentally derived [171], demonstrating the existence of a critical point for the I-BPIII transition at strong chiralities and a triple point where all three BPs coexist [125]. In the late 90s, the BP phase diagrams were revisited and the critical behavior as a function of chirality was well-understood [171]–[173]. So far, several reports exist in the literature proposing different strategies to widen the temperature range of BPs. Stabilization in the range of a few K up to a few tens of K has been achieved for various systems such as polymer composites [92], [174]–[178], nanoparticles [85], [95], [98], [116], [125].

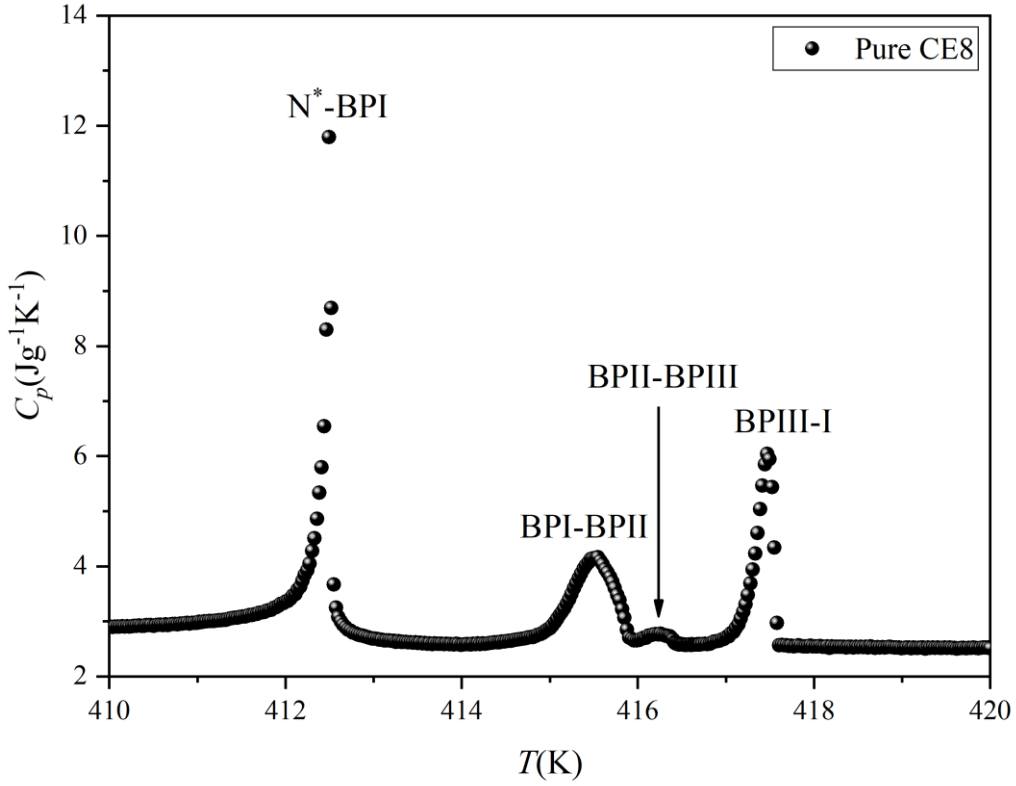


Figure 4.20: Heat capacity of pure CE8 cooling run [116]. The sample was initially heated up to the isotropic phase and then cooled along the blue phases down to the cholesteric phase with a scanning rate of 250 mK/h. The onset of BPIII was observed at 417.55 K.

#### 4.4.1.2 Heat capacity results

The temperature profiles of specific heat capacity $C_p(T)$ results obtained by ac calorimetry with three concentrations, i.e. $\chi = 0.0001, 0.001$ & $0.01$ are shown in Figure 4.21. The heat capacity data were obtained upon both cooling and heating from the I–N$^*$ phase with a scanning rate of 250 mK/h. The $C_p(T)$ profile of pure CE8 [99] is shown at the bottom layer at the same temperature range compared with other NPs mixtures. The $C_p(T)$ demonstrates well that all concentrations of magnetic NPs have a visible impact on the phase transition behavior of pure CE8. The heat runs to confirm the phase sequence and the range of phases mentioned above are thermodynamically may/may not stable, upon both heating and cooling (Figure 4.22). The pretransition peak/wing of the specific heat, another shoulder-like feature, indicates two possible scenarios [159]. i) This indicates another BPs region of an approximately 1 K wide temperature range or ii) it could be a mean non-constant conversion rate between the two phases temperature range anyway, POM will reveal this. As in Figure 4.21, the top two concentrations, $\chi = 0.001$ & $0.01$, did not show visible confirmation of I-BP transition. In the heat capacity runs upon both heating and cooling, sometimes the isotropic to blue phases transitions are not visible because of 1$^{st}$ order transition character in CE8. In contrast to other highly chiral compounds like CE2 and CE4, I-BPIII transition becomes supercritical [171], [173].

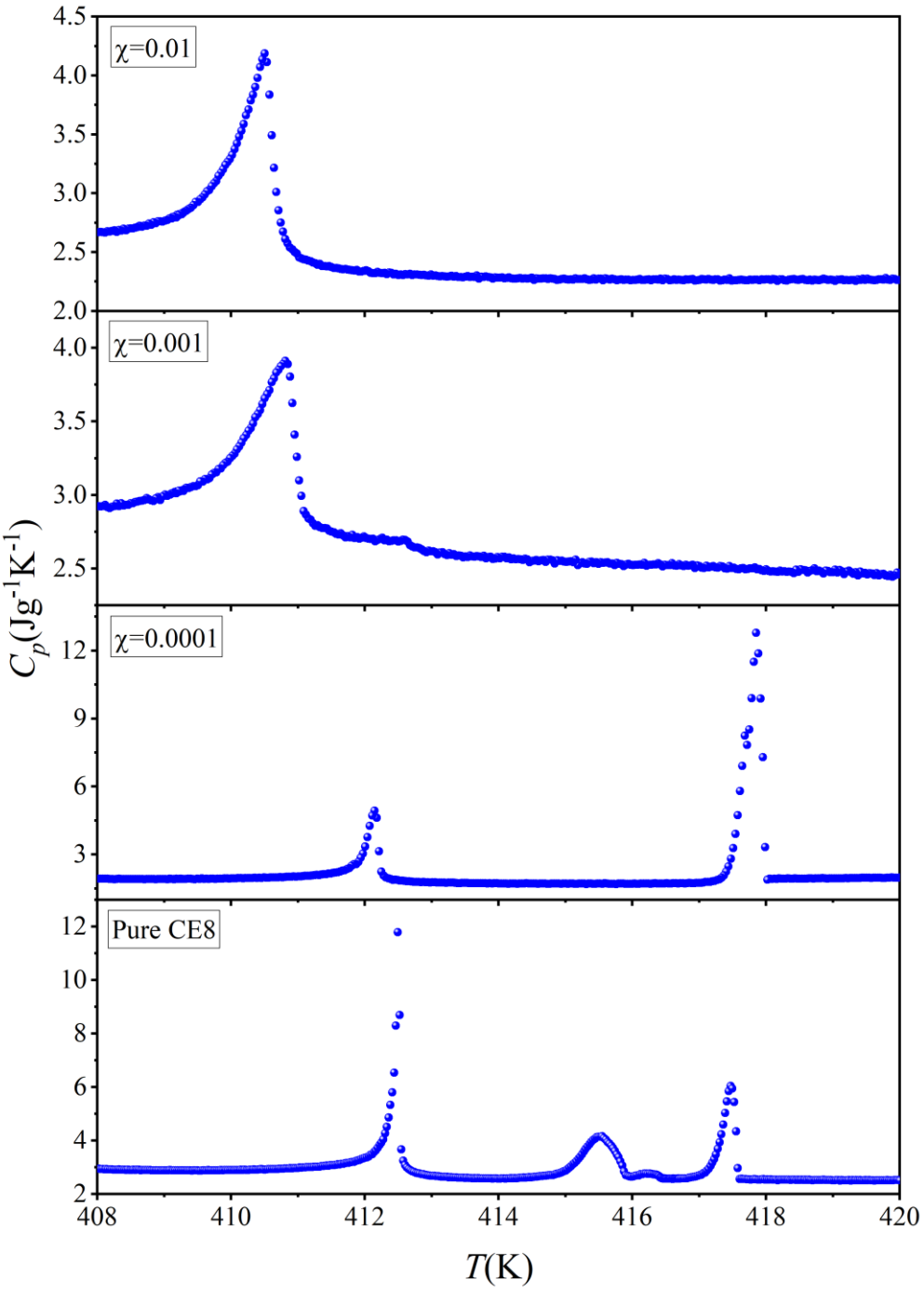


Figure 4.21: The temperature dependence of specific heat $C_p(T)$ for CE8 and mixtures of pure CE8 (data taken from [99]) with $\chi = 0.0001, 0.001$ & $0.01$ magnetic NPs. Data points were obtained upon cooling with a scanning rate of 250 mK/h. The top two $\chi = 0.001$ & $0.01$ mixtures did not show the I–BP transition due to strong 1$^{st}$ order transition. For this, we have visible confirmation from POM.

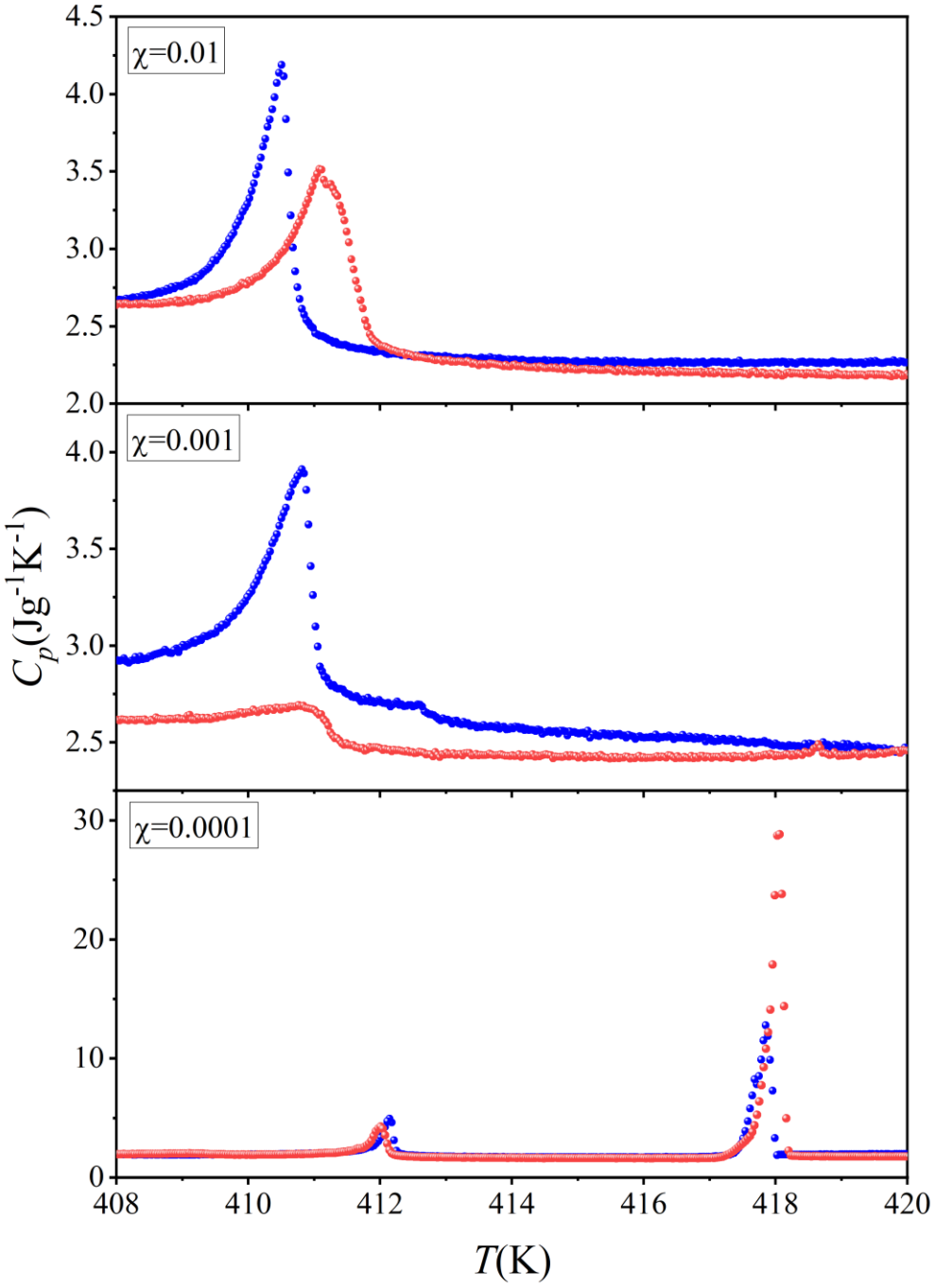


Figure 4.22: The $C_p(T)$ as a function of temperature obtained by ac calorimetry is shown for three mixtures, i.e. $\chi = 0.0001, 0.001$ & $0.01$. Both runs, heating (red) and cooling (blue), are presented with a scanning rate of 250 mK/h.

In detail, a mild widening of BP temperature range is observed, from 5.0 K for pure CE8 to 5.9 K for $\chi = 0.0001$, 7.0 K for $\chi = 0.001$, and 6.9 K for $\chi = 0.01$. For all three concentrations, the total BP range increases and the transition temperature between I-BP is shifted to higher. The I-BP transition signature ($T_{I\text{-}BP}$) is observed here ($\Delta T_{I\text{-}BP}$ =0.9 K, 2.0 K, 1.9 K) shifted with respect to pure CE8, respectively. The phase transition peaks from BPIII- BPII and BPII-BPI in pure CE8 vanished in the presence of magnetic NPs. Only $\chi = 0.001$ mixture exhibited a small trace of BPI-BPII transition. Both cooling and

heating runs are presented in Figure 4.21 and Figure 4.22 and confirmed between a small hysteresis of 0.5 K is observed and these are related to the 1st order transition. In order to identify the particular BPs, the POM measurements were performed.

#### 4.4.1.3 POM results

The optical textures have been examined for the additional confirmation of phase sequence derived by high-resolution calorimetry. All the images were sensibly taken under optical microscopy upon cooling at different concentrations (i.e. $\chi = 0.0001, 0.001 \,\&\, 0.01$) with a mixture of pure CE8. Non-treated cell preparation is given in Section 3.3.1. The temperature is slowly changed, used an average scanning rate of 0.02K per 1 min cooling to determine whether BPs are present in the given sample.

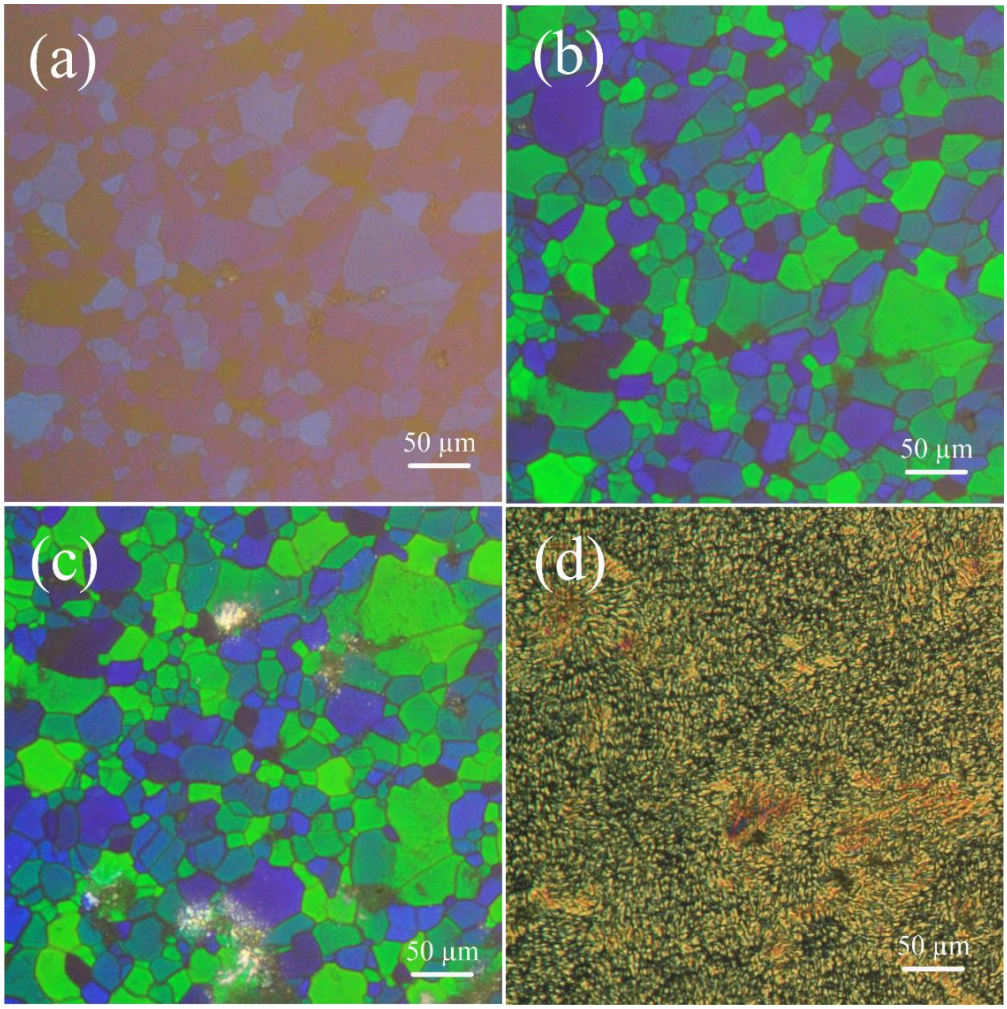


Figure 4.23: Polarizing optical microscopy textures obtained on cooling for $\chi = 0.0001$ mixture. Presence of (a) the formation of blue phase, (b) BPI, (c) $N^*$ domains developing within BP, and (d) $N^*$.

The images are captured at multi-temperature ranges in the transmission mode under polarizers for all the mixtures ($\chi = 0.0001, 0.001 \,\&\, 0.01$). Figure 4.23a shows the foggy blue phase known as BPIII and clear evidence of BPs, where the large-size platelets attributed to BPI appearing on cooling. Also, got see the transformation from the BPIII–BPI–$N^*$ phase, upon cooling on BPI slowly developing $N^*$ domains within. The evolution of BP textures at different temperatures in panels (a) foggy BP, (b) stable BPI, (c) the

appearance of $N^*$ domains, and (d) stable $N^*$. All the textures mentioned above remain stable when leaving the sample for longer time scales at a fixed temperature.

The POM texture confirms that the remaining BPs, by mixing of $\chi$ =0.001 magnetic NPs with chiral CE8 LC, is reasonably stabilized and temperature wide with increasing $\chi$ as shown in Figure 4.24.

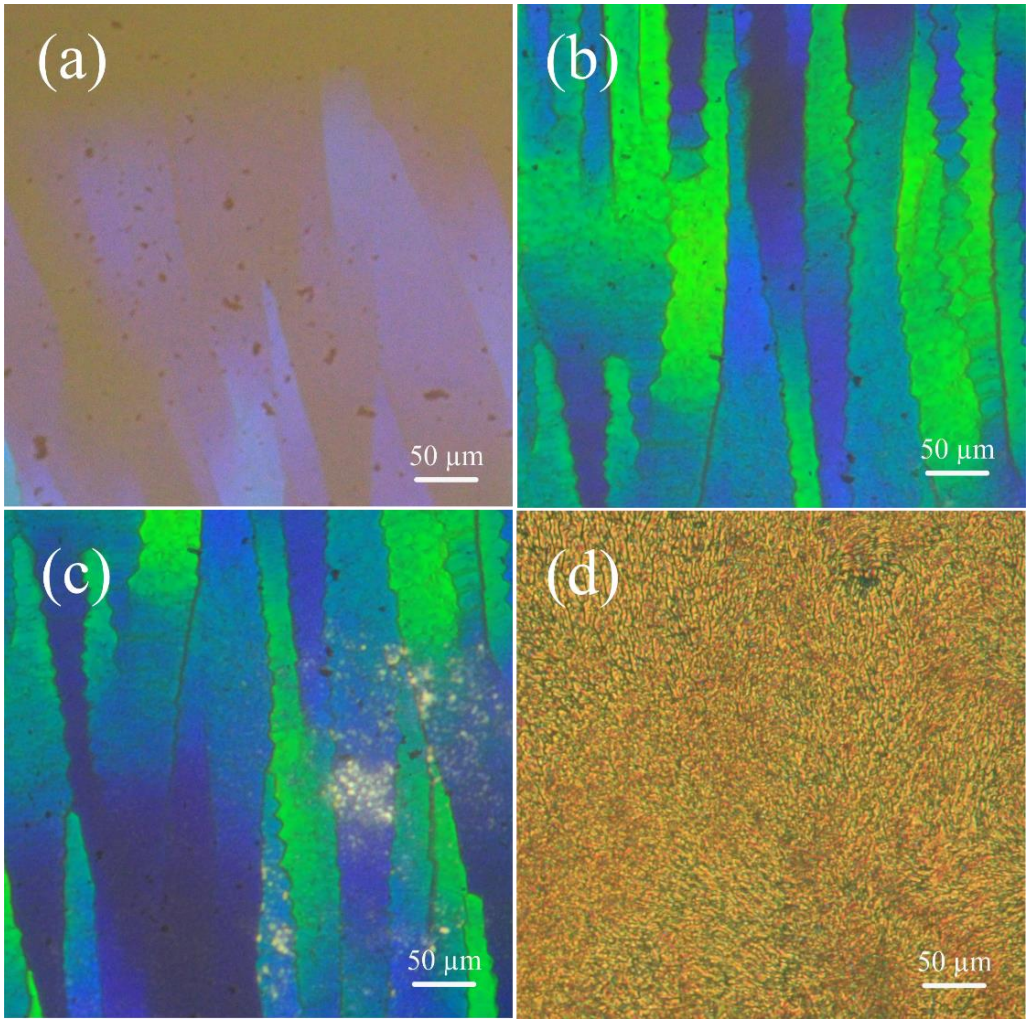


Figure 4.24: Polarizing optical microscopy textures obtained on cooling for $\chi = 0.001$ mixture. Presence of (a) the formation of blue phase, (b) BP, (c) $N^*$ domains are developing within BP, and (d) $N^*$.

The POM images for chiral CE8 and magnetic NPs with $\chi = 0.01$ are presented in Figure 4.25. By increasing the $\chi$ concentration, BP was stabilized at the same time $\chi$ consternation became high and NPs over-exploited.

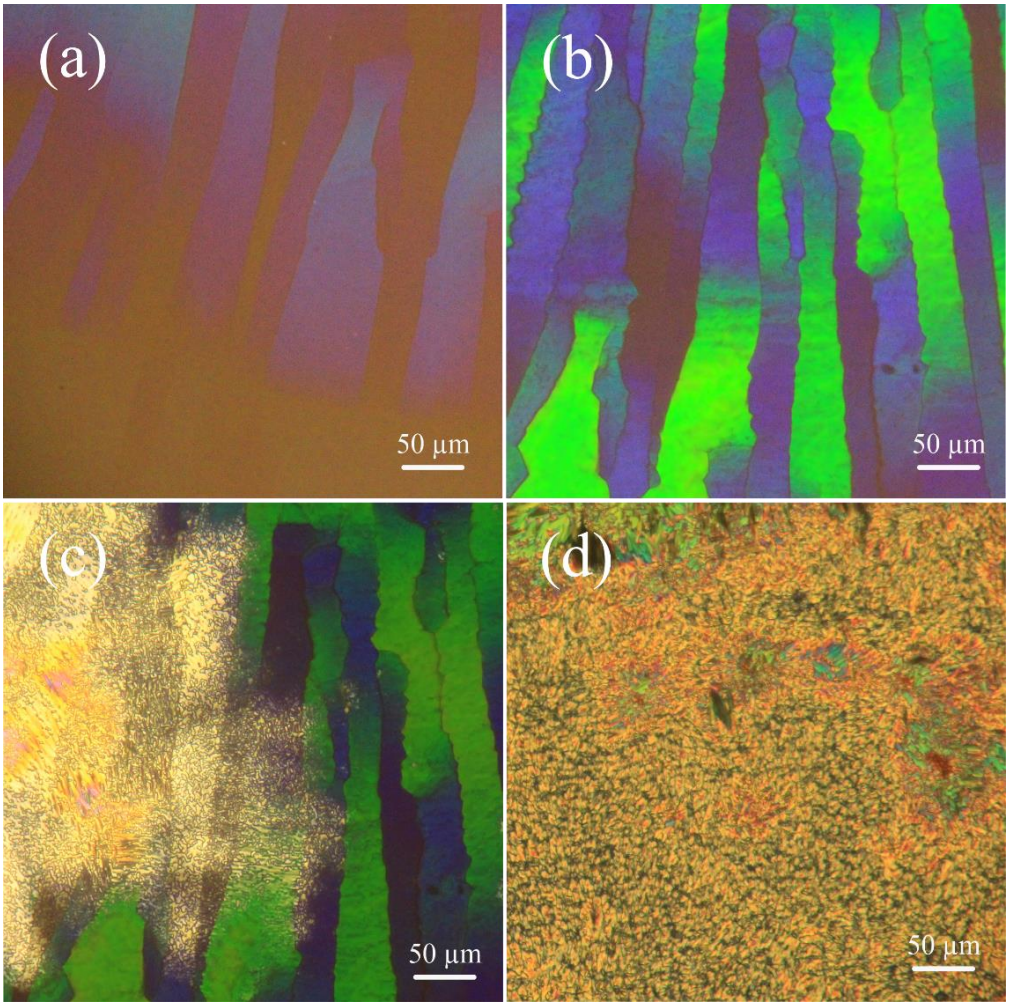


Figure 4.25: Polarizing optical microscopy textures obtained on cooling for $\chi = 0.01$ mixture. Presence of (a) the formation of blue phase, (b) BPI, (c) $N^*$ domains developing within BP, and (d) $N^*$.

#### 4.4.1.4 Phase diagram

The temperature-concentration $(\chi - T)$ phase diagram of the CE8 and magnetic NPs mixtures (i.e. $\chi = 0.0001, 0.001 \,\&\, 0.01$) is presented in Figure 4.26. POM textures derive the phase sequence and ac calorimetry has been examined upon both cooling (only POM) and heating cycles. Both optical microscopy and ac calorimetry results well agree with each other. The five insets in Figure 4.33 shows the characteristic textures of the BPI, $N^*$, $N_L^*$, $TGB_A$ and SmA phases at given mixtures.

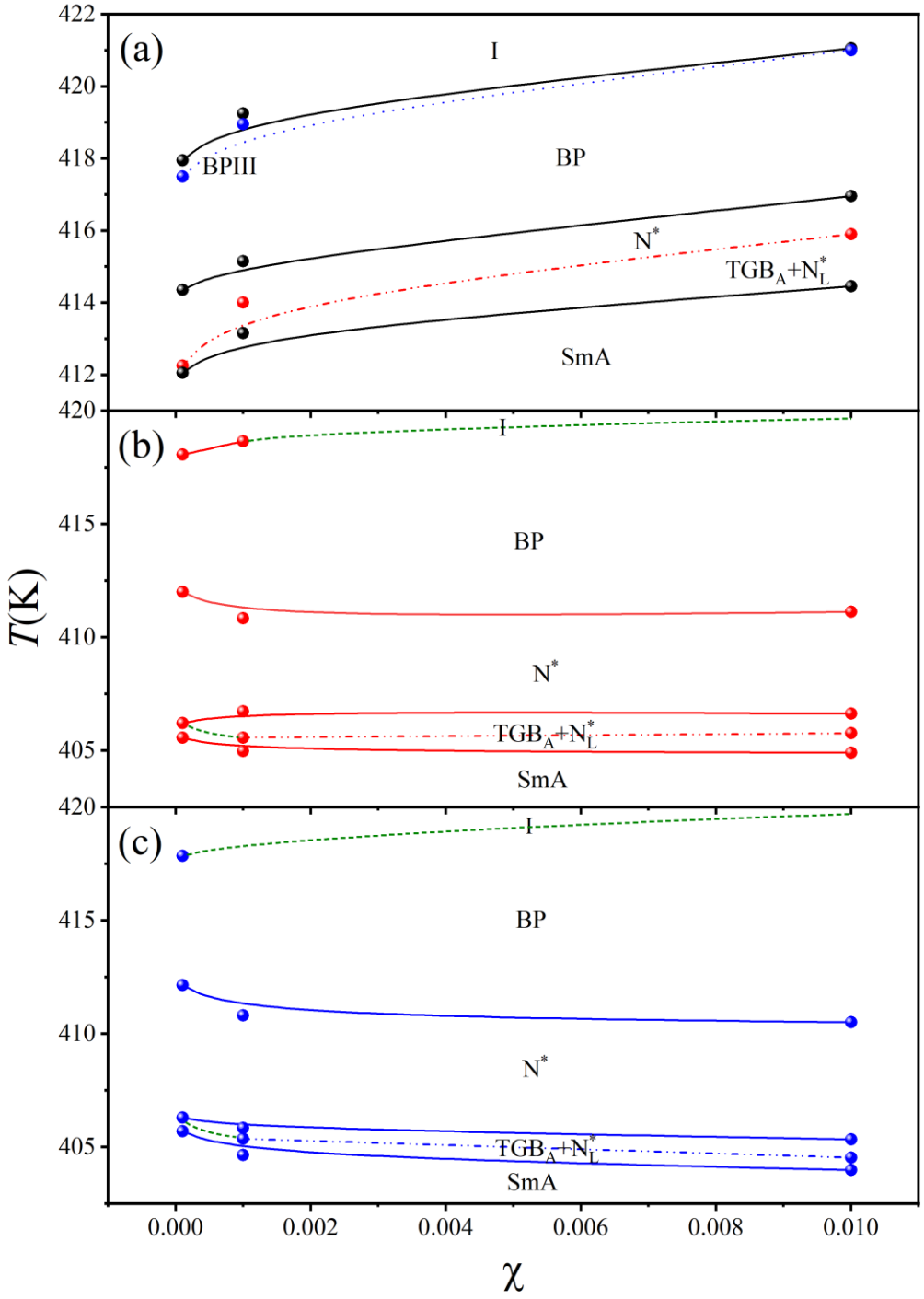


Figure 4.26: The phase diagram $\chi - T$ of CE8 and magnetic NPs mixtures. (a) Based on optical texture temperatures, the data obtained upon cooling, (b) heat capacity data upon heating, and (c) heat capacity data upon cooling. Since I-BP transition peak $\chi = 0.001$ & $0.01$ has not been detected by ac calorimetry, we have a visible confirmation of I-BP transition by optical microscopy. Considering this, the green lines are drawn to show the I-BP transition.

As mentioned in the previous section, the heat capacity results failed to show the transition peak between I–BP phases, as shown in Figure 4.26b and Figure 4.26c. To

overcome this, we have visible confirmation from POM data presented in the top layer. There you could observe the existence of the BPIII phase at a lower concentration, and it is vanishing while increasing the NPs concentration. It is a clear indication by the phase diagrams, BPIII structure is slowly disappeared and BPI becomes stable and wider while increasing the NPs concertation as you can see in Figure 4.33. The solid circles represent the phase transition temperatures obtained by both POM and ACC methods. The dotted lines (Figure 4.26b and Figure 4.26c) indicated the imaginary I–BP transition lines inspired by POM data collection.

#### 4.4.1.5 Discussion of the BP stabilization by magnetic NPs

Both POM and calorimetric results show a wider BPI range higher BPI–N$^*$ phase transition temperatures. From the I–BPI transition, the heat capacity anomaly of the I–BP transition remains sharp and analogous to the pure CE8 even for all the concentrations reported. The transition temperatures between I–BPI remain rather close to the pure CE8 for low concentration mixtures (i.e. $\chi = 0.0001$). It is a good sign that even a smaller concentration of magnetic NPs is enough to suppress the BPII range acting in similar as in [86], [99], [116], [157], [158]. It is well known that only the pure CE8 could exhibit the BPIII–BPII transition (Figure 4.20). However, at all three concentrations, a small range of BPI is still present.

The heat capacity and optical microscopy results were combined to construct the phase diagram for mixtures of pure CE8 and magnetic NPs. The phase diagram $\chi - T$ of given mixtures with magnetic NPs is presented upon cooling in Figure 4.26. It is clearly demonstrated that both BPIII and BPII are suppressed at even very small concentrations ($\chi = 0.0001, 0.001$ & $0.01$) of magnetic NPs. The phase diagram $\chi - T$ of mixtures with magnetic NPs is rather similar to those of Au nanorods [158], [159] demonstrating an extended stabilization of BPI and rather fast suppression of BPIII phases with increasing $\chi$. It appears that used magnetic NPs efficiently stabilize only the BPI structure by magnetic NPs assembling at the cores of defects, like in the cases of Au nanorods and platelet NPs [158].

As mentioned earlier, similar findings were observed in anisotropic Au nanorods. In both cases (magnetic NPs and Au nanorods), only BPI was stabilized while BPII and BPIII were suppressed. As in the case of NPs platelets induce the nematic order and destroy isotropic symmetry due to their anisotropic nature. This means that the magnetic NPs stabilize BPI with lower symmetry close to the long-range nematic order. Thus, the chain formation could be made by magnetic NPs. The formation acts as rods, indicating the possible formation of anisotropic cluster formation of magnetic NPs in defect cores mimicking the Au nanorods.

Concerning the I–BP transition temperature, as revealed by previous studies that I–BP transition is slightly shifted towards lower temperature or stays the same for small spherical NPs. In the case of large spherical NPs, I–BP transition temperature is increased. In the case of magnetic NPs, which are similar to spherical Au NPs and Au nanorods, the $T_{I\text{-}BP}$ transition temperature increases. The $T_{I\text{-}BP}$ transition shift is related to the interplay of several mechanisms. First, it appears that in general the same DCR mechanism is present in the mixture and that imposes the $T_{I\text{-}BP}$ increase. However, this is less efficient when a sample is approaching the $T_{I\text{-}BP}$, where the correlation length attains its maximum value and the volume occupied by defects is larger. Second, the elastic distortion induced by the NPs imposes the opposite tendency, i.e., decreases $T_{I\text{-}BP}$. Another elastic mechanism is a reduction of fluctuation of disclination lines due to the assembling of heavy NPs such as spherical Au and large anisotropic NPs within the defect cores or their vicinity.

### 4.4.2 Stabilization of $TGB_A$ by magnetic NPs

Recent studies by *Trček et al.* [126], [127], [156] reported the stabilization of the $TGB_A$ phase in a mixture of chiral LC and surface functionalized NPs. Effectively, they stabilize the one-dimensional lattice of screw dislocations, thus establishing the $TGB_A$ order between the cholesteric and SmA phases. Here we present the experimental results and the discussion related to the stabilization of the $TGB_A$ phase in chiral CE8 LC compound by adding magnetic NPs at different concentrations.

#### 4.4.2.1 Existence of $TGB_A$ phase in pure CE8

Many reports followed and the TGB phases are generally observed in chiral LCs, LCs mixtures, and in mixtures of LCs with chiral dopants [132], [179]. Based on the calorimetry results that have been reported in Ref. [99], [116], the $TGB_A$ phase does not exhibit in pure CE8 compound and it goes directly from the SmA to $N^*$ phases [99], [116], [126], [127] as you can see in Figure 4.27. There could be a possibility, explained by *Wilson et al.* [180], the $TGB_A$ phase in CE8 could exist in a narrow range temperature. In order to confirm this statement, additional experiments such as optical microscopy and heat capacity have been studied. The obtained results shown below suggest that at best some non-equilibrium $TGB_A$ domains could be seen in a narrow temperature range along with $N^*$ and SmA domains. This demonstrated that the pure CE8 could be closer to triple point such as $N^*$–$TGB_A$–SmA and experimentally it was first observed by *Renn* and *Lubensky* [115] also, the sequence cholesteric–$TGB_A$–SmA was first observed by *Lavrentovich et al.* [112]. A recent study by means of POM suggests that the $TGB_A$ phase exists in a metastable state with strong fluctuations for pure CE8. However, it could become stable for particular anchoring conditions [127]. Recently, the $TGB_A$ phase has been induced by CdSe and CdSSe quantum dots dispersed in chiral LC hosts by *Trček et al.* [126], [127].

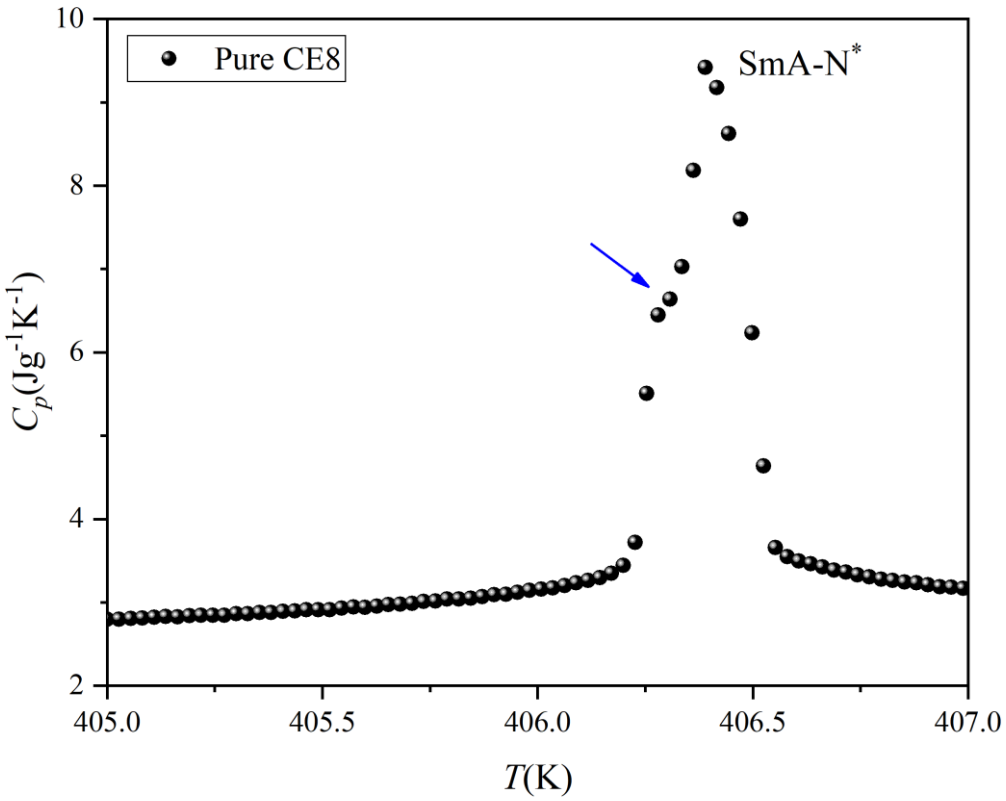


Figure 4.27: Heat capacity of pure CE8 cooling run [99]. The sample was initially heated up to the isotropic phase and then cooled along with the blue phases down to the cholesteric phase, upon cooling with a rate of 250 mK/h. The arrow is showing some meta-stable TGB could exist.

#### 4.4.2.2 Heat capacity results

The heat capacity $C_p(T)$ results for pure CE8 and three mixtures $\chi = 0.0001, 0.001$ & $0.01$ near the N*–SmA phase transitions are shown in Figure 4.28. The heat capacity data were obtained upon both cooling and heating from the N*–SmA phase with the scanning rate of 250 mK/h. The $C_p(T)$ profile of pure CE8 is shown at the bottom layer at the same temperature range compared with NPs mixtures. It should be noted that there was no orientation was imposed on the sample cell walls during calorimetric measurements.

The pure CE8 data was used from the previous experiments [99], as mentioned that CE8 undergoes a 1st order phase transition from N*–SmA with a smaller shoulder at a low-temperature wing. As it is clearly visible in Figure 4.28, the temperature profiles of $C_p(T)$ demonstrate well that all the concentrations of magnetic NPs have a good impact on the phase transition behavior of $TGB_A$. By increasing the NPs concentration, the transition peak shifts towards higher temperatures and at the same time becomes broader. Then the presence of magnetic NPs progressively seamer the transition between N*–SmA phases and a visible shoulder was created at a low-temperature wing of $C_p(T)$ data, representing the presence of the $TGB_A$ and a small trace of $N_L^*$ phase. Based on the calorimetric data, the $C_p(T)$ peak of the $\chi = 0.0001$ mixture shows a small widening; however, the aforementioned low-temperature anomaly is clearly visible for the $\chi = 0.001$ mixture. Lastly, it becomes very pronounced for the $\chi = 0.01$ mixture, where the $TGB_A$ phase is stabilized in a

temperature range of ~3.0 K. Similar kinds of results were reported by Dr. Maja Trček's thesis [159].

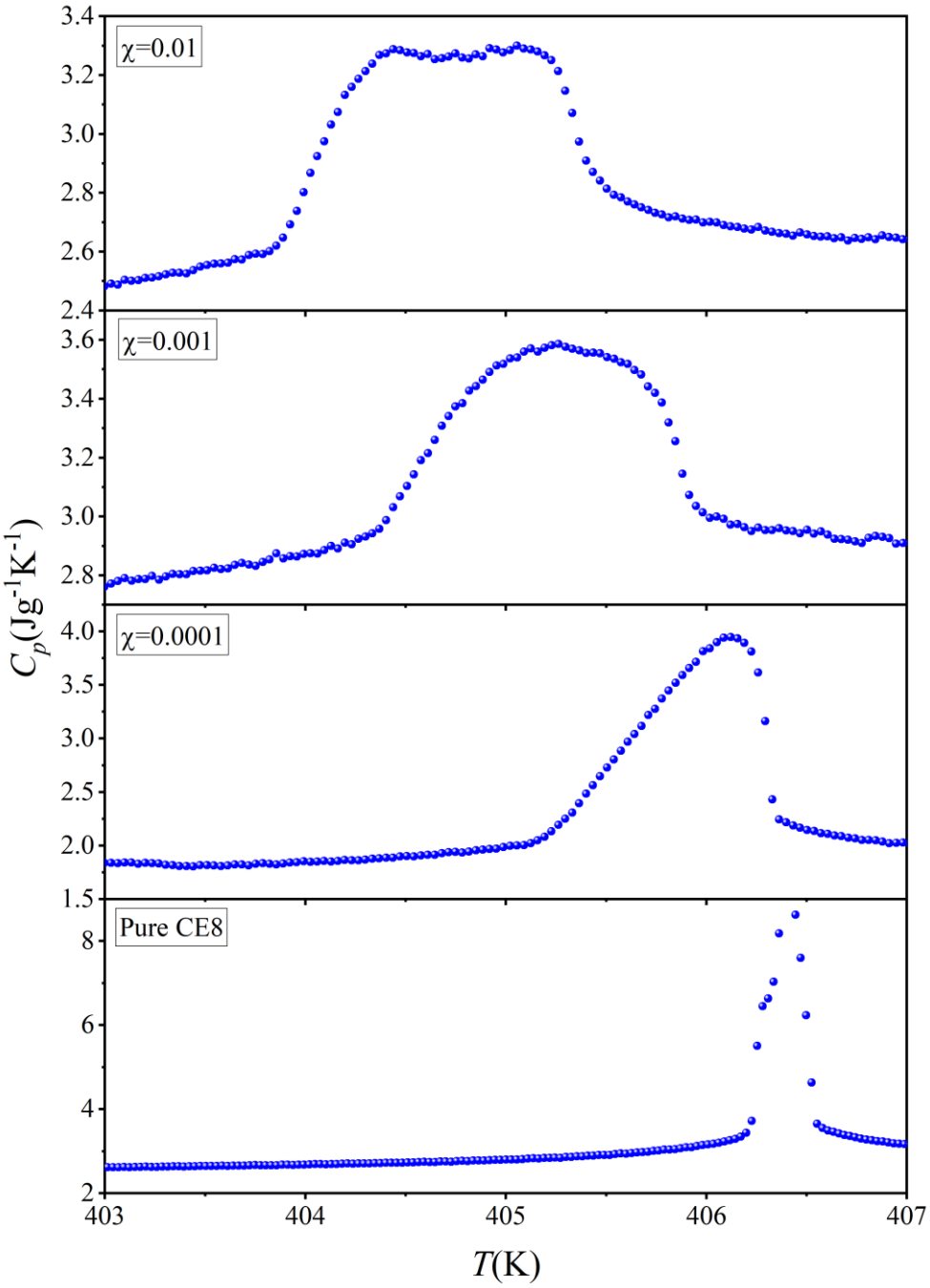


Figure 4.28: The temperature dependence of specific heat $C_p(T)$ for pure CE8 (data taken from [99]) and mixtures of pure CE8 and the mixtures $\chi = 0.0001, 0.001$ & $0.01$ magnetic NPs. Data points were obtained upon cooling with a scanning rate of 250 mK/h.

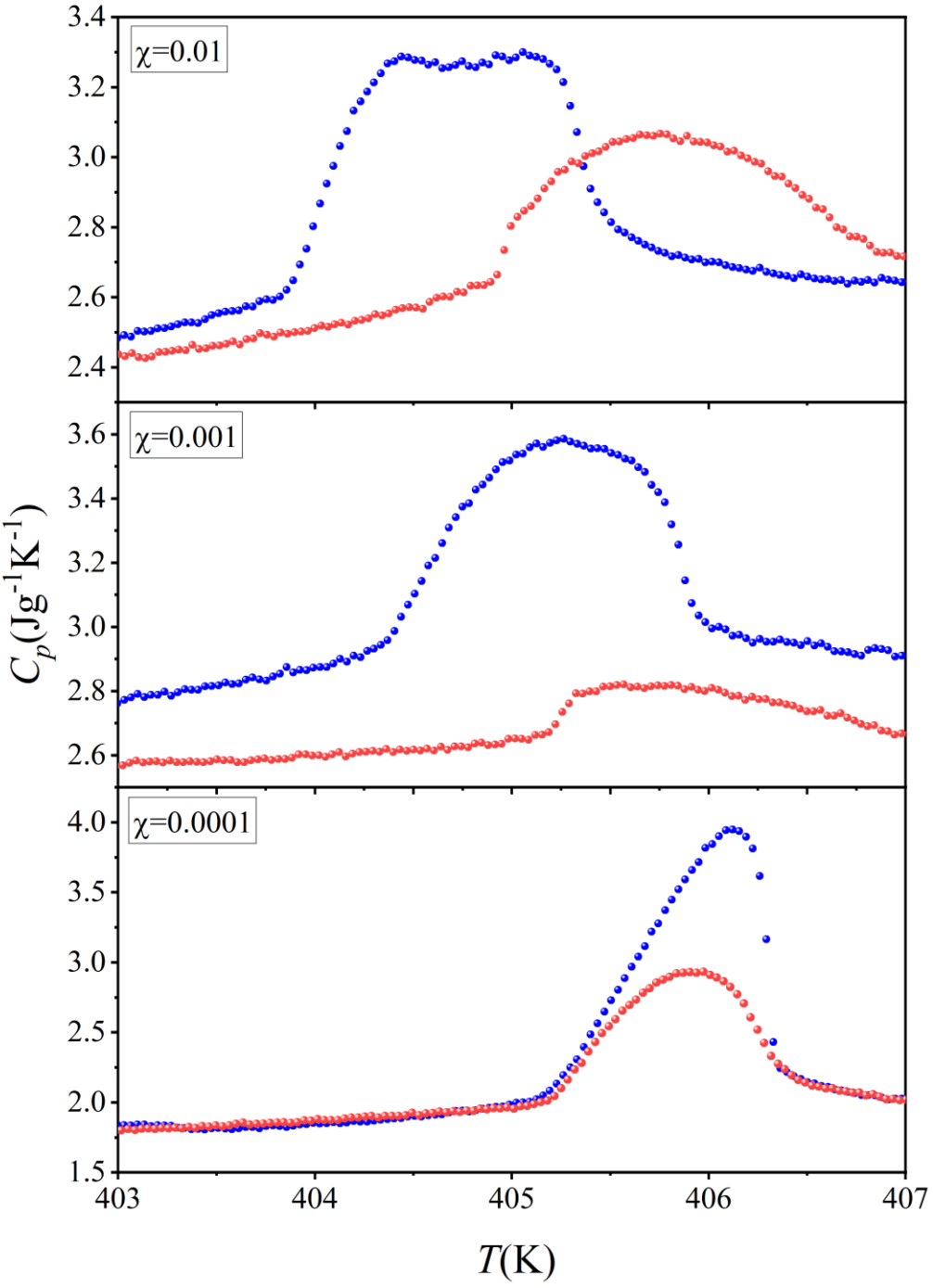


Figure 4.29: The heat capacity $C_p(T)$ as a function of temperature obtained by ac calorimetry is shown for three mixtures, i.e. $\chi = 0.0001, 0.001$ & $0.01$. Both runs, heating (red) and cooling (blue), are presented with a scanning rate of 250 mK/h.

#### 4.4.2.3 POM results

The presence of the $TGB_A$ phase was observed with the help of the optical textures. The mixture of magnetic NPs in chiral CE8 LC was trapped in non-treated cells. The optical textures have been examined upon the cooling cycle. All the images were sensibly taken under the POM at different concentrations with a mixture of pure CE8 as shown in Figure 4.30, Figure 4.31, and Figure 4.32. The temperature is slowly changed, using an average

scanning 0.02 K per 1 min cooling rate to find out the non-existing $TGB_A$ and $N_L^*$ phases in the given sample. The images are captured at various temperatures in the transmission mode under polarizers for all the mixtures ($\chi = 0.0001, 0.001$ & $0.01$). So far, there is no stable $TGB_A$ phase observed in non-treated cells, but only a colorful texture in between the Sm*A* focal conics and the oily streaks of $N^*$ phase. These types of textures were previously observed in the case of NPs stabilized $TGB_A$ phase [127], [156]. The colorful intermediate textures corresponding to the $TGB_A$ and $N_L^*$ phases are stable with time if the temperature is kept at a constant value. In agreement with calorimetric results, the POM textures confirm the stable $TGB_A$ phase while increasing the concentration. The optical textures of $\chi = 0.0001$ confirm the existence of $N^*$, $N_L^*$ and $TGB_A$ textures upon cooling, as can be seen in Figure 4.30. The following POM textures can be explained by the continuous twisting of SmA slabs along the $TGB_A$ helix, which appear rather metastable. These textures could not be stabilized by changing the temperature.

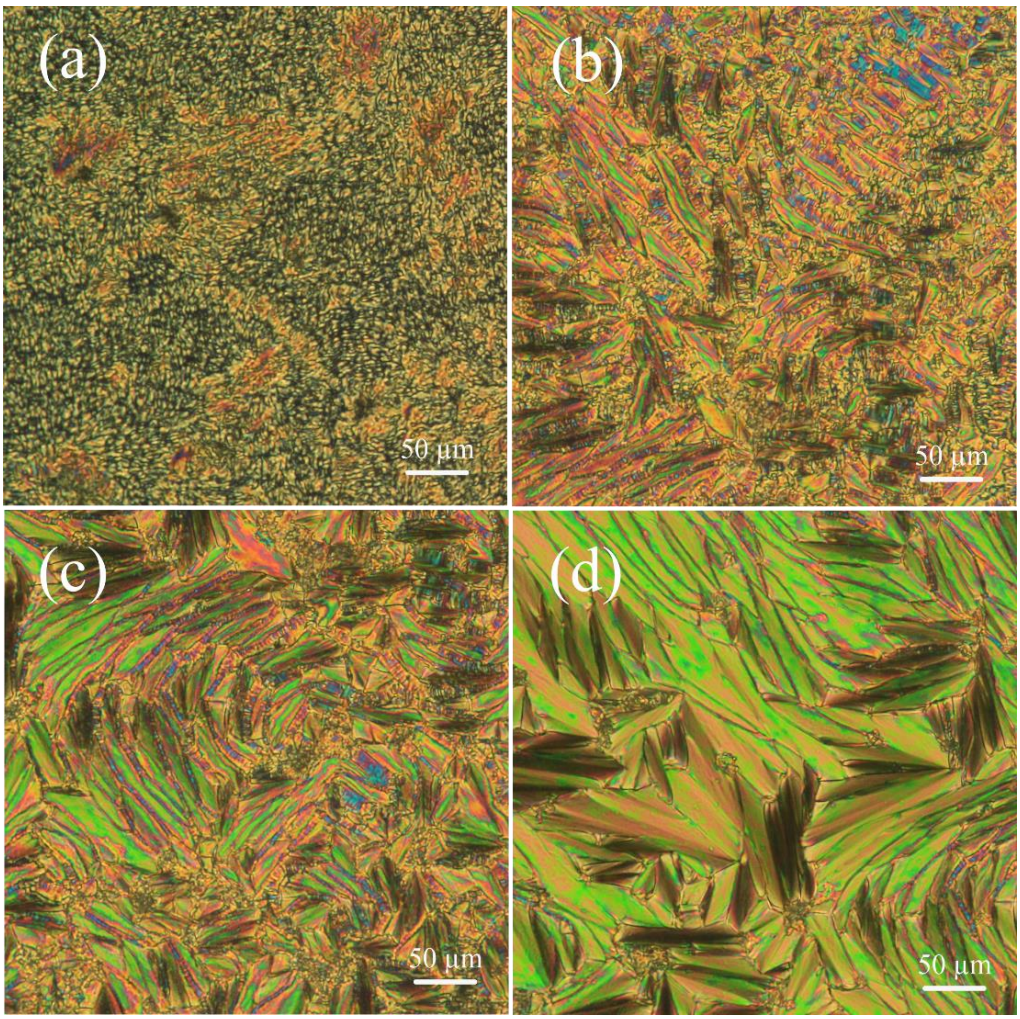


Figure 4.30: Polarizing optical microscopy textures obtained on cooling for the $\chi = 0.0001$ mixture. Presence of the (a) $N^*$, (b) $N_L^*$, (c) $TGB_A$ and (d) SmA phase.

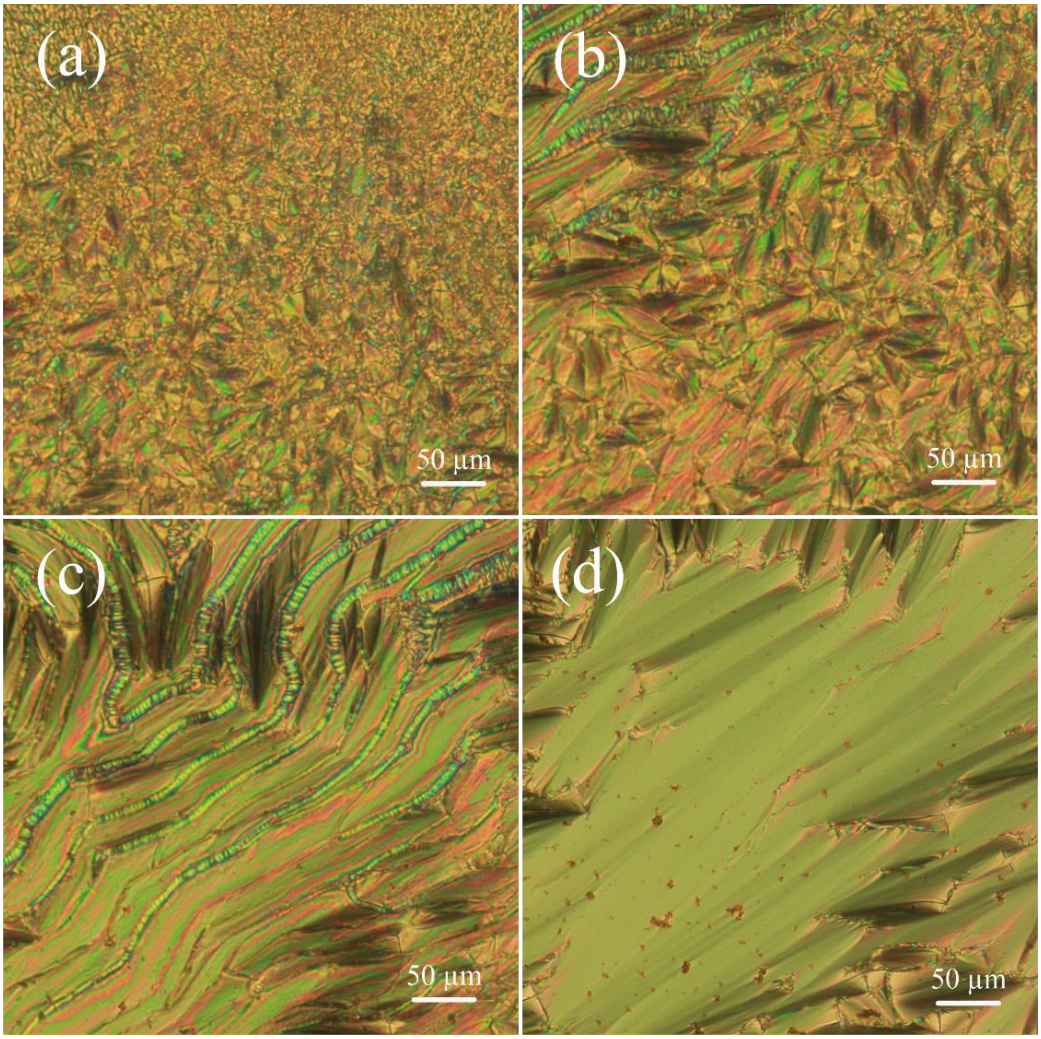


Figure 4.31: Polarizing optical microscopy textures obtained on cooling for the $\chi = 0.001$ mixture. Presence of (a) $N^*$, (b) $N_L^*$, (c) $TGB_A$ and (d) SmA phase.

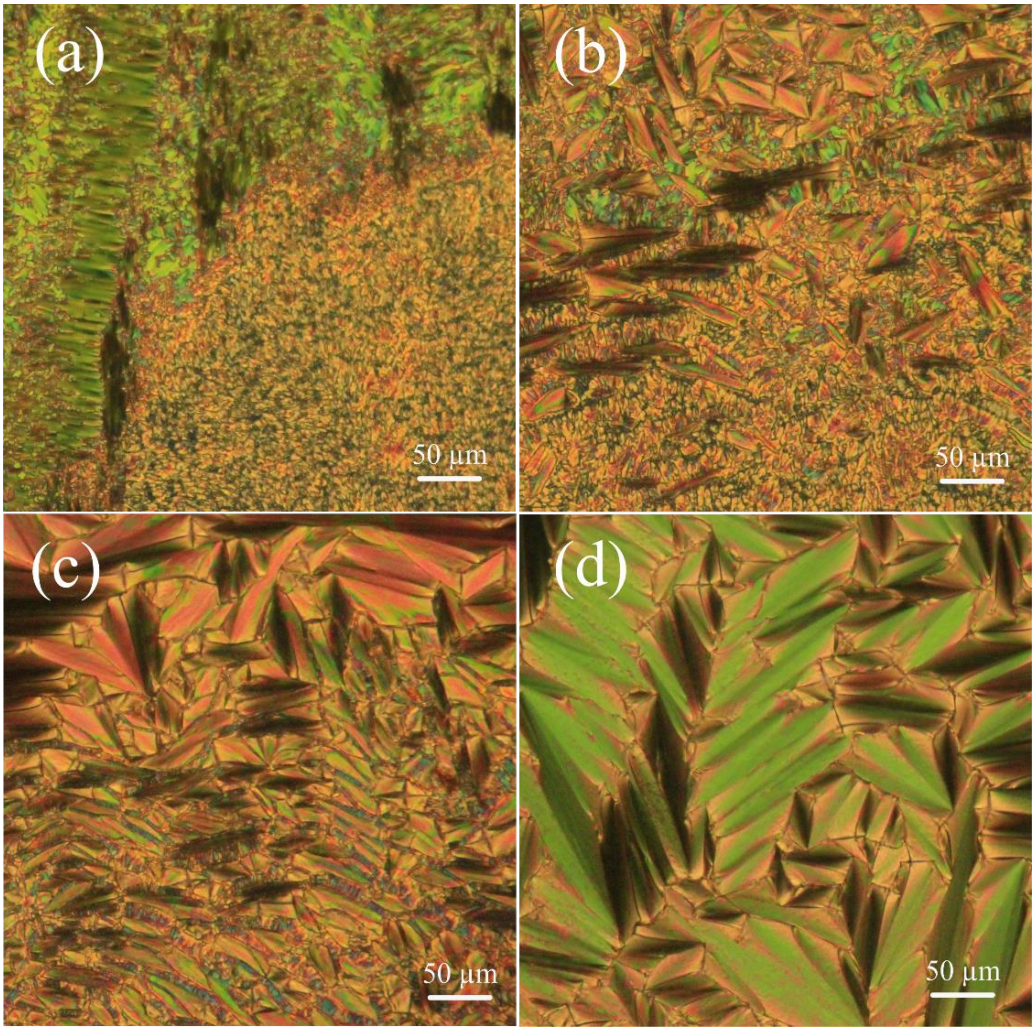


Figure 4.32: Polarizing optical microscopy textures obtained on cooling for the $\chi = 0.01$ mixture. Presence of the (a) $N^*$, (b) $N_L^*$, (c) $TGB_A$ and (d) SmA phase.

#### 4.4.2.4 Phase diagram

Based on both calorimetric and optical microscopy results, the phase diagram ($\chi - T$) of the CE8 and magnetic NPs mixtures on cooling is presented in Figure 4.26 and Figure 4.33. The phase sequences are a derived collection of temperature points from optical textures and peak points from $C_p(T)$ data by ac calorimetry have been examined upon both cooling (only optical textures) and heating cycles. In the plot, the colored lines indicate the overall temperature range of the $TGB_A$ and $N_L^*$ phases. In the case of lowering the concentration of NPs, the distinguished of both $TGB_A$ and $N_L^*$ phases are not straightforward. One could clearly notice the significant rise of the stability range of the $TGB_A$ phase; otherwise, it could be metastable in the case of pure CE8 [127], [159]. As mentioned by *Trček et al.* [159], more than twice was observed in the case of CE8+CdSSe $\chi = 0.05$ mixture temperature range 3.4 K. Later, and the same result was obtained for 2.5 times smaller concentration of CE8+Au NPs $\chi = 0.02$ mixture. In our case, we obtained similar results even smaller concentrations of NPs in CE8+Mg NPs $\chi = 0.001$ & $0.01$ mixtures.

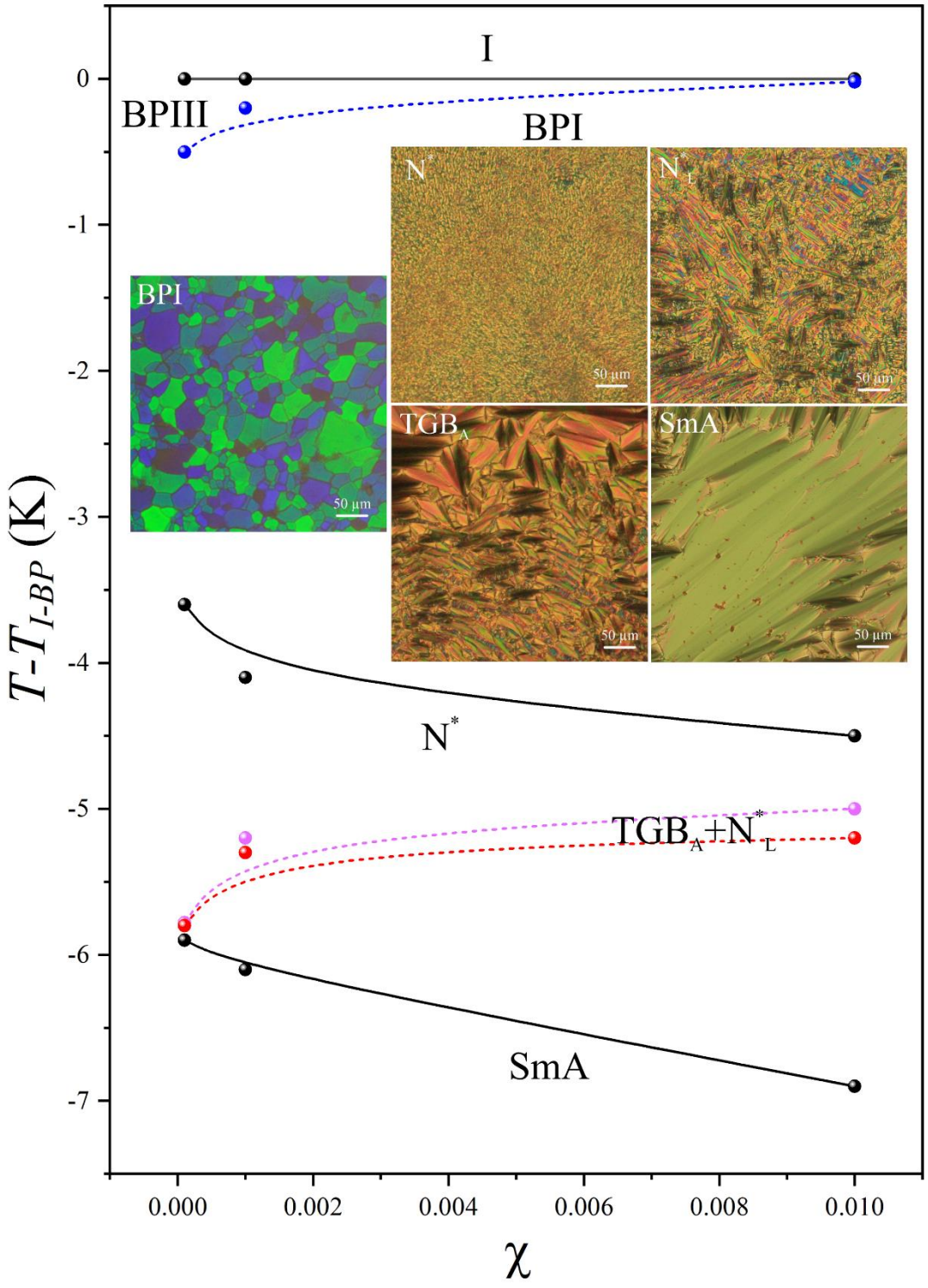


Figure 4.33: The phase diagram temperature vs. concentration ($\chi - T$) obtained for CE8 and magnetic NPs, upon cooling by POM (data points were collected from the textures appearing temperature). The solid circles represent the phase transition temperature obtained by POM and the solid lines that connect them serve as a guide to the eye.

#### 4.4.2.5 Discussion of the $TGB_A$ stabilization by magnetic NPs

The results obtained by ac calorimetry and optical microscopy demonstrate that the dispersion of magnetic NPs can moderately stabilize the short-range $TGB_A$ order between $N^*$–SmA phases of CE8. It is clearly seen that the presence of magnetic NPs gradually smears the $N^*$–SmA transition and the visible shoulders are created while increasing the $\chi$ at low-temperature wing, which represents $TGB_A$ existence. For additional confirmation of the $TGB_A$ presence, optical textures were taken with given three mixtures at specific temperature ranges. The higher concentrated mixtures $\chi = 0.01$ and $\chi = 0.001$ confirm the existence of an intermediate texture between the SmA and the oily streaks characteristic of the $N^*$ phase [156]. Those intermediate textures were previously observed in the cases of Au nanorods [159] and Au NPs [156] stabilized $TGB_A$ phase. The following textures corresponding to the $N_L^*$ and $TGB_A$ phases are stable if the temperature is kept at a constant value. In agreement with calorimetric measurements, the POM textures confirm the stable $TGB_A$ phase. Figure 4.31 and Figure 4.32 show the textures of the $N^*$, $N_L^*$, $TGB_A$ and SmA phases.

The magnetic NPs have a similar diameter to Au nanorods [159] and Au NPs [156] that have also successfully stabilized the $TGB_A$ phase. The heat capacity results are very similar to those Au nanorods, i.e., anisotropic NPs. We conclude that the stabilization of both BP and TGBA, as explained in the previous section: BP demonstrates that magnetic NPs form anisotropic clusters in defect cores, similar to Au nanorods. This indicates the possible formation of anisotropic cluster formation of magnetic NPs in defect cores mimicking the Au nanorods.

It is interesting to note that the sequence of SmA–$TGB_A$–$N_L^*$–$N^*$ heat capacity anomalies is similar to the sequence of $N^*$–BPI–PBIII–I heat capacity anomalies [159]. Especially, it is interesting to note that both BPIII-BPI and $N_L^*$–$N^*$ phase transitions can exhibit very similar broad supercritical heat capacity anomalies in BP samples with sufficiently high chirality [98], [173], [181]. Both BPIII and $N_L^*$ phases having short-range order usually react in the same way upon the addition of the magnetic NPs. However, the only difference between the TGB and BPs sequences is that there is a direct BPI-I transition, while there is no direct $TGB_A$–$N^*$ transition as all published specific heat data always show the intermediate $N_L^*$ phase [159].

# Chapter 5

# Conclusions

Of interest were conditions enabling the stability of line defects in nematic liquid crystals and the trapping of NPs into LC disclinations (line defects in orientational order) and LC dislocations (line defects in translational order). Our study consisted of sample preparation, experimental measurements by using polarizing optical microscopy (POM) and high-resolution calorimetry (ACC), theoretical analysis, and numerical simulations.

In the 1st part of the thesis, we theoretically and numerically analyzed the conditions enabling stability of disclinations in NLCs. For this purpose, we focused on nematic structures exhibiting multiple-twisted nematic distortions in cylindrical geometry. The latter enabled us to analyze several structural details of our interest analytically. Note, that the double-twist configurations for which we determined stability conditions in cylindrical geometry do not exhibit line defects. However, in 3D geometry, such structures necessary lead to the lattice of a disclination. Therefore, our study gives insight into which material conditions and structures could be realized in bulk 3D cartesian geometry. We analyzed in detail the stability of two qualitatively different classes of multiple-twisted structures. Of particular interest was the impact of the saddle-splay elastic constant $K_{24}$ which promotes fluctuations in nematic order that stabilize multiple-twisted nematic configurations. In analytic analysis, we carried out a Landau-type expansion in terms of dimensionless periodicities $Q_i$ characterizing the twisted configurations. In a chiral structure, we could easily identify the (meta) stability range of such structures because the leading term in Landau expansion is quadratic in $Q_i$. Consequently, structures of interest could be condensated if the quadratic term coefficient is negative. For the chiral case, we analyzed (meta) the stability of structures numerically. Furthermore, our stability analysis suggested a convenient method to determine the value of $K_{24}$. This constant has been so far relatively scarcely measured. Namely, it has been believed that its impact on the stability of the bulk nematic structure is negligible because mathematically its contribution could be converted from bulk to 2D surface confining the nematic order. However, later it was shown [15], [74] that additional surfaces are formed in the presence of topological defects and the presence of $K_{24}$ energy contribution could stabilize such structures. In our study, we showed that $K_{24}$ has a strong impact on the critical condition where twist reversal is realized. The latter could be relatively easily observed experimentally using optical polarizing microscopy. Furthermore, one could trigger the twist reversal terms formation by dropping LC with a chiral dopant.

In the 2nd part of our study, we analyzed the stability regime of lattices of line defects in BPs and $TGB_A$ configuration. These structures could be stable in chiral nematic (BPs) and chiral SmA phases. Of our interest was the stabilization of tee structures by using appropriate NPs with the so-called Defect-Core Replacement (DCR) mechanism. We first carried out a simple numerical analysis to demonstrate the importance of the surface treatment of NPs on coupling with LC order. We showed that NPs are attracted to cores

of topological defect structures if the resulting surface conditions at the NP-LC interface match relatively well with the local LC structures. These simulations indicate that appropriate surface treatment of NPs could enable their controlled targeting to desired regions within the LC body.

In the last part of the thesis, we focus on the stability enhancement of BPs and $TGB_A$ configurations by trapping different NPs. Experimental analysis of existing results reveals that the geometry of NPs has a strong impact on stabilizing specific defect lattices. Namely, spherical particles are, in general, efficiently stabilizing BPIII configurations. Furthermore, platelets are more efficient in stabilizing BPI and $TGB_A$ structures. In these studies, NPs were not the source of electro-magnetic (EM) fields. Our study carried pioneer studies on the impact of spherical ferromagnetic NPs on the structural stability of BPs and $TGB_A$ configurations. Our results suggest that the resulting magnetic field promotes a similar stability effect as EM-neutral NPs exhibiting cylindrical symmetry. In particular, we showed that magnetic spherical NPs are an efficient stabilizer of the BPI structure. Note that in the absence of magnetic properties spherical NPs support BPIII structures.

The fundamental understanding of the behavior of LC + magnetic NPs results in some cases can be useful for several applications in micro-sized reconfigurable devices, electro-optic applications, sensitive detectors, etc. Furthermore, they are of interest from a fundamental perspective. For example, the basic unit of BPs consists of a double-twist cylinder. Its central region exhibits the nonsingular $\mathsf{m} = 1$ escaped line defect. In order to compensate for this 2D charge in a plane perpendicular to this plane, two singulars $\mathsf{m} = -1/2$ disclinations are formed in the close neighborhood. Therefore, the BPs unit consists of a stable configuration consisting of three-line defects, which are topologically equivalent to a homogeneous nematic structure. This unit represents an LC analog of hadrons which consists of three quarks, where the total electrical charge equals zero. This analogy was first suggested by Skyrme [13]. In this study, such units (referred to as the Skyrmions) were stabilized by hand by including additional "artificial" terms into the model. However, the stability of BP structures in LCs, confirmed by experiments and simulations, suggests that geometrical concepts are crucial. Our preliminary analysis suggests that the basic understanding of Gaussian curvature of hypothetical planes, which are locally defined by the surface normal pointing along $\vec{n}$ could provide the stabilizing mechanism, which is the topic of our following research project.

# References


[1] I. W. Hamley, "Nanotechnology with Soft Materials," *Angew. Chemie Int. Ed.*, vol. 42, no. 15, pp. 1692–1712, Apr. 2003, doi: 10.1002/anie.200200546.

[2] H. K. Bisoyi and S. Kumar, "Liquid-crystal nanoscience: an emerging avenue of soft self-assembly," *Chem. Soc. Rev.*, vol. 40, no. 1, pp. 306–319, 2011, doi: 10.1039/B901793N.

[3] T. Hegmann, H. Qi, and V. M. Marx, "Nanoparticles in Liquid Crystals: Synthesis, Self-Assembly, Defect Formation and Potential Applications," *J. Inorg. Organomet. Polym. Mater.*, vol. 17, no. 3, pp. 483–508, Jun. 2007, doi: 10.1007/s10904-007-9140-5.

[4] A. C. Balazs, T. Emrick, and T. P. Russell, "Nanoparticle polymer composites: Where two small worlds meet," *Science (80-. ).*, vol. 314, no. 5802, pp. 1107–1110, 2006, doi: 10.1126/science.1130557.

[5] M. Kleman and O. Laverntovich, *Soft Matter Physics: An Introduction*. New York, NY: Springer New York, 2004.

[6] Y. A. Garbovskiy and A. V. Glushchenko, "Liquid Crystalline Colloids of Nanoparticles: Preparation, Properties, and Applications," *Solid State Phys. - Adv. Res. Appl.*, vol. 62, pp. 1–74, Jan. 2010, doi: 10.1016/B978-0-12-374293-3.00001-8.

[7] D. R. Nelson, "Toward a Tetravalent Chemistry of Colloids," *Nano Lett.*, vol. 2, no. 10, pp. 1125–1129, Oct. 2002, doi: 10.1021/nl0202096.

[8] P. Palffy-Muhoray, "The diverse world of liquid crystals," *Phys. Today*, vol. 60, no. 10, p. 17, 2007.

[9] N. D. Mermin, "The topological theory of defects in ordered media," *Rev. Mod. Phys.*, vol. 51, no. 3, pp. 591–648, Jul. 1979, doi: 10.1103/RevModPhys.51.591.

[10] O. D. LAVRENTOVICH, "Topological defects in dispersed words and worlds around liquid crystals, or liquid crystal drops," *Liq. Cryst.*, vol. 24, no. 1, pp. 117–126, Jan. 1998, doi: 10.1080/026782998207640.

[11] W. H. Zurek, "Cosmological experiments in superfluid helium?," *Nature*, vol. 317, no. 6037, pp. 505–508, Oct. 1985, doi: 10.1038/317505a0.

[12] A. Hobson, "There are no particles, there are only fields," *Am. J. Phys.*, vol. 81, no. 3, pp. 211–223, Mar. 2013, doi: 10.1119/1.4789885.

[13] T. H. R. Skyrme, "A unified field theory of mesons and baryons," *Nucl. Phys.*, vol. 31, no. C, pp. 556–569, Mar. 1962, doi: 10.1016/0029-5582(62)90775-7.

[14] G. Cordoyiannis *et al.*, "Different modulated structures of topological defects stabilized by adaptive targeting nanoparticles," *Soft Matter*, vol. 9, no. 15, p. 3956, Mar. 2013, doi: 10.1039/c3sm27644a.

[15] S. Meiboom, J. P. Sethna, P. W. Anderson, and W. F. Brinkman, "Theory of the Blue Phase of Cholesteric Liquid Crystals.," *Phys. Rev. Lett.*, vol. 46, no. 25, pp. 1656–1656, Jun. 1981, doi: 10.1103/PhysRevLett.46.1656.

[16] D. C. Wright and N. D. Mermin, "Crystalline liquids: the blue phases," *Rev. Mod. Phys.*, vol. 61, no. 2, pp. 385–432, Apr. 1989, doi: 10.1103/RevModPhys.61.385.

[17] S. R. Renn and T. C. Lubensky, "Abrikosov dislocation lattice in a model of the

cholesteric – to – smectic- A transition," *Phys. Rev. A*, vol. 38, no. 4, pp. 2132–2147, Aug. 1988, doi: 10.1103/PhysRevA.38.2132.

[18] J. W. Goodby, M. A. Waugh, S. M. Stein, E. Chin, R. Pindak, and J. S. Patel, "A new molecular ordering in helical liquid crystals," *J. Am. Chem. Soc.*, vol. 111, no. 21, pp. 8119–8125, Oct. 1989, doi: 10.1021/ja00203a009.

[19] R. Viswanathan, J. A. Zasadzinski, and D. K. Schwartz, "Spontaneous chiral symmetry breaking by achiral molecules in a Langmuir–Blodgett film," *Nature*, vol. 368, no. 6470, pp. 440–443, Mar. 1994, doi: 10.1038/368440a0.

[20] M. M. Green and V. Jain, "Homochirality in Life: Two Equal Runners, One Tripped," *Orig. Life Evol. Biosph.*, vol. 40, no. 1, pp. 111–118, Feb. 2010, doi: 10.1007/s11084-009-9180-7.

[21] L. Pasteur, "Memoires sur la relation qui peut exister entre la forme crystalline et al composition chimique, et sur la cause de la polarization rotatoire," *Compt. rend.*, vol. 26, pp. 535–538, 1848.

[22] A. B. Harris, R. D. Kamien, and T. C. Lubensky, "Molecular chirality and chiral parameters," *Rev. Mod. Phys.*, vol. 71, no. 5, pp. 1745–1757, Oct. 1999, doi: 10.1103/RevModPhys.71.1745.

[23] H. Li *et al.*, "Chiral fermion reversal in chiral crystals," *Nat. Commun.*, vol. 10, no. 1, pp. 1–7, Dec. 2019, doi: 10.1038/s41467-019-13435-4.

[24] S. Vignolini *et al.*, "A 3D Optical Metamaterial Made by Self-Assembly," *Adv. Mater.*, vol. 24, no. 10, pp. OP23–OP27, Mar. 2012, doi: 10.1002/adma.201103610.

[25] Y. Wang *et al.*, "Colloids with valence and specific directional bonding," *Nature*, vol. 491, no. 7422, pp. 51–55, Nov. 2012, doi: 10.1038/nature11564.

[26] Y.-J. Lu *et al.*, "Plasmonic Nanolaser Using Epitaxially Grown Silver Film," *Science (80-. ).*, vol. 337, no. 6093, pp. 450–453, Jul. 2012, doi: 10.1126/science.1223504.

[27] J. Yeom *et al.*, "Chiral templating of self-assembling nanostructures by circularly polarized light," *Nat. Mater.*, vol. 14, no. 1, pp. 66–72, Jan. 2015, doi: 10.1038/nmat4125.

[28] M. Siavashpouri, C. H. Wachauf, M. J. Zakhary, F. Praetorius, H. Dietz, and Z. Dogic, "Molecular engineering of chiral colloidal liquid crystals using DNA origami," *Nat. Mater.*, vol. 16, no. 8, pp. 849–856, Aug. 2017, doi: 10.1038/nmat4909.

[29] S. M. Douglas, H. Dietz, T. Liedl, B. Högberg, F. Graf, and W. M. Shih, "Self-assembly of DNA into nanoscale three-dimensional shapes," *Nature*, vol. 459, no. 7245, pp. 414–418, May 2009, doi: 10.1038/nature08016.

[30] B. M. Friedrich and F. Jülicher, "Steering Chiral Swimmers along Noisy Helical Paths," *Phys. Rev. Lett.*, vol. 103, no. 6, p. 068102, Aug. 2009, doi: 10.1103/PhysRevLett.103.068102.

[31] B. Liu, M. Gulino, M. Morse, J. X. Tang, T. R. Powers, and K. S. Breuer, "Helical motion of the cell body enhances Caulobacter crescentus motility," *Proc. Natl. Acad. Sci.*, vol. 111, no. 31, pp. 11252–11256, Aug. 2014, doi: 10.1073/pnas.1407636111.

[32] M. M. Green, N. C. Peterson, T. Sato, A. Teramoto, R. Cook, and S. Lifson, "A Helical Polymer with a Cooperative Response to Chiral Information," *Science (80-. ).*, vol. 268, no. 5219, pp. 1860–1866, Jun. 1995, doi: 10.1126/science.268.5219.1860.

[33] E. Hendry *et al.*, "Ultrasensitive detection and characterization of biomolecules using superchiral fields," *Nat. Nanotechnol.*, vol. 5, no. 11, pp. 783–787, Nov. 2010, doi: 10.1038/nnano.2010.209.

[34] B. Yeom *et al.*, "Chiral Plasmonic Nanostructures on Achiral Nanopillars," *Nano Lett.*, vol. 13, no. 11, pp. 5277–5283, Nov. 2013, doi: 10.1021/NL402782D.

[35] V. K. Valev, J. J. Baumberg, C. Sibilia, and T. Verbiest, "Chirality and Chiroptical

Effects in Plasmonic Nanostructures: Fundamentals, Recent Progress, and Outlook," *Adv. Mater.*, vol. 25, no. 18, pp. 2517–2534, May 2013, doi: 10.1002/adma.201205178.

[36] Y. Zhao *et al.*, "Shell-Engineered Chiroplasmonic Assemblies of Nanoparticles for Zeptomolar DNA Detection," *Nano Lett.*, vol. 14, no. 7, pp. 3908–3913, Jul. 2014, doi: 10.1021/nl501166m.

[37] S. Zhang, Y. S. Park, J. Li, X. Lu, W. Zhang, and X. Zhang, "Negative refractive index in chiral metamaterials," *Phys. Rev. Lett.*, vol. 102, no. 2, pp. 1–4, 2009, doi: 10.1103/PhysRevLett.102.023901.

[38] C. M. Soukoulis and M. Wegener, "Past achievements and future challenges in the development of three-dimensional photonic metamaterials," *Nat. Photonics*, vol. 5, no. 9, pp. 523–530, 2011, doi: 10.1038/nphoton.2011.154.

[39] J. M. Ribo, "Chiral Sign Induction by Vortices During the Formation of Mesophases in Stirred Solutions," *Science (80-. ).*, vol. 292, no. 5524, pp. 2063–2066, Jun. 2001, doi: 10.1126/science.1060835.

[40] Y. Snir, "Entropically Driven Helix Formation," *Science (80-. ).*, vol. 307, no. 5712, pp. 1067–1067, Feb. 2005, doi: 10.1126/science.1106243.

[41] L. E. Hough *et al.*, "Chiral Isotropic Liquids from Achiral Molecules," *Science (80-. ).*, vol. 325, no. 5939, pp. 452–456, Jul. 2009, doi: 10.1126/science.1170028.

[42] Y. Hatwalne and M. Muthukumar, "Chiral Symmetry Breaking in Crystals of Achiral Polymers," *Phys. Rev. Lett.*, vol. 105, no. 10, p. 107801, Aug. 2010, doi: 10.1103/PhysRevLett.105.107801.

[43] L. Tortora and O. D. Lavrentovich, "Chiral symmetry breaking by spatial confinement in tactoidal droplets of lyotropic chromonic liquid crystals," *Proc. Natl. Acad. Sci.*, vol. 108, no. 13, pp. 5163–5168, Mar. 2011, doi: 10.1073/pnas.1100087108.

[44] T.-C. Lin *et al.*, "Nematic molecular core flexibility and chiral induction," *Phys. Rev. E*, vol. 88, no. 4, p. 042501, Oct. 2013, doi: 10.1103/PhysRevE.88.042501.

[45] L. Wu and H. Sun, "Manipulation of cholesteric liquid crystal phase behavior and molecular assembly by molecular chirality," *Phys. Rev. E*, vol. 100, no. 2, p. 022703, Aug. 2019, doi: 10.1103/PhysRevE.100.022703.

[46] Y. Kim *et al.*, "Reconfigurable chiroptical nanocomposites with chirality transfer from the macro- to the nanoscale," *Nat. Mater.*, vol. 15, no. 4, pp. 461–468, Apr. 2016, doi: 10.1038/nmat4525.

[47] K. M. Salikhov, "Kleman, M., Lavrentovich, O.D.: Soft Matter Physics. An Introduction," *Appl. Magn. Reson.*, vol. 27, no. 3–4, pp. 563–564, Sep. 2004, doi: 10.1007/BF03166751.

[48] P. Palffy-Muhoray, "The diverse world of liquid crystals," *Phys. Today*, vol. 60, no. 9, pp. 54–60, Sep. 2007, doi: 10.1063/1.2784685.

[49] H. Zou *et al.*, "Quantifying the triboelectric series," *Nat. Commun.*, vol. 10, no. 1, p. 1427, Dec. 2019, doi: 10.1038/s41467-019-09461-x.

[50] Z. D. and and S. Fraden, "Cholesteric Phase in Virus Suspensions," *Langmuir*, vol. 16, no. 20, pp. 7820–7824, Oct. 2000, doi: 10.1021/LA000446T.

[51] L. E. Hough *et al.*, "Helical Nanofilament Phases," *Science (80-. ).*, vol. 325, no. 5939, pp. 456–460, Jul. 2009, doi: 10.1126/science.1170027.

[52] D. Andrienko, "Introduction to liquid crystals," *J. Mol. Liq.*, vol. 267, pp. 520–541, Oct. 2018, doi: 10.1016/j.molliq.2018.01.175.

[53] P. G. De Gennes and J. Prost, *The physics of liquid crystals Oxford Univ.* Oxford University Press, 1995.

[54] P. S. Pershan, "Lyotropic liquid crystals," *Phys. Today*, vol. 35, no. 5, pp. 34–39,

May 1982, doi: 10.1063/1.2915092.
[55] E. T. Samulski, "Polymeric liquid crystals," *Phys. Today*, vol. 35, no. 5, pp. 40–46, May 1982, doi: 10.1063/1.2915093.
[56] A. Gudimalla, B. Rožič, and S. Kralj, "Behavior of nanoparticles within liquid crystal phases," in *Elsevier*, 1st ed., S. Thomas, N. Kalarikkal, and A. R. Abraham, Eds. 2021, pp. 65–96.
[57] A. Gudimalla *et al.*, "Nanoparticle-Stabilized Lattices of Topological Defects in Liquid Crystals," *Int. J. Thermophys.*, vol. 41, no. 4, p. 51, Apr. 2020, doi: 10.1007/s10765-020-02631-w.
[58] M. Kleman, "Defects in liquid crystals," *Reports Prog. Phys.*, vol. 52, no. 5, p. 555, May 1989, doi: 10.1088/0034-4885/52/5/002.
[59] M. V Kurik and O. D. Lavrentovich, "Defects in liquid crystals: homotopy theory and experimental studies," *Sov. Phys. Uspekhi*, vol. 31, no. 3, pp. 196–224, Mar. 1988, doi: 10.1070/PU1988v031n03ABEH005710.
[60] S. Afghah, R. L. B. Selinger, and J. V. Selinger, "Visualising the crossover between 3D and 2D topological defects in nematic liquid crystals," *Liq. Cryst.*, vol. 45, no. 13–15, pp. 2022–2032, Dec. 2018, doi: 10.1080/02678292.2018.1494857.
[61] N. Schopohl and T. J. Sluckin, "Defect Core Structure in Nematic Liquid Crystals," *Phys. Rev. Lett.*, vol. 59, no. 22, pp. 2582–2584, Nov. 1987, doi: 10.1103/PhysRevLett.59.2582.
[62] S. Kralj, E. G. Virga, and S. Žumer, "Biaxial torus around nematic point defects," *Phys. Rev. E*, vol. 60, no. 2, pp. 1858–1866, Aug. 1999, doi: 10.1103/PhysRevE.60.1858.
[63] H. Aharoni, T. Machon, and R. D. Kamien, "Composite Dislocations in Smectic Liquid Crystals," *Phys. Rev. Lett.*, vol. 118, no. 25, p. 257801, Jun. 2017, doi: 10.1103/PhysRevLett.118.257801.
[64] S. Kralj and T. J. Sluckin, "Landau-de Gennes theory of the core structure of a screw dislocation in smectic A liquid crystals," *Liq. Cryst.*, vol. 18, no. 6, pp. 887–902, Jun. 1995, doi: 10.1080/02678299508036707.
[65] F. Reinitzer, "Beiträge zur kenntniss des cholesterins," *Monatshefte für Chemie*, vol. 9, no. 1, pp. 421–441, 1888.
[66] D. Coates and G. W. Gray, "Optical studies of the amorphous liquid-cholesteric liquid crystal transition: The 'blue phase,'" *Phys. Lett. A*, vol. 45, no. 2, pp. 115–116, Sep. 1973, doi: 10.1016/0375-9601(73)90448-9.
[67] J. Yan and S.-T. Wu, "Polymer-stabilized blue phase liquid crystals: a tutorial [Invited]," *Opt. Mater. Express*, vol. 1, no. 8, p. 1527, Dec. 2011, doi: 10.1364/OME.1.001527.
[68] H. J. Coles and M. N. Pivnenko, "Liquid crystal 'blue phases' with a wide temperature range," *Nature*, vol. 436, no. 7053, pp. 997–1000, Aug. 2005, doi: 10.1038/nature03932.
[69] J. P. Sethna, "Theory of the Blue Phases of Chiral Nematic Liquid Crystals," Springer, New York, 1987, pp. 305–324.
[70] I. Dierking *et al.*, "Stabilising liquid crystalline Blue Phases," *Soft Matter*, vol. 8, no. 16, p. 4355, Mar. 2012, doi: 10.1039/c2sm07155j.
[71] E. P. Koistinen and P. H. Keyes, "Light-Scattering Study of the Structure of Blue Phase III," *Phys. Rev. Lett.*, vol. 74, no. 22, pp. 4460–4463, May 1995, doi: 10.1103/PhysRevLett.74.4460.
[72] E. Dubois-violette, B. Pansu, and P. Pieranski, "Infinite Periodic Minimal Surfaces: A Model for Blue Phases," *Mol. Cryst. Liq. Cryst. Inc. Nonlinear Opt.*, vol. 192, no. 1, pp. 221–237, Jan. 1990, doi: 10.1080/00268949008035634.

[73] J. Yan, L. Rao, M. Jiao, Y. Li, H.-C. Cheng, and S.-T. Wu, "Polymer-stabilized optically isotropic liquid crystals for next-generation display and photonics applications," *J. Mater. Chem.*, vol. 21, no. 22, p. 7870, May 2011, doi: 10.1039/c1jm10711a.

[74] S. Meiboom and M. Sammon, "Structure of the blue phase of a cholesteric liquid crystal," *Phys. Rev. Lett.*, vol. 44, no. 13, pp. 882–885, 1980, doi: 10.1103/PhysRevLett.44.882.

[75] O. Henrich, K. Stratford, M. E. Cates, and D. Marenduzzo, "Structure of Blue Phase III of Cholesteric Liquid Crystals," *Phys. Rev. Lett.*, vol. 106, no. 10, p. 107801, Mar. 2011, doi: 10.1103/PhysRevLett.106.107801.

[76] E. Kemiklioglu, J.-Y. Hwang, and L.-C. Chien, "Stabilization of cholesteric blue phases using polymerized nanoparticles," *Phys. Rev. E*, vol. 89, no. 4, p. 042502, Apr. 2014, doi: 10.1103/PhysRevE.89.042502.

[77] W. Cao, A. Muñoz, P. Palffy-Muhoray, and B. Taheri, "Lasing in a three-dimensional photonic crystal of the liquid crystal blue phase II," *Nat. Mater.*, vol. 1, no. 2, pp. 111–113, Sep. 2002, doi: 10.1038/nmat727.

[78] W. Zhang *et al.*, "Blue phase liquid crystals affected by graphene oxide modified with aminoazobenzol group," *Liq. Cryst.*, vol. 43, no. 5, pp. 573–580, Apr. 2016, doi: 10.1080/02678292.2015.1126862.

[79] J. P. F. Lagerwall and G. Scalia, "A new era for liquid crystal research: Applications of liquid crystals in soft matter nano-, bio- and microtechnology," *Curr. Appl. Phys.*, vol. 12, no. 6, pp. 1387–1412, Nov. 2012, doi: 10.1016/j.cap.2012.03.019.

[80] Y. Hisakado, H. Kikuchi, T. Nagamura, and T. Kajiyama, "Large Electro-optic Kerr Effect in Polymer-Stabilized Liquid-Crystalline Blue Phases," *Adv. Mater.*, vol. 17, no. 1, pp. 96–98, Jan. 2005, doi: 10.1002/ADMA.200400639.

[81] H. Iwamochi and A. Yoshizawa, "Electro-optical Switching in Blue Phases Induced using a Binary System of a T-shaped Nematic Liquid Crystal and a Chiral Compound," *Appl. Phys. Express*, vol. 1, no. 11, p. 111801, Oct. 2008, doi: 10.1143/APEX.1.111801.

[82] H.-Y. Liu, C.-T. Wang, C.-Y. Hsu, T.-H. Lin, and J.-H. Liu, "Optically tuneable blue phase photonic band gaps," *Appl. Phys. Lett.*, vol. 96, no. 12, p. 121103, Mar. 2010, doi: 10.1063/1.3368119.

[83] H. Choi, H. Higuchi, Y. Ogawa, and H. Kikuchi, "Polymer-stabilized supercooled blue phase," *Appl. Phys. Lett.*, vol. 101, no. 13, p. 131904, Sep. 2012, doi: 10.1063/1.4752461.

[84] L. Wang *et al.*, "Hysteresis-Free Blue Phase Liquid-Crystal-Stabilized by ZnS Nanoparticles," *Small*, vol. 8, no. 14, pp. 2189–2193, Jul. 2012, doi: 10.1002/SMLL.201200052.

[85] M. Lavrič *et al.*, "The effect of graphene on liquid-crystalline blue phases," *Appl. Phys. Lett.*, vol. 103, no. 14, p. 143116, Sep. 2013, doi: 10.1063/1.4824424.

[86] M. Lavrič, G. Cordoyiannis, S. Kralj, V. Tzitzios, G. Nounesis, and Z. Kutnjak, "Effect of anisotropic MoS 2 nanoparticles on the blue phase range of a chiral liquid crystal," *Appl. Opt.*, vol. 52, no. 22, p. E47, Aug. 2013, doi: 10.1364/AO.52.000E47.

[87] I. Gvozdovskyy, "'Blue phases' of highly chiral thermotropic liquid crystals with a wide range of near-room temperature," *Liq. Cryst.*, vol. 42, no. 10, pp. 1391–1404, Oct. 2015, doi: 10.1080/02678292.2015.1053001.

[88] M. A. Gharbi *et al.*, "Reversible Nanoparticle Cubic Lattices in Blue Phase Liquid Crystals," *ACS Nano*, vol. 10, no. 3, pp. 3410–3415, Mar. 2016, doi: 10.1021/acsnano.5b07379.

[89] S.-Y. Jo, S.-W. Jeon, B.-C. Kim, J.-H. Bae, F. Araoka, and S.-W. Choi, "Polymer

Stabilization of Liquid-Crystal Blue Phase II toward Photonic Crystals," *ACS Appl. Mater. Interfaces*, vol. 9, no. 10, pp. 8941–8947, Mar. 2017, doi: 10.1021/acsami.7b01502.

[90] F. Liu, G. Ma, and D. Zhao, "Nickel nanoparticle-stabilized room-temperature blue-phase liquid crystals," *Nanotechnology*, vol. 29, no. 28, p. 285703, Jul. 2018, doi: 10.1088/1361-6528/aabaa4.

[91] Y. Zhao *et al.*, "Blue phase liquid crystals stabilized by graphene oxide modified with aminoalkyl group," *Mol. Cryst. Liq. Cryst.*, vol. 664, no. 1, pp. 1–8, Mar. 2018, doi: 10.1080/15421406.2018.1442706.

[92] H. Kikuchi, M. Yokota, Y. Hisakado, H. Yang, and T. Kajiyama, "Polymer-stabilized liquid crystal blue phases," *Nat. Mater.*, vol. 1, no. 1, pp. 64–68, Sep. 2002, doi: 10.1038/nmat712.

[93] G. P. Alexander and J. M. Yeomans, "Stabilizing the blue phases," *Phys. Rev. E*, vol. 74, no. 6, p. 061706, Dec. 2006, doi: 10.1103/PhysRevE.74.061706.

[94] A. Yoshizawa, H. Iwamochi, S. Segawa, and M. Sato, "The role of a liquid crystal oligomer in stabilizing blue phases," *Liq. Cryst.*, vol. 34, no. 9, pp. 1039–1044, Sep. 2007, doi: 10.1080/02678290701565867.

[95] H. Yoshida *et al.*, "Nanoparticle-Stabilized Cholesteric Blue Phases," *Appl. Phys. Express*, vol. 2, no. 12, p. 121501, Nov. 2009, doi: 10.1143/APEX.2.121501.

[96] S. Taushanoff *et al.*, "Stable amorphous blue phase of bent-core nematic liquid crystals doped with a chiral material," *J. Mater. Chem.*, vol. 20, no. 28, p. 5893, Jul. 2010, doi: 10.1039/c0jm00690d.

[97] K.-M. Chen, S. Gauza, H. Xianyu, and S.-T. Wu, "Submillisecond Gray-Level Response Time of a Polymer-Stabilized Blue-Phase Liquid Crystal," *J. Disp. Technol.*, vol. 6, no. 2, pp. 49–51, Feb. 2010, doi: 10.1109/JDT.2009.2037981.

[98] G. Cordoyiannis *et al.*, "Blue phase III widening in CE6-dispersed surface-functionalised CdSe nanoparticles," *Liq. Cryst.*, vol. 37, no. 11, pp. 1419–1426, Nov. 2010, doi: 10.1080/02678292.2010.519057.

[99] B. Rožič *et al.*, "Theoretical and experimental study of the nanoparticle-driven blue phase stabilisation," *Eur. Phys. J. E*, vol. 34, no. 2, p. 17, Feb. 2011, doi: 10.1140/epje/i2011-11017-8.

[100] P. G. de Gennes, "An analogy between superconductors and smectics A," *Solid State Commun.*, vol. 88, no. 11–12, pp. 1039–1042, 1993, doi: 10.1016/0038-1098(93)90291-T.

[101] L. Navailles, H. T. Nguyen, P. Barois, C. Destrade, and N. Isaert, "Smectic A twist grain boundary phase in three new series with chiral (L) lactic acid derivatives," *Liq. Cryst.*, vol. 15, no. 4, pp. 479–495, Oct. 1993, doi: 10.1080/02678299308036468.

[102] L. Navailles, B. Pansu, L. Gorre-Talini, and H. T. Nguyen, "Structural Study of a Commensurate TGB-A Phase and of a Presumed Chiral Line Liquid Phase," *Phys. Rev. Lett.*, vol. 81, no. 19, pp. 4168–4171, Nov. 1998, doi: 10.1103/PhysRevLett.81.4168.

[103] L. Navailles, P. Barois, and H. T. Nguyen, "X-ray measurement of the twist grain boundary angle in the liquid crystal analog of the Abrikosov phase," *Phys. Rev. Lett.*, vol. 71, no. 4, pp. 545–548, Jul. 1993, doi: 10.1103/PhysRevLett.71.545.

[104] L. Navailles, P. Barois, and H. T. Nguyen, "X-ray measurement of the twist grain boundary angle in the liquid crystal analog of the Abrikosov phase," *Phys. Rev. Lett.*, vol. 71, no. 4, pp. 545–548, Jul. 1993, doi: 10.1103/PhysRevLett.71.545.

[105] S. R. Renn and T. C. Lubensky, "Existence of a Sm-C Grain Boundary Phase at the Chiral MAC Point," *Mol. Cryst. Liq. Cryst.*, vol. 209, no. 1, pp. 349–355, Dec. 1991, doi: 10.1080/00268949108036210.

[106] S. R. Renn, "Multicritical behavior of Abrikosov vortex lattices near the cholesteric smectic-Asmectic-C* point," *Phys. Rev. A*, vol. 45, no. 2, pp. 953–973, 1992, doi: 10.1103/PhysRevA.45.953.

[107] J. W. Goodby, M. A. Waugh, S. M. Stein, E. Chin, R. Pindak, and J. S. Patel, "Characterization of a new helical smectic liquid crystal," *Nature*, vol. 337, no. 6206, pp. 449–452, Feb. 1989, doi: 10.1038/337449a0.

[108] T. C. Lubensky and S. R. Renn, "Twist-grain-boundary phases near the nematic–smectic- A –smectic- C point in liquid crystals," *Phys. Rev. A*, vol. 41, no. 8, pp. 4392–4401, Apr. 1990, doi: 10.1103/PhysRevA.41.4392.

[109] R. D. Kamien and T. C. Lubensky, "Twisted line liquids," *J. Phys. I*, vol. 3, no. 11, pp. 2131–2138, Nov. 1993, doi: 10.1051/jp1:1993110.

[110] P. Hohenberg and W. Kohn, "Physical Review Physical Review," *Phys. Rev.*, vol. 136, no. 3B, pp. 864–871, 1964.

[111] K. J. Ihn, J. A. N. Zasadzinski, R. Pindak, A. J. Slaney, and J. Goodby, "Observations of the Liquid-Crystal Analog of the Abrikosov Phase," *Science (80-. ).*, vol. 258, no. 5080, pp. 275–278, Oct. 1992, doi: 10.1126/science.258.5080.275.

[112] O. D. Lavrentovich, Y. A. Nastishin, V. I. Kulishov, Y. S. Narkevich, A. S. Tolochko, and S. V. Shiyanovskii, "Helical Smectic A," *Europhys. Lett.*, vol. 13, no. 4, pp. 313–318, Oct. 1990, doi: 10.1209/0295-5075/13/4/005.

[113] P.-G. De Gennes and J. Prost, *The physics of liquid crystals*, no. 83. Oxford university press, 1993.

[114] S. Kralj and S. Žumer, "Fréedericksz transitions in supra-μm nematic droplets," *Phys. Rev. A*, vol. 45, no. 4, pp. 2461–2470, Feb. 1992, doi: 10.1103/PhysRevA.45.2461.

[115] T. C. Lubensky and S. R. Renn, "Twist-grain-boundary phases near the nematic–smectic-$A$–smectic-$C$ point in liquid crystals," *Phys. Rev. A*, vol. 41, no. 8, p. 4392, Apr. 1990, doi: 10.1103/PhysRevA.41.4392.

[116] E. Karatairi *et al.*, "Nanoparticle-induced widening of the temperature range of liquid-crystalline blue phases," *Phys. Rev. E*, vol. 81, no. 4, p. 041703, Apr. 2010, doi: 10.1103/PhysRevE.81.041703.

[117] M. Ambrožič, S. Kralj, T. J. Sluckin, S. Žumer, and D. Svenšek, "Annihilation of edge dislocations in smectic-A liquid crystals," *Phys. Rev. E*, vol. 70, no. 5, p. 051704, Nov. 2004, doi: 10.1103/PhysRevE.70.051704.

[118] C. Kyrou, S. Kralj, M. Panagopoulou, Y. Raptis, G. Nounesis, and I. Lelidis, "Impact of spherical nanoparticles on nematic order parameters," *Phys. Rev. E*, vol. 97, no. 4, p. 042701, Apr. 2018, doi: 10.1103/PhysRevE.97.042701.

[119] Z. Kutnjak, "Ferroelectric smectic-C* liquid-crystal phase: Reexamination of the electric-field influence," *Phys. Rev. E*, vol. 70, no. 6, p. 061704, Dec. 2004, doi: 10.1103/PhysRevE.70.061704.

[120] G. S. Iannacchione, C. W. Garland, J. T. Mang, and T. P. Rieker, "Calorimetric and small angle x-ray scattering study of phase transitions in octylcyanobiphenyl-aerosil dispersions," *Phys. Rev. E*, vol. 58, no. 5, pp. 5966–5981, Nov. 1998, doi: 10.1103/PhysRevE.58.5966.

[121] A. Hourri, T. K. Bose, and J. Thoen, "Effect of silica aerosil dispersions on the dielectric properties of a nematic liquid crystal," *Phys. Rev. E*, vol. 63, no. 5, p. 051702, Apr. 2001, doi: 10.1103/PhysRevE.63.051702.

[122] T. Fukuchi-Shimogori, "Neocortex Patterning by the Secreted Signaling Molecule FGF8," *Science (80-. ).*, vol. 294, no. 5544, pp. 1071–1074, Nov. 2001, doi: 10.1126/science.1064252.

[123] G. Cordoyiannis, L. K. Kurihara, L. J. Martinez-Miranda, C. Glorieux, and J.

Thoen, "Effects of magnetic nanoparticles with different surface coating on the phase transitions of octylcyanobiphenyl liquid crystal," *Phys. Rev. E*, vol. 79, no. 1, p. 011702, Jan. 2009, doi: 10.1103/PhysRevE.79.011702.

[124] D. Coursault *et al.*, "Linear Self-Assembly of Nanoparticles Within Liquid Crystal Defect Arrays," *Adv. Mater.*, vol. 24, no. 11, pp. 1461–1465, Mar. 2012, doi: 10.1002/adma.201103791.

[125] M. Lavrič *et al.*, "Blue phase stabilization by CoPt-decorated reduced-graphene oxide nanosheets dispersed in a chiral liquid crystal," *J. Appl. Phys.*, vol. 127, no. 9, p. 095101, Mar. 2020, doi: 10.1063/1.5141930.

[126] M. Trček *et al.*, "Nanoparticle-induced twist-grain boundary phase," *Phys. Rev. E*, vol. 90, no. 3, p. 032501, Sep. 2014, doi: 10.1103/PhysRevE.90.032501.

[127] M. Trček, G. Cordoyiannis, Z. Kutnjak, G. Nounesis, and I. Lelidis, "Twist-grain-boundary-A* phase stabilisation in confined geometry by the interfaces," *Liq. Cryst.*, vol. 43, no. 10, pp. 1437–1447, Aug. 2016, doi: 10.1080/02678292.2016.1175675.

[128] B. Rožič *et al.*, "Orientational Order-Magnetization Coupling in Mixtures of Magnetic Nanoparticles and the Ferroelectric Liquid Crystal," *Ferroelectrics*, vol. 410, no. 1, pp. 37–41, Nov. 2010, doi: 10.1080/00150193.2010.492037.

[129] M. D. Lynch and D. L. Patrick, "Organizing Carbon Nanotubes with Liquid Crystals," *Nano Lett.*, vol. 2, no. 11, pp. 1197–1201, Nov. 2002, doi: 10.1021/nl025694j.

[130] I. Dierking, G. Scalia, and P. Morales, "Liquid crystal–carbon nanotube dispersions," *J. Appl. Phys.*, vol. 97, no. 4, p. 044309, Feb. 2005, doi: 10.1063/1.1850606.

[131] S. Gyergyek *et al.*, "Hydrothermal growth of iron oxide NPs with a uniform size distribution for magnetically induced hyperthermia: Structural, colloidal and magnetic properties," *J. Alloys Compd.*, vol. 694, pp. 261–271, Feb. 2017, doi: 10.1016/J.JALLCOM.2016.09.238.

[132] C. Bahr and H. Kitzerow, *Chirality in Liquid Crystals*. New York: Springer-Verlag, 2001.

[133] C. W. GARLAND, "Calorimetric studies," in *Liquid Crystals: Experimental Study of Physical Properties and Phase Transitions*, Cambridge University Press, 2001, p. 240.

[134] M. Anisimov, *Critical phenomena in liquids and liquid crystals*. CRC Press, 1991.

[135] J. Thoen, G. Cordoyiannis, and C. Glorieux, "Investigations of phase transitions in liquid crystals by means of adiabatic scanning calorimetry," *Liq. Cryst.*, vol. 36, no. 6–7, pp. 669–684, Aug. 2009, doi: 10.1080/02678290902755564.

[136] K. Ema, T. Uematsu, A. Sugata, and H. Yao, "Complex Calorimeter with AC- and Relaxation-Mode Operation," *Jpn. J. Appl. Phys.*, vol. 32, no. Part 1, No. 4, pp. 1846–1850, Apr. 1993, doi: 10.1143/JJAP.32.1846.

[137] C. W. Garland and G. Nounesis, "Critical behavior at nematic–smectic- A phase transitions," *Phys. Rev. E*, vol. 49, no. 4, pp. 2964–2971, Apr. 1994, doi: 10.1103/PhysRevE.49.2964.

[138] Z. Kutnjak, J. Petzelt, and R. Blinc, "The giant electromechanical response in ferroelectric relaxors as a critical phenomenon," *Nature*, vol. 441, no. 7096, pp. 956–959, Jun. 2006, doi: 10.1038/nature04854.

[139] K. Ema, H. Yao, I. Kawamura, T. Chan, and C. W. Garland, "High-resolution calorimetric study of the antiferroelectric liquid crystals methylheptyloxycarbonylphenyl octyloxybiphenyl carboxylate and its octylcarbonylbiphenyl analog," *Phys. Rev. E*, vol. 47, no. 2, p. 1203, Feb. 1993, doi: 10.1103/PhysRevE.47.1203.

[140] H. Yao, K. Ema, and C. W. Garland, "Nonadiabatic scanning calorimeter," *Rev. Sci. Instrum.*, vol. 69, no. 1, pp. 172–178, Jan. 1998, doi: 10.1063/1.1148492.

[141] O. D. L. Maurice Kleman, *Soft Matter Physics: An Introduction*. Springer, 2007.

[142] J. Jeong, L. Kang, Z. S. Davidson, P. J. Collings, T. C. Lubensky, and A. G. Yodh, "Chiral structures from achiral liquid crystals in cylindrical capillaries," *Proc. Natl. Acad. Sci.*, vol. 112, no. 15, pp. E1837–E1844, Apr. 2015, doi: 10.1073/pnas.1423220112.

[143] G. P. Crawford, J. A. Mitcheltree, E. P. Boyko, W. Fritz, S. Zumer, and J. W. Doane, "K 33 / K 11 determination in nematic liquid crystals: An optical birefringence technique," *Appl. Phys. Lett.*, vol. 60, no. 26, pp. 3226–3228, Jun. 1992, doi: 10.1063/1.106701.

[144] M. Ambrožič, A. Gudimalla, C. Rosenblatt, and S. Kralj, "Multiple Twisted Chiral Nematic Structures in Cylindrical Confinement," *Crystals*, vol. 10, no. 7, p. 576, Jul. 2020, doi: 10.3390/cryst10070576.

[145] R. D. Polak, G. P. Crawford, B. C. Kostival, J. W. Doane, and S. Umer, "Optical determination of the saddle-splay elastic constant K24 in nematic liquid crystals," *Phys. Rev. E*, vol. 49, no. 2, 1994, doi: 10.1103/PHYSREVE.49.R978.

[146] M. Ambrožič and S. Žumer, "Chiral nematic liquid crystals in cylindrical cavities," *Phys. Rev. E*, vol. 54, no. 5, pp. 5187–5197, Nov. 1996, doi: 10.1103/PhysRevE.54.5187.

[147] M. Ambrožič and S. Žumer, "Axially twisted chiral nematic structures in cylindrical cavities," *Phys. Rev. E*, vol. 59, no. 4, pp. 4153–4160, Apr. 1999, doi: 10.1103/PhysRevE.59.4153.

[148] H. De Sterck and K. Miller, "An Adaptive Algebraic Multigrid Algorithm for Low-Rank Canonical Tensor Decomposition," *SIAM J. Sci. Comput.*, vol. 35, no. 1, pp. B1–B24, Jan. 2013, doi: 10.1137/110855934.

[149] S.-P. Do *et al.*, "From Chains to Monolayers: Nanoparticle Assembly Driven by Smectic Topological Defects," *Nano Lett.*, vol. 20, no. 3, pp. 1598–1606, Mar. 2020, doi: 10.1021/acs.nanolett.9b04347.

[150] S.-P. Do *et al.*, "Interactions Between Topological Defects and Nanoparticles," *Front. Phys.*, vol. 7, p. 234, Feb. 2020, doi: 10.3389/fphy.2019.00234.

[151] S. Kralj, "Nanoparticle Controlled Soft Complex Structures with Topological Defects." Oct. 01, 2013, Accessed: Aug. 25, 2021. [Online]. Available: https://apps.dtic.mil/sti/citations/ADA597739.

[152] M. Škarabot, A. V. Ryzhkova, and I. Muševič, "Interactions of single nanoparticles in nematic liquid crystal," *J. Mol. Liq.*, vol. 267, pp. 384–389, Oct. 2018, doi: 10.1016/j.molliq.2018.01.068.

[153] A. V. Dubtsov, S. V. Pasechnik, D. V. Shmeliova, S. Kralj, and R. Repnik, "Controlled Nanoparticle Targeting and Nanoparticle-Driven Nematic Structural Transition," *Adv. Condens. Matter Phys.*, vol. 2015, pp. 1–9, 2015, doi: 10.1155/2015/803480.

[154] P. Kaiser, W. Wiese, and S. Hess, "Stability and Instability of an Uniaxial Alignment Against Biaxial Distortions in the Isotropic and Nematic Phases of Liquid Crystals," *J. Non-Equilibrium Thermodyn.*, vol. 17, no. 2, pp. 153–170, Jan. 1992, doi: 10.1515/jnet.1992.17.2.153.

[155] R. Rosso, E. G. Virga, and S. Kralj, "Elastic actions exchanged by eccentric cylinders in liquid crystals," *Phys. Rev. E*, vol. 74, no. 6, p. 061703, Dec. 2006, doi: 10.1103/PhysRevE.74.061703.

[156] M. Trček *et al.*, "Twist-grain boundary phase induced by Au nanoparticles in a chiral liquid crystal host," *Liq. Cryst.*, vol. 44, no. 10, pp. 1575–1581, Aug. 2017,

doi: 10.1080/02678292.2017.1306887.

[157] M. Lavrič *et al.*, "Blue Phase Range Widening Induced by Laponite Nanoplatelets in the Chiral Liquid Crystal CE8," *Mol. Cryst. Liq. Cryst.*, vol. 615, no. 1, pp. 14–18, Jul. 2015, doi: 10.1080/15421406.2015.1066554.

[158] M. Lavrič, "Stabilization of cholesteric blue phases by nanoparticles and nematic caloric effects induced by external fields," 2018, Accessed: Aug. 16, 2021. [Online]. Available: https://repozitorij.uni-lj.si/IzpisGradiva.php?id=106028.

[159] M. Trček, "Nanoparticle-induced twist grain boundary phases and electrocaloric effect in liquid crystals : PhD thesis," 2017, Accessed: Aug. 02, 2021. [Online]. Available: https://repozitorij.uni-lj.si/IzpisGradiva.php?id=97429.

[160] G. Cordoyiannis *et al.*, "Quantum Dot-Driven Stabilization of Liquid-Crystalline Blue Phases," *Front. Phys.*, vol. 8, p. 315, Aug. 2020, doi: 10.3389/fphy.2020.00315.

[161] P. J. Collings and J. R. McColl, "Nuclear magnetic resonance spectroscopy in cholesteric liquid crystals .II. The blue phase," *J. Chem. Phys.*, vol. 69, no. 7, pp. 3371–3373, Oct. 1978, doi: 10.1063/1.436963.

[162] C. A. F. Johnson, S. D. Kelly, and J. E. Parker, "Triplet states in the dissociative excitation of water by electron impact," *Chem. Phys. Lett.*, vol. 116, no. 1, pp. 30–34, Apr. 1985, doi: 10.1016/0009-2614(85)80119-6.

[163] P. H. Keyes, "The Cholesteric Blue Phases," *MRS Bull.*, vol. 16, no. 1, pp. 32–37, Jan. 1991, doi: 10.1557/S0883769400057882.

[164] A. Leforstier and F. Livolant, "DNA liquid crystalline blue phases. Electron microscopy evidence and biological implications," *Liq. Cryst.*, vol. 17, no. 5, pp. 651–658, Nov. 1994, doi: 10.1080/02678299408037336.

[165] J. Charvolin and J.-F. Sadoc, "A geometrical template for toroidal aggregates of chiral macromolecules," *Eur. Phys. J. E*, vol. 25, no. 3, pp. 335–341, Mar. 2008, doi: 10.1140/epje/i2008-10313-8.

[166] R. Barbet-Massin, "P. E. Cladis and P. Pieranski," *Phys. Rev. A*, vol. 30, p. 1161, 1984.

[167] P. Keyes, "High-chirality blue-phase lattices are unstable: A theory for the formation of blue phase III," *Phys. Rev. Lett.*, vol. 65, no. 4, pp. 436–439, Jul. 1990, doi: 10.1103/PhysRevLett.65.436.

[168] P. J. Collings, "Comment on '"Chiral-racemic phase diagram of a blue-phase liquid crystal,"'" *Phys. Rev. A*, vol. 33, no. 3, p. 2153, Mar. 1986, doi: 10.1103/PhysRevA.33.2153.

[169] J. Thoen, "Adiabatic scanning calorimetric results for the blue phases of cholesteryl nonanoate," *Phys. Rev. A*, vol. 37, no. 5, pp. 1754–1759, Mar. 1988, doi: 10.1103/PhysRevA.37.1754.

[170] G. Voets and W. van Dael, "Investigation of the chirality dependence of thermal properties in chiral-racemic mixtures of the cholesteric ester CE6," *Liq. Cryst.*, vol. 14, no. 3, pp. 617–627, Jan. 1993, doi: 10.1080/02678299308027740.

[171] Z. Kutnjak, C. W. Garland, C. G. Schatz, P. J. Collings, C. J. Booth, and J. W. Goodby, "Critical point for the blue-phase-III–isotropic phase transition in chiral liquid crystals," *Phys. Rev. E*, vol. 53, no. 5, pp. 4955–4963, May 1996, doi: 10.1103/PhysRevE.53.4955.

[172] M. A. Anisimov, V. A. Agayan, and P. J. Collings, "Nature of the Blue-Phase-III–isotropic critical point: An analogy with the liquid-gas transition," *Phys. Rev. E*, vol. 57, no. 1, pp. 582–595, Jan. 1998, doi: 10.1103/PhysRevE.57.582.

[173] Z. Kutnjak, C. W. Garland, J. L. Passmore, and P. J. Collings, "Supercritical Conversion of the Third Blue Phase to the Isotropic Phase in a Highly Chiral Liquid Crystal," *Phys. Rev. Lett.*, vol. 74, no. 24, pp. 4859–4862, Jun. 1995, doi:

10.1103/PhysRevLett.74.4859.

[174] H.-S. Kitzerow, H. Schmid, A. Ranft, G. Heppke, R. A. M. Hikmet, and J. Lub, "Observation of blue phases in chiral networks," *Liq. Cryst.*, vol. 14, no. 3, pp. 911–916, Jan. 1993, doi: 10.1080/02678299308027768.

[175] C. Bohley and T. Scharf, "Blue phases as photonic crystals," in *Physics, Theory, and Applications of Periodic Structures in Optics II*, Dec. 2003, vol. 5184, p. 202, doi: 10.1117/12.503554.

[176] Y. Hisakado, H. Kikuchi, T. Nagamura, and T. Kajiyama, "Large Electro-optic Kerr Effect in Polymer-Stabilized Liquid-Crystalline Blue Phases," *Adv. Mater.*, vol. 17, no. 1, pp. 96–98, Jan. 2005, doi: 10.1002/adma.200400639.

[177] T. Noma *et al.*, "Effects of Polymer Network Surfaces on Expansion of Cholesteric Blue Phases Temperature," *e-Journal Surf. Sci. Nanotechnol.*, vol. 6, pp. 17–20, Jan. 2008, doi: 10.1380/ejssnt.2008.17.

[178] T. Iwata *et al.*, "Control of Cross-Linking Polymerization Kinetics and Polymer Aggregated Structure in Polymer-Stabilized Liquid Crystalline Blue Phases," *Macromolecules*, vol. 42, no. 6, pp. 2002–2008, Mar. 2009, doi: 10.1021/ma802464w.

[179] J. Fernsler *et al.*, "From The Cover: Giant-block twist grain boundary smectic phases," *Proc. Natl. Acad. Sci.*, vol. 102, no. 40, pp. 14191–14196, Oct. 2005, doi: 10.1073/pnas.0500664102.

[180] P. Wilson, S. Cowling, and D. Lacey, "Synthesis and evaluation of novel selenophene-and thiophene-containing liquid crystal materials exhibiting TGB C* phases," in *8th International Conference on Ferroelectric Liquid Crystals*, 2001, pp. 5–10.

[181] Z. Kutnjak, C. W. Garland, C. G. Schatz, P. J. Collings, C. J. Booth, and J. W. Goodby, "Critical point for the blue-phase-III–isotropic phase transition in chiral liquid crystals," *Phys. Rev. E*, vol. 53, no. 5, pp. 4955–4963, May 1996, doi: 10.1103/PhysRevE.53.4955.

# Bibliography

## Publications Related to the Thesis

### Journal Articles

A. Gudimalla, S. Thomas, and A. Zidanšek, "Phase behaviour of n-CB liquid crystals confined to controlled pore glasses," *Journal of Molecular Structure*, vol. 1235, p. 130217, 2021, doi: 10.1016/j.molstruc.2021.130217.

A. Gudimalla *et al.*, "Nanoparticle-Stabilized Lattices of Topological Defects in Liquid Crystals," *Int J Thermophys*, vol. 41, no. 4, 2020, doi: 10.1007/s10765-020-02631-w.

M. Ambrožič, A. Gudimalla, C. Rosenblatt, and S. Kralj, "Multiple Twisted Chiral Nematic Structures in Cylindrical Confinement," *Crystals*, vol. 10, no. 7, p. 576, 2020, doi: 10.3390/cryst10070576.

A. Gudimalla *et al.*, "Influence of magnetic nanoparticless on phase transition of CE8 liquid crystals" (tentative title)(Under preparation)

### Book Chapter

A. Gudimalla, B. Rožič, and S. Kralj, "Behavior of nanoparticles within liquid crystal phases," in *Fundamentals and Properties of Multifunctional Nanomaterials*, S. Thomas, N. Kalarikkal, and A. R. Abraham, Eds. Elsevier, 2021, pp. 65–96, doi: 10.1016/B978-0-12-822352-9.00014-6.

## Other Publications

A. Gudimalla, J. Jose, R. J. Varghese, and S. Thomas, "Green Synthesis of Silver Nanoparticles Using Nymphae odorata Extract Incorporated Films and Antimicrobial Activity," *J Polym Environ*, vol. 29, no. 5, pp. 1412–1423, 2021, doi: 10.1007/s10924-020-01959-6.

A. Gudimalla J. Jose, R. J. Varghese, G. Gurram and S. Thomas, "Synthesis of Silver Nanoparticles by Plant Extract, Incorporated into Alginate Films and their Characterizations," *Chem. Pap.*, pp. 1-13, 2021, doi: 10.1007/s11696-021-01923-1.

V. R Jose, L. Vidya, T. M Joseph, A. Gudimalla, G. H. Bhuvaneswari, and S. Thomas, "Potential Applications of XLPE Nanocomposites in the Field of Cable Insulation," in *Crosslinkable Polyethylene Based Blends and Nanocomposites* , J. Thomas and S. Thomas, Eds. Springer Nature, 2021, p. 197.

A. Gudimalla *et al.*, "Electrospinning as a Novel Delivery Vehical for Bioactive Compounds in Food," in *Innovative food science and emerging technologies* , S. Thomas, R. Rajendran, A. George, and N. Kalarikal, Eds. Apple Academic Press, 2018.

A. Gudimalla, R. K. Mishra, and P. Arora, "Novel Approaches to Nanomedicine and Nanotechnology," in *Recent Trends in Nanomedicine and Tissue Engineering* , J. Thomas, S. Thomas, Ji. Jose, and N. Kalarikkal, Eds. River Publishers, 2017, p. 19.

G. Gurram, R. K. N. R. Manepalli, and A. Gudimalla, "Size-exclusion chromatography in Nanoscience and Nanotechnology," in *Thermal and Rheological Measurement Techniques for Nanomaterials Characterization* , S. Thomas, R. Thomas, A. K. Zachariah, and R. K. Mishra, Eds. 2017, pp. 51–65.

G. Gurram, R. K. N. R. Manepalli, and A. Gudimalla, "Confocal Raman Spectroscopy," in *Spectroscopic Methods for Nanomaterials Characterization* , S. Thomas, R. Thomas, A. K. Zachariah, and R. K. Mishra, Eds. 2017, pp. 141–161.

G. Gurram, R. K. N. R. Manepalli, and A. Gudimalla, "Contact Angle Measurements Techniques in Nanosciences and Nanotechnology," in *Thermal and Rheological Measurement Techniques for Nanomaterials Characterization*, S. Thomas, R. Thomas, A. K. Zachariah, and R. K. Mishra, Eds. Elsevier, 2017, pp. 173–195.

G. Gurram, M. RKNR, and A. Gudimalla, "X-ray Microanalysis and Electron Energy Loss Spectroscopy (EELS)," in *Microscopy Methods in Nanomaterials Characterization* , S. Thomas, R. Thomas, Ajesh. K. Zachariah, and Raghvendra. K. Mishra, Eds. Elsevier, 2017, pp. 293–311.

## Patents

A. Gudimalla, T. A. Sajith, S. Thomas, N. Kalarikkal, Z. Ahmad, "High-Performance EMI Shielding Coating Form Low-Cost Carbon Black with XLPE", Ref. No. 201841040343, C. B. R. No. 30477, 2018, (Filed).

# Biography

Mr. Apparao Gudimalla was born on 23.12.1993 in Surampalem, India. He completed his earlier studies Integrated M.Sc. Nanotechnology (5 years) from the Department of Nanotechnology, Acharya Nagarjuna University, Guntur, Andhra Pradesh, India. He completed his Master studies with the thesis entitled "Biosynthesis of Silver Nanoparticles Incorporated with Alginate Films for Wound Healing Applications" under the supervision of Prof. Dr. Sabu Thomas (IIUCNN, Mahatma Gandhi University, Kerala, India). After that, he continued as a Research Assistant under a project entitled "Development of Hybrid Fillers for Various Engineering Applications" supported by University Teknologi MARA, Malaysia. In late 2017, he enrolled his Doctoral studies at Jožef Stefan International Postgraduate School and started working in the Condensed Matter Department (F5) at Jožef Stefan Institute Ljubljana, Slovenia.